



LIGO Laboratory / LIGO Scientific Collaboration

LIGO-T060269-01-D

ADVANCED LIGO

5/03/07

Input Optics Subsystem
Preliminary Design Document

Muzammil A. Arain, Antonio Lucianetti, Rodica Martin, Guido Mueller, Volker Quetschke, David Reitze, David Tanner, Luke Williams, and Wan Wu

Distribution of this document:
LIGO Science Collaboration

This is an internal working note
of the LIGO Project.

California Institute of Technology
LIGO Project – MS 18-34
1200 E. California Blvd.
Pasadena, CA 91125
Phone (626) 395-2129
Fax (626) 304-9834
E-mail: info@ligo.caltech.edu

Massachusetts Institute of Technology
LIGO Project – NW17-161
175 Albany St
Cambridge, MA 02139
Phone (617) 253-4824
Fax (617) 253-7014
E-mail: info@ligo.mit.edu

LIGO Hanford Observatory
P.O. Box 1970
Mail Stop S9-02
Richland WA 99352
Phone 509-372-8106
Fax 509-372-8137

LIGO Livingston Observatory
P.O. Box 940
Livingston, LA 70754
Phone 225-686-3100
Fax 225-686-7189

<http://www.ligo.caltech.edu/>

Table of Contents

1	<i>Introduction</i>	10
1.1	Purpose	10
1.2	Scope	10
1.2.1	IO Subsystems	11
1.3	Definitions	11
1.4	Acronyms	11
1.5	Applicable Documents	12
1.5.1	LIGO Documents	12
1.5.2	Non-LIGO Documents	12
2	<i>Overview of Design Status</i>	13
2.1	Summary of the design changes from the Conceptual Design	13
2.1.1	In-vacuum Layout	13
2.1.2	Modulation Method	13
2.1.3	Reduction in the IMC finesse	13
2.2	Areas that need more work	14
2.2.1	Complex (AM/PM) modulation	14
2.2.2	Faraday Isolator Performance in Vacuum	14
2.2.3	Adaptive Mode-matching	14
2.2.4	IO Baffling	14
2.3	Areas that have been de-emphasized	14
2.3.1	Active jitter suppression	14
3	<i>Interfaces with other subsystems</i>	16
3.1	PSL	16
3.1.1	Optical	16
3.1.2	Mechanical	16
3.1.3	Water	17
3.2	COC	17
3.2.1	Optical	17
3.3	ISC/CDS	17
3.3.1	Optical	17
3.3.2	Mechanical	18
3.3.3	Electrical	18
3.4	SEI	19
3.4.1	Mechanical	19
3.5	AOS	19
3.5.1	Optical	19
3.6	SUS	19

4	<i>Optical Layout</i>	20
4.1	Assumptions	20
4.2	PSL Table Layout	20
4.2.1	Optical Components	21
4.2.2	Laser Beam Injection Periscope	22
4.3	In-vacuum optical layout	22
4.3.1	Design Considerations	22
4.3.2	Stable Recycling Cavity Layouts	23
4.3.3	Marginally Stable Power Recycling Cavity	25
4.4	Baffles	27
4.4.1	MC errant beam baffles	27
4.4.2	SOS baffles	29
4.4.3	Modified LOS baffle	30
4.4.4	MC cleaning baffle	31
4.4.5	HAM 2 baffle	32
4.4.6	IO baffle	33
5	<i>Power Control Subsystem</i>	35
5.1	Requirements	35
5.2	Design	35
5.2.1	Radiation pressure and IMC displacement	36
5.3	Beam Dump	38
5.3.1	Alternative Low Backscatter Beam Dump	40
6	<i>RF Modulation</i>	42
6.1	Introduction	42
6.2	Baseline Design	42
6.3	Constraints	43
6.4	RF modulation requirements	43
6.4.1	Modulation frequencies	43
6.4.2	Modulation depths	43
6.5	Modulator design	43
6.5.1	Mechanical design	43
6.5.2	Impedance matching	44
6.5.3	Temperature stabilization	44
6.5.4	Damage testing and thermal lensing	44
6.6	Avoiding Sidebands on Sidebands	45
6.6.1	Parallel (Mach-Zehnder) modulation	45
6.6.2	Noise coupling / estimates	46
6.6.3	Experimental realization	49
6.6.4	Power scaling	52
6.6.5	Monolithic design (alternative design #1)	52

6.6.6	Complex modulation (alternative design #2)	53
7	<i>Input Mode Cleaner</i>	56
7.1	Optical Configuration and Definitions	56
7.2	Input Mode Cleaner Optical Parameters	57
7.2.1	Constraints and Assumptions	57
7.2.2	Lengths	57
7.2.3	Modulation frequencies	58
7.2.4	Straight IFO, Marginal PRC	59
7.2.5	Straight IFO, Stable PRC	59
7.2.6	Folded IFO, Marginal PRC	60
7.2.7	Folded IFO, Stable PRC	60
7.2.8	Calculated Optical Parameters	61
7.2.9	Input Mode Cleaner Locking Frequency	62
7.3	Input Mode Cleaner Expected Performance	62
7.3.2	Jitter Suppression	62
7.3.3	Higher Order Mode Rejection	63
7.3.4	Laser wavelength stabilization	64
7.3.5	Laser noise suppression	64
7.3.6	Polarization	64
7.3.7	Input Mode Cleaner Instabilities	65
7.3.8	Input Mode Cleaner Thermal effects	66
7.3.9	Input Mode Cleaner Noise Budget	68
8	<i>Faraday Isolator</i>	69
8.1	Faraday Isolator Design	69
8.2	Optical Characterization	69
8.2.1	Optical Isolation	70
8.2.2	Thermal Drift	71
8.2.3	Thermal Lens Compensation	71
8.3	Vacuum compatibility	71
8.3.1	Preliminary UHV tests	71
8.4	Excess Phase Noise	73
8.4.1	Movement of a focusing element	73
8.4.2	Movement of a prism (wedge)	74
9	<i>IFO MODE MATCHING TELESCOPE</i>	76
9.1	Overview of Mode Matching Telescope Design	76
9.1.1	Design Philosophy	76
9.1.2	Design Assumptions	77
9.2	MSPRC MMT	78
9.2.1	Optical Layout of MMT	78
9.2.2	MMT Design Parameters	78
9.2.3	Preliminary Mirror Component Specifications	79

9.2.4	Adaptive Mode Matching	80
9.2.5	MSPRC Mode Matching Operation and Performance	80
9.2.6	Preliminary Adaptive Mode Matching Specifications	84
9.3	SPRC Mode Matching Telescope	88
9.3.1	Optical Layout of Mode Matching Telescope	88
9.3.2	MMT Design Parameters	89
9.3.3	Preliminary Mirror Component Specifications	89
9.3.4	Adaptive Mode Matching	90
9.3.5	MSPRC Mode Matching Operation and Performance	90
9.3.6	Preliminary Adaptive Mode Matching Specifications	91
9.4	Angular Noise	91
10	Overall IO Performance	92
10.1	Optical throughput	92
11	Diagnostics	94
11.1.1	PSL Table	94
11.1.2	Mode Cleaner	94
11.1.3	Faraday Isolator	94
11.1.4	IFO Mode-Matching Telescope	95
12	Preparation for Delivery	96
12.1	Preparation	96
12.2	Packaging	96
12.2.1	Small Optics	96
12.2.2	Mode Cleaner Mirrors and Large MMT mirror	96
12.3	Marking	96
12.3.1	Vendor-supplied catalog items	96
12.3.2	Vendor-supplied custom items	96
12.3.3	UF manufactured mechanical and opto-mechanical components	97
12.3.4	Suspended mirrors	97
13	Assembly and Installation	98
13.1	Installation Tooling and Fixtures	98
13.1.1	PSL Table	98
13.1.2	In-HAM optics	98
13.2	Installation and Alignment Procedures	100
13.2.1	Mechanical alignment	100
13.2.2	Optical alignment	100

Appendices

Appendix A Quality Conformance Inspections Error! Bookmark not defined.

Table of Tables

Table 1 Required RF inputs to IO EOMs. _____	18
Table 2 Summary of PSL table optical component sizes _____	22
Table 3 Parameter Values for Triple Pendulum IMC Mirror. _____	37
Table 4 Performance of the Advanced LIGO FI _____	43
Table 5 Allowed range of lengths for LIGO cavities _____	58
Table 6. Straight IFO, Marginal PRC _____	59
Table 7. Straight IFO, Stable PRC _____	59
Table 8. Folded IFO, Marginal PRC _____	60
Table 9. Folded IFO, Stable PRC _____	60
Table 10 Optical parameters for the straight interferometer, marginal PRC _____	61
Table 11 Temperature effects in the IMC _____	67
Table 12 Performance of the Advanced LIGO FI _____	70
Table 13 Parameters for MSPRC _____	78
Table 14 Component Specifications _____	79
Table 15 Static Errors Sources and Mode Miss-Match _____	82
Table 16 Parameters for SPRC _____	89
Table 17 Component Specifications _____	89
Table 18 Optical throughput _____	92

Table of Figures

Figure 1.1. Block Diagram of the Input Optics _____	10
Figure 3.1 Defined IO and PSL areas on the PSL table, _____	17
Figure 4.1 Diagram of the PSL Table showing IO components _____	20
Figure 4.2 Blow up of the main area of the IO components on the PSL table showing functional blocks of IO components. _____	21
Figure 4.3 Layout drawing of HAM2,3 for the stable power recycling cavity configuration. ____	23
Figure 4.4 Another view of the SPRC layout looking from HAM2 to HAM3. _____	24
Figure 4.5 Close up views of HAM2 and HAM3 for the SPRC configuration. _____	24
Figure 4.6 Layout drawing of HAM2,3 for the marginally stable power recycling cavity configuration. Red indicates the path of the main laser; optical lever beams are shown in blue. _	25
Figure 4.7 Another view of the MSPRC layout looking from HAM2 to HAM3. Red indicates the path of the main laser; optical lever beams are shown in blue. _____	26
Figure 4.8 Close up views of HAM2 and HAM3 for the MSPRC configuration. _____	27
Figure 4.9. MC front baffle _____	27
Figure 4.10. MC side baffle. _____	28

Figure 4.11 MC1 and MC3 with baffles. _____	28
Figure 4.12 SOS baffle for SM1, SM2, and MMT2. _____	29
Figure 4.13 SOS baffle for MMT1. _____	30
Figure 4.14 Modified LOS baffle. _____	31
Figure 4.15 MC cleaning baffle. _____	32
Figure 4.16. HAM 2 baffle. _____	33
Figure 4.17 IO baffle. _____	34
Figure 5.1 Conceptual Design of Power Control System. _____	35
Figure 5.2 Incremental transmitted power as a function of motor drive count to be used to send a control signal to the rotational motorized stage controller. Note that the x-axis is units of 10^4 counts. _____	36
Figure 5.3 Power in W measured at a detector of 1 cm^2 area placed at 18.5 cm from the beam dump as a function of angle from the normal to the beam dump. The blue squares are experimentally measured powers for the Kentek beam dump; the red circles are experimentally measured powers from a home-made beam dump described in the text. _____	39
Figure 5.4 UF-made beam dump for ultra-low scattering/reflection high power laser power absorption. _____	40
Figure 5.5 Experimental results showing the transmission (1 pass attenuation) of the low scatter beam dump. _____	41
Figure 6.1 Equivalent circuit of the resonant circuit / impedance matching network. _____	44
Figure 6.2 Parallel modulation using a Mach-Zehnder interferometer. _____	46
Figure 6.3 AdvLIGO frequency stability requirements _____	48
Figure 6.4 Stability requirement for MZ differential mode _____	48
Figure 6.5 Experimental MZ layout. Photo (left) and schematic drawing (right). _____	50
Figure 6.6 Modified impedance matching circuit with DC input and EOM in separate housings. _____	50
Figure 6.7 Schematic servo design with slow and fast actuator output. _____	51
Figure 6.8 Closed-loop noise suppression TF _____	52
Figure 6.9 Monolithic realization of MZ _____	53
Figure 6.10 Complex modulation _____	54
Figure 6.11 Schematic experimental setup. Inset in lower right corner shows the two EOMs. _____	54
Figure 6.12 Left: Phase Modulation. Right: Single sideband from complex modulation. _____	55
Figure 7.1 Diagram of the input mode cleaner, defining the names of the mirrors. _____	56
Figure 7.2 Calculated input mode cleaner transmission as a function of frequency, one FSR above the carrier. The left panel shows the spectrum on a broad frequency scale and a logarithmic scale for the transmission; the left panel shows the detail. _____	62
Figure 7.3 Transmission of MC Cavity _____	64
Figure 7.4 Predicted MC Frequency noise properties. _____	68
Figure 8.1 Power-dependent optical isolation for FI using one TFP and CWP (blue diamonds) and a pair of CWPs (red triangles) _____	70
Figure 8.2 Isolation degradation with the pressure at 104 W, 50 W and 30 W. _____	72

Figure 8.3 Prism moving perpendicular to the beam.	74
Figure 9.1 Marginally Stable Recycling Cavity Optical Layout. $MMT_{1,3}$ are located on HAM_2 ; MMT_2 is located on HAM_3 . Ring Heater (RH) of DKDP is used for adaptive adjustment.	78
Figure 9.2 Modal Space showing the beam waist location and beam waist size inside the arm cavity as ITM and ETM ROC are varied from 2076 m to 2137 m exploring every possible combination of the two cavity mirrors. The solid lines are the contour of constant ITM ROC.	81
Figure 9.3 Improved mode matching as a result of repositioning MMT_2 mirror to correct static errors in MMT_2 and MMT_3 ROC. The lines are contour of constant mode matching. The worst case mode matching is 99.6%.	83
Figure 9.4 Optimal ROC required at DKDP via RH for improving the mode matching. The resultant mode mismatch becomes less than 0.25% if we apply the required correction at the DKDP for a given value of residual thermal lensing in FI.	85
Figure 9.5 Conceptual layout of DKDP RH design. The parabolic groove will ensure that a constant flux from the heating Nichrome wire element incident on the rim of DKDP.	86
Figure 9.6 Sensing and control of adaptive mode matching in the IOO. Steering mirror SM_3 , BS, and Quad photodetector are located in vacuum while the lens and the CCD camera are located outside the vacuum chamber. A control servo converts the beam width data to four control signals to the four DKDP RHs.	86
Figure 9.7 Beam radius at CCD in Figure 9.6 as a function of residual thermal lensing in FI, DKDP, and MC mirrors.	87
Figure 9.8 Optical layout of Stable Power Recycling Cavity. PRM and MMT_3 are located on HAM_2 ; MMT_2 is located on HAM_3 . The main difference between SPRC and MSPRC is the position of the PRM. In SPRC, PRM replaces MMT_1 .	88

Abstract

This document presents aspects of the Preliminary Design for the Advanced LIGO Input Optics Subsystem relating to power control, overall modulation method, the input mode cleaner, and the mode matching telescope as well as ancillary IO functions. The IO preliminary design is consistent with the requirements listed in LIGO-T020020-00-D, “Input Optics Subsystem Design Requirements Document.” The Input Optics Subsystem includes the RF modulation of the light, the input mode cleaner, optical isolation, mode matching of the light to the interferometer, and beam steering into the interferometer. The scope of the IO includes the following hardware: phase modulation Pockels cells, photodetectors and related protective shutter, active jitter suppression system, input mode cleaner optics, suspensions, Faraday isolator, and mode matching telescopes.

This document does not address the electro-optic modulators or Faraday Isolators in any detail; their preliminary design was presented in “Upgrading the Input Optics for High Power Operation”, LIGO T060267-00-D.

1 Introduction

1.1 Purpose

This document along with supporting analysis documents presents the current design status for the Advanced LIGO Input Optics. The design information in this document supersedes that presented in the IOO Conceptual Design and are intended to present a detailed preliminary design for the LIGO Input Optics Subsystem which conform to the *Advanced LIGO Input Optics Design Requirements*, LIGO-T020020-00-D. The intended audience for this document is the LIGO Detector Team.

1.2 Scope

This document details the current status of the Input Optics design effort. The IO provides for the conditioning of the laser light after the PSL and before the IFO input, and for the disposition of the IFO reflected light to the ISC subsystems. It includes power control into the interferometer, RF phase modulation of the light for the generation of length and alignment control sidebands; mode-matching, a mode cleaner cavity for spatial as well as amplitude and frequency filtering of the PSL beam; mode matching of the light to the IFO; beam steering into the IFO; and diagnostic beam pick-offs for the ISC subsystems.

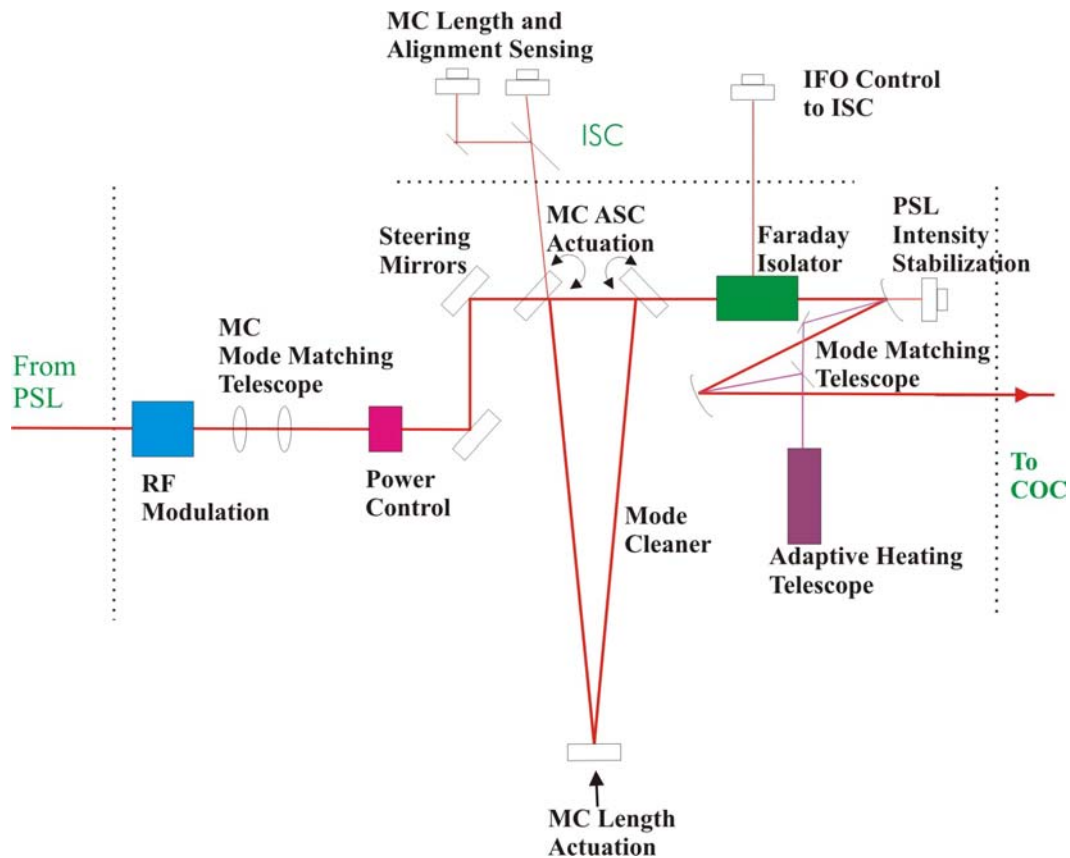


Figure 1.1. Block Diagram of the Input Optics

1.2.1 IO Subsystems

The Input / Output (IOO) subsystem layout consists of the following units, schematically shown in Figure 1:

- Outside vacuum
 - RF modulation
 - Power control into the IFO
 - Steering and mode matching optics for the input mode cleaner
 - Required IO diagnostics
- In vacuum
 - Input mode cleaner cavity
 - IFO mode matching and beam steering
 - Faraday isolation and signal extraction for ISC
 - Signal extraction for PSL intensity control

1.3 Definitions

- Modulation index m : The application of RF sidebands using an EOM results in a modulated output field $E_{mod} = E_{in} \exp[-i\omega t - i m \cos \Omega t]$ where ω and Ω are the carrier and modulation frequencies and E_{in} is the input field amplitude.

1.4 Acronyms

AM	Amplitude Modulation
AOS	Auxiliary Optics Support (detector subsystem)
BS	Beamsplitter (optical component)
CD	Conceptual Design
CDS	Control and Data System (detector subsystem)
CMRR	Common Mode Rejection Ratio
COC	Core Optics Components (detector subsystem)
DC	Direct Current (steady state - low frequency)
EOM	Electro-Optic Modulator (optical hardware)
ETM	End Test Mass (optical component)
FI	Faraday Isolator (optical component)
GPM	Gallons Per Minute (flow rate)
GW	Gravitational Wave
HAM	Horizontal Access Module
HWP	Half-Wave Plate (optical hardware)
IFO	LIGO Interferometer
IMC	Input Mode Cleaner (formerly, just the ‘MC’)
IO	Input Optics (detector subsystem)
ISC	Interferometer Sensing / Control (detector subsystem)
ITM	Input Test Mass (optical component)
LOS	Large Optic Suspension
LVEA	Laser and Vacuum Equipment Area
MMT	IFO Mode Matching Telescope
MSPRC	Marginally Stable Power Recycling Cavity

MZ	Mach-Zehnder Interferometer
Nd:YAG	Neodymium doped Yttrium Aluminum Garnet
PDH	Pound-Drever-Hall
PM	Phase Modulation
PSL	Pre-Stabilized Laser (detector subsystem)
PZT	Piezo-electric Transducer (mechanical hardware)
RC	Radius of Curvature of a Reflective Mirror
RF	Radio Frequency
RM	Recycling Mirror (detector subsystem)
SEI	Seismic Isolation (detector subsystem)
SM	Suspended Steering Mirror
SOS	Small Optic Suspension
SPRC	Stable Power Recycling Cavity
TBD	To Be Determined
TCS	Core Optics Thermal Compensation System
TGG	Terbium-Gallium-Garnet (optical material used in Faraday Isolators)
TFP	Thin Film Polarizer (optical hardware)
WFS	Wave Front Sensors

1.5 Applicable Documents

1.5.1 LIGO Documents

Advanced LIGO Input Optics Preliminary Design Document, LIGO T-020020-00-D

Advanced LIGO Input Optics Conceptual Design Document, LIGO T-020027-00-D

Advanced LIGO Input Optics Subsystem: Design Requirements Review Panel Report, LIGO-T020065-02-R

Upgrading the Input Optics for High Power Operation, LIGO- T060267-00-D

Response to EOM-FI Preliminary Design Action Items, LIGO T060081-00-D

Modulators and Isolators for Advanced LIGO, LIGO-G060361-00-D

Effect of sideband of sideband on 40m and Advanced LIGO, LIGO-G040081-00-R

Analysis of Stray Magnetic Fields from the Advanced LIGO Faraday Isolator, LIGO T060025-00-Z

1.5.2 Non-LIGO Documents

E. Khazanov, N. Andreev, A. Mal'shakov, O. Palashov, A. Poteomkin, A. M. Sergeev, A. Shaykin, V. Zelenogorsky, Igor Ivanov, Rupal Amin, Guido Mueller, D. B. Tanner, and D. H. Reitze, "Compensation of thermally induced modal distortions in Faraday isolators", IEEE J. Quant. Electron. **40**, 1500-1510 (2004).

V. Quetschke, J. Gleason, M. Rakhmanov, J. Lee, L. Zhang, K. Yoshiki Franzen, C. Leidel, G. Mueller, R. Amin, D. B. Tanner, and D. H. Reitze, Adaptive control of laser modal properties", Opt. Lett. **31**, 217-219 (2006).

2 Overview of Design Status

We believe that the IO design is substantially complete at the Preliminary Design level. Several of the IO components will be tested in Enhanced LIGO, including the electro-optic modulators and the Faraday Isolator.

2.1 Summary of the design changes from the Conceptual Design

Since the completion of the IO Conceptual Design in April 2002, there have been the following changes to the IO design:

2.1.1 In-vacuum Layout

Several changes have been made to the in-vacuum layout. Due to the relocation of HAM3 (\rightarrow HAM1) and the movement of the ISC sensing table into HAM 1, the beam injection from the PSL table has changed. As of this writing, the injection path has not been completely determined but it will most likely be through HAM1

In addition, the ISC group is considering the possibility of changing from unstable to stable power and signal recycling cavities. A change in the PRC would affect the IO since the mode matching telescope would be integrated within the PRC. While the marginally stable is still the baseline, we have developed a preliminary design level layout for the stable recycling cavity.

2.1.2 Modulation Method

The double demodulation length sensing scheme initially posed by ISC was discovered to be compromised by serial modulation (the ‘sidebands-on-sidebands’ problem) during work at the 40 m.¹ Thus, we have developed modulation schemes which do not produce sideband cross products.

Most of the preliminary design work has focused on developing requirements for and prototyping a Mach-Zehnder (MZ) modulation scheme. Some effort has also been directed at complex modulation methods (combined AM/PM) modulation.

We adopt the MZ modulation as the baseline for the preliminary design.

2.1.3 Reduction in the IMC finesse

The IO CD proposed a finesse of ~ 2000 for the IMC was conservative based on expected performance of the PSL pointing and required jitter suppression. The high finesse coupled with high input powers results in very high intracavity powers (~ 100 kW) and peak intensities on the mirror surfaces (~ 700 kW/cm²). This results in 100 mW absorption assuming a 1 ppm loss which leads to some degradation of the IMC performance at the highest power operating power.² In order to reduce the thermal loading on the IMC and relax the tolerances on mirror coatings:

We adopt a finesse of 500 for the Advanced LIGO input mode cleaner.

¹ O. Miyakawa, “Effect of sideband of sideband on 40m and Advanced LIGO”, LIGO-G040081-00-R

² Franzen Melody work

Assuming that the required jitter specification of $\varepsilon_1 \sim (3 \times 10^{-5}/f) / \text{Hz}^{1/2}$ for the PSL is met, the IMC will have no problems meeting the requirement. Recent results by the LZH and MPG groups indicate that this specification should be easily met.³

2.2 Areas that need more work

2.2.1 Complex (AM/PM) modulation

Since we have proposed MZ modulation as the baseline for AdvLIGO, we have put more effort into developing requirements and prototyping that system. An alternative modulation system based on the use of a single amplitude modulator and phase modulator is also possible.⁴ We have performed experiments and modeling on the complex modulation at a level commensurate with a conceptual design, but not yet to the full maturity of a preliminary design.

2.2.2 Faraday Isolator Performance in Vacuum

A recent test of the isolation ratio as a function of vacuum pressure revealed a significant deterioration ($47 \rightarrow 30$ dB) of the performance for when the pressure is decreased to 10^{-4} Torr at 100W power levels. Although there are still investigations to do, we believe that the culprit is poor thermal contact between the optical components (TGG, polarizers) and casings and mounts.

This is a high priority which we are actively investigating since the effect also impacts Enhanced LIGO somewhat.

2.2.3 Adaptive Mode-matching

The design of the mode matching telescope is fairly mature, including distances, mirror specifications and tolerances, etc. The adaptive mode matching concept has been changed recently from our original idea of CO₂ heating of the MMT mirrors to a four segment ring heater on the FI DKDP. Preliminary modeling has been done, but we have not yet experimentally tested the idea.

2.2.4 IO Baffling

AOS and IO recently redefined the interface to put the beam dump, suspension protection, and scattered light baffling for the IO in the IO subsystem. Since this scope change just occurred, not much has been done on this.

2.3 Areas that have been de-emphasized

2.3.1 Active jitter suppression

The IO CD proposed high bandwidth active jitter suppression using electro-optic actuators (RTP-prisms) to complement the passive suppression provided by the IMC. As noted above, we have reduced the IMC finesse to mitigate thermal effects, and do not believe that these will be necessary.

³ LIGO G070137-00-Z “Status of the Advanced LIGO PSL Development”, Benno Willke

⁴ V. Quetschke, “Complex Optical Modulation”, LIGO [G060452-00-Z](#)

In the event that more jitter suppression is needed, we will to develop and prototype an active jitter suppression system based on RTP prisms.

3 Interfaces with other subsystems

This section contains the IO interfaces with other subsystems, including:

- Optical
- Electrical/Electronic
- Mechanical
- Water

3.1 PSL

3.1.1 Optical

3.1.1.1 Main Beam

The output beam from the PSL will be delivered to IOO at $(X,Y,Z) = (144'', 50'', 3'')$ in the optical table local coordinate system defined in Figure X. The spot size at the beam waist, of the PSL output beam shall be **TBD** mm. The PSL output beam waist location shall be within 5.0 cm of the PSL output beam location.

The polarization of the beam shall be ‘p’.

3.1.1.2 PSL Intensity Stabilization Beam

The intensity stabilization beam for the PSL will be delivered to the PSL photodiode located (**TBD PSL/ISC**) on the ISC seismic platform in HAM 1(7). At the IOO/PSL interface location, the spot size of the IOO output beam sample for power stabilization shall be **TBD PSL/IOO**. The power of the beam shall be **TBD PSL/ISC**.

3.1.2 Mechanical

The IOO shares an optical table with the PSL (PSL/IOO table). Components of the IO that are located on the PSL table include

- modulation
- power control
- mode matching optics for the IMC,
- periscope and beam injection optics
- diagnostics

Figure 3.1 shows the allocation of table area for each subsystem. The optical table itself as well as the physical enclosure surrounding the table (for controlling acoustic noise, air currents, dust, and thermal variations) is the responsibility of the PSL subsystem.

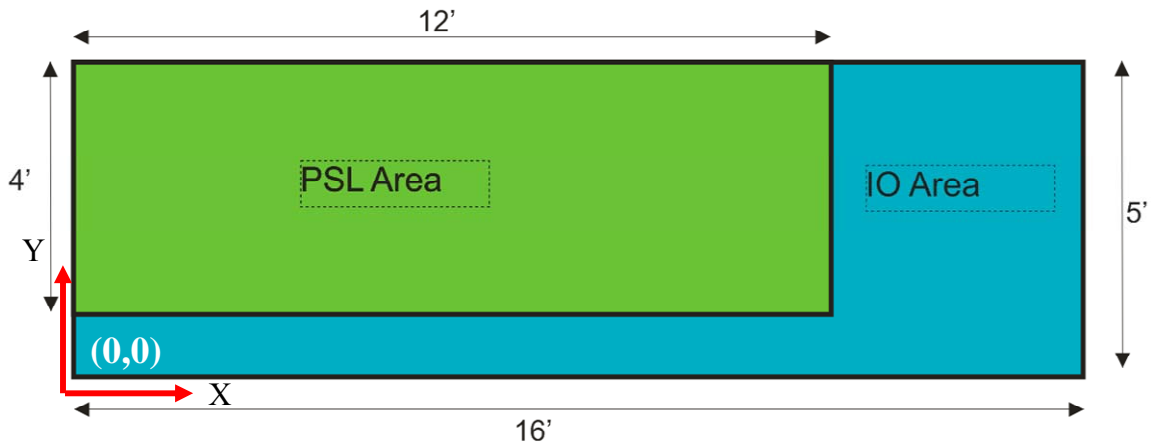


Figure 3.1 Defined IO and PSL areas on the PSL table,

3.1.3 Water

The IFO power control beam dump must dissipate 180W of power. Thus water-cooled beam dumps are required. We require inlets and outlets with a flow rate of 0.5 GPM through a 1/4" outer diameter tube to the IO power control beam dump.

3.2 COC

3.2.1 Optical

The IO delivers the main beam to the power recycling mirror (PRM) at $(X,Y,Z) = (-3930.48\text{mm}, 222.355\text{mm}, -156.562\text{mm})$ in LIGO Global Coordinates and direction cosines $(\theta_x, \theta_y, \theta_z) = (1, -0.0000951851, -2.5693 \times 10^{-14})$.

3.3 ISC/CDS

3.3.1 Optical

3.3.1.1 Interferometer Length and Alignment Sensing Beams

The IOO delivers diagnostic beams for interferometer length and alignment control to the ISC subsystem (REFL port) from Faraday Isolators located in HAMs 2,8 to the ISC sensing tables in HAM1,7 (TBD/ISC). These beams will have spot sizes of 2 mm (TBR ISC/IO) with nominal powers of TBD ISC mW and up to TBD ISC W during lock acquisition of the IFO.

3.3.1.2 IMC length and alignment sensing beams

The IO delivers diagnostic beams for IMC length and alignment control to the ISC subsystems (IMC_REFL port) using the reflected beam from IMC1 to the ISC sensing tables in HAM1,7 (TBD/ISC). These beams will have spot sizes of 2 mm (TBR ISC/IO) with nominal powers of 300 mW and up to 6 W during lock acquisition of the IFO.

3.3.2 Mechanical

IO mode matching sensors for measuring laser-induced thermal distortions in the IO optical components will be located on sensing tables in HAMS 1,7.

3.3.3 Electrical

3.3.3.1 RF modulation

The RF modulation signals for the two interferometer control sidebands and the IMC sideband are supplied to the IO EOMs from ISC/CDS. IOO will use in-house resonant RTP electro-optic phase modulators⁵ with the following characteristics:

- Electro-optic crystal: RTP
- Maximum Optical Power: 7 kW/cm²
- Modulation Depth : 0.071 rad/V (depends on frequency; assumes matching circuit with Q=20, 20 mm long, 4 mm thick RTP crystal)
- Aperture: 4 mm
- Electrical Input Impedance: 50 Ω

At the time of this review, the choice of modulation frequencies is still under discussion by the ISC group. The signal characteristics are given in Table 1.

Table 1 Required RF inputs to IO EOMs.

<i>Sideband</i>	<i>Frequency (MHz)</i>	<i>Max. Modulation Index</i>	<i>Voltage</i>	<i>RF Power, RMS (in 50 Ω)</i>
Upper IFO control sideband	9 (TBR ISC)	0.8 (TBR ISC)	10 V (TBR ISC)	2 W (TBR ISC)
Lower IFO control sideband	45 (TBR ISC)	0.8 (TBR ISC)	10 V (TBR ISC)	2 W (TBR ISC)
IMC control sideband	31.457 (TBR IO)	0.03	0.5 V	5 mW

3.3.3.2 Automated Power Control

The IO provides power control of the PSL into the interferometer for commissioning as well as different operational modes of the interferometers. The CDS will provide control signals for rotating a 1/2 wave plate (see section 5.2.1.3). A motorized stage Newport URS-100 CC is controlled via an ESP 300 controller with a GPIB/RS232 interface. A script containing appropriate commands can be used to drive the ESP 300, or alternatively direct connection to the URS-100 CC can be used.

⁵ IO HIGH POWER UPGRADE DOCUMENT

3.4 SEI

3.4.1 Mechanical

All in-vacuum IO components are located on seismic isolation platforms in HAMs 2,3 and HAMs 8,9.

3.5 AOS

3.5.1 Optical

There are eleven optical lever beams from AOS that interface with the IO subsystem. There is one optical lever on each of the suspended optics (IMC1, IMC2, IMC3, SM1, SM2, MMT1, MMT2, MMT3, and PRM), and one optical lever for each HAM table (HAM 2 and HAM 3).

3.6 SUS

SUS supplies the IMC triple suspensions and MMT3 LOS-type suspension to the IO. All small optics suspensions (for SMs, small MMT mirrors) will use LIGO 1 small optics suspensions (SOS) manufactured by UF.

4 Optical Layout

This section includes the status of the physical layout of the IO components for Advanced LIGO.

4.1 Assumptions

We assume that the LIGO facilities meet the specifications for vibrational and acoustic noise given in the Civil Construction Facilities *Design Configuration Control Document*, LIGO C960703-0.

4.2 PSL Table Layout

The layout of IO optical components on the PSL table is shown in Figure 4.1 and Figure 4.2. All beam paths will be enclosed in either beam tubes or plexiglass enclosures to minimize environmental effects. Red represents the main beam, and green represents beams that will be dumped or used for diagnostics.

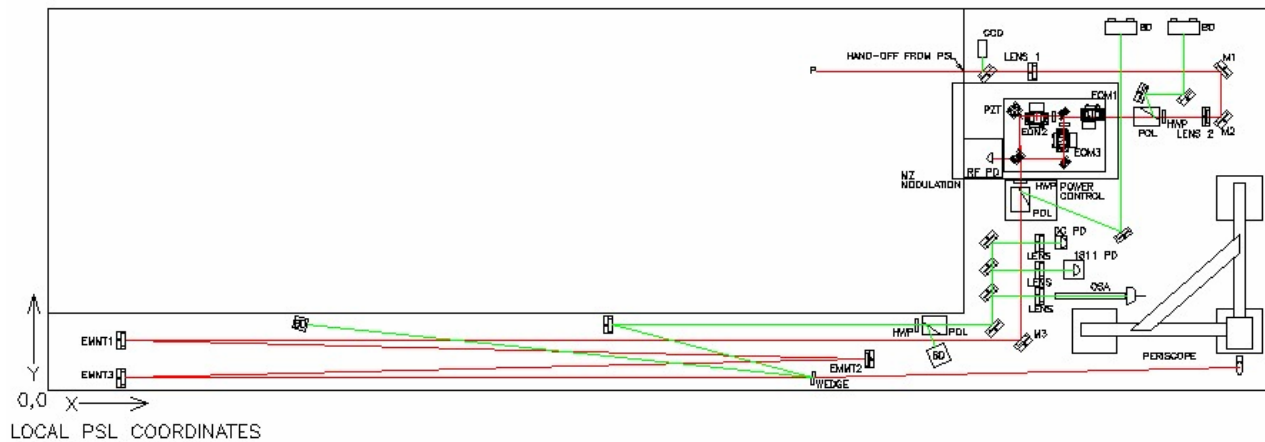


Figure 4.1 Diagram of the PSL Table showing IO components

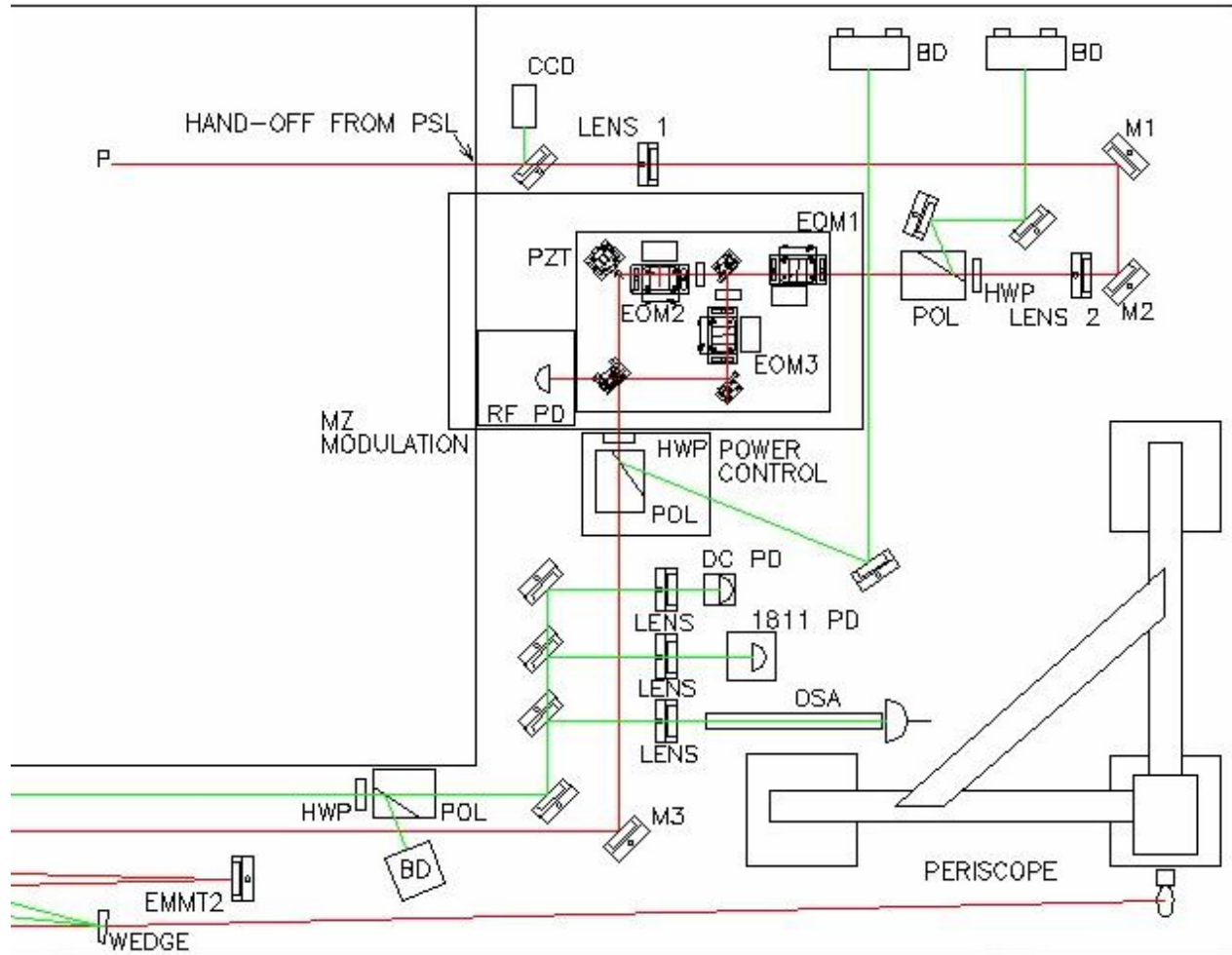


Figure 4.2 Blow up of the main area of the IO components on the PSL table showing functional blocks of IO components.

4.2.1 Optical Components

4.2.1.1 General Characteristics

4.2.1.1.1 Optical components

All transmissive optical components (excepting modulators and wave plates) will use fused silica for minimal thermal distortions.

4.2.1.1.2 Kinematic mirror mounts

Newport Ultima®/Suprema® kinematic mounts or Linos Lee's mounts will be used for all in-air mirror mounts in the IO subsystem.

4.2.1.2 Optical Component Dimensions

Table 2 gives the physical dimensions and clear apertures for the optical components on the IO table.

Table 2 Summary of PSL table optical component sizes

<i>COMPONENT</i>	<i>PHYSICAL DIAMETER (MM)</i>	<i>CLEAR APERTURE (MM)</i>	<i>COMMENTS</i>
Lens	50	45	
0° beam path mirror	50	45	
45° beam steering mirrors	50	35	
Wave Plate	25	20	
Thin Film Polarizer	50	27.5	Brewster angle
MMT mirrors	50	45	
MZ Beamsplitter	50	35	
MZ active mirror	10	8	Low mass for High Loop Gains for MZ LSC servo

4.2.2 Laser Beam Injection Periscope

At the time of this writing, the injection of the laser beam into the vacuum system is still under discussion, with the possibility of injecting the beam either beneath HAM1,7, above the HAMS, or through HAM1,7. The IO group has a strong preference for direct injection through HAM1,7. In that case, a periscope similar to that used in current LIGO⁶ will be used.

4.3 In-vacuum optical layout

4.3.1 Design Considerations

The in-vacuum layout of the IO components was driven by several considerations:

- MC length - the requirements on mode cleaner length determine the positions of the SOS in the HAMS

⁶ PERISCOPE DESIGN DOCUMENT OR DRAWING REF. D010231-A

- Positioning of the MMT mirrors - To be able to achieve the maximum independent adjustability of the mode parameters into the interferometer, we require that the mirror MMT 2 be able to move at least 20 cm forward or back along the HAM3 platform.
- Minimization of coupling of stray magnetic field (B) to the suspended IMC mirror actuators - a minimum separation distance of 30 cm between the FI and the suspension is required to reduce the displacement noise induced on the suspended mirror by B -field fluctuations to a level below the ambient displacement noise induced by seismic fluctuations.⁷
- Scattered light baffles – A large baffle plate will be located on HAM 3,9 to minimize scattered light coupling between the IO and COC. The IO components must not interfere with these baffles and visa versa.

The current state of the layouts is shown in the figures below. Lines representing beams are drawn at the 25 ppm intensity contour.

NOTE: The layouts below assume laser beam injection from HAM 1. Other variations have been discussed (injection from the floor through the bottom of HAM2, injection through side viewports), and both of these options would complicate the layout issues.

4.3.2 Stable Recycling Cavity Layouts

The overall layout and close-ups of HAM2,3 are shown below.

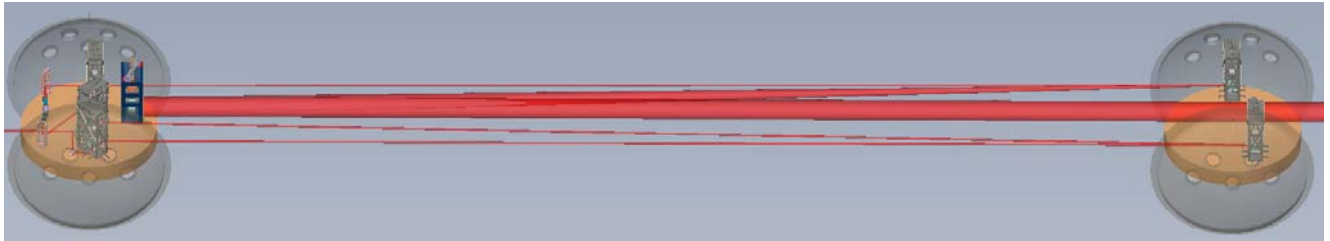


Figure 4.3 Layout drawing of HAM2,3 for the stable power recycling cavity configuration.

⁷ LIGO T060025-00-Z, “Analysis of Stray Magnetic Fields from the Advanced LIGO Faraday Isolator”, G. Mueller and S. Stepuk

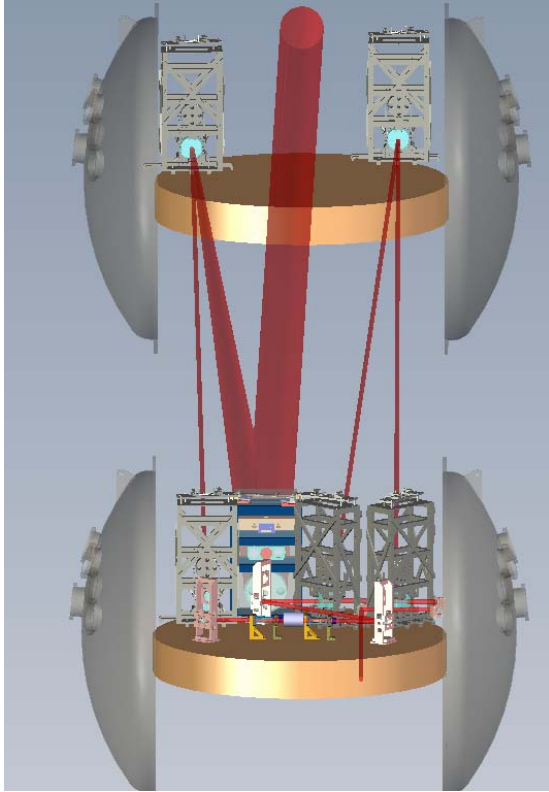


Figure 4.4 Another view of the SPRC layout looking from HAM2 to HAM3.

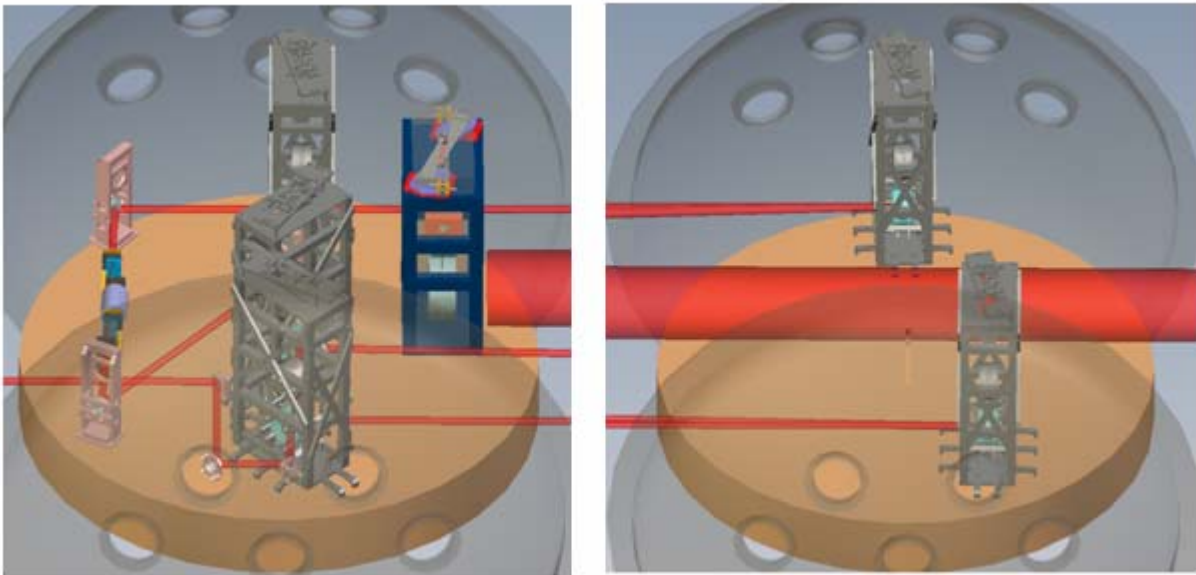


Figure 4.5 Close up views of HAM2 and HAM3 for the SPRC configuration.

4.3.3 Marginally Stable Power Recycling Cavity

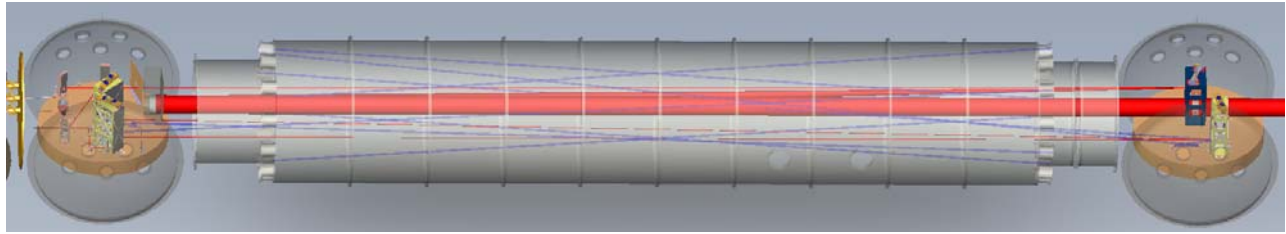


Figure 4.6 Layout drawing of HAM2,3 for the marginally stable power recycling cavity configuration. Red indicates the path of the main laser; optical lever beams are shown in blue.

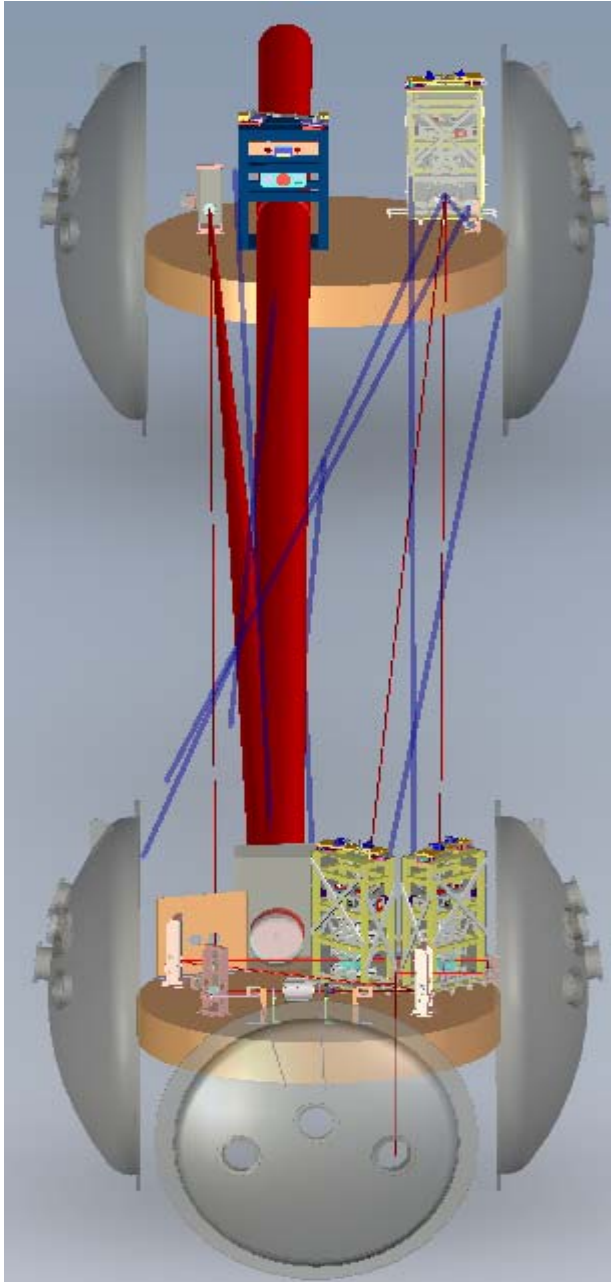


Figure 4.7 Another view of the MSPRC layout looking from HAM2 to HAM3. Red indicates the path of the main laser; optical lever beams are shown in blue.

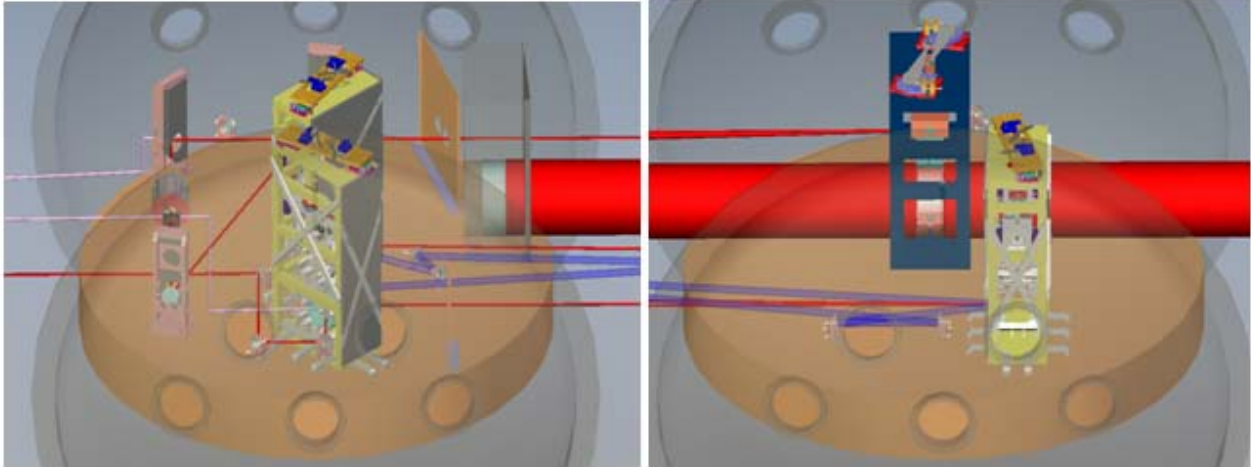


Figure 4.8 Close up views of HAM2 and HAM3 for the MSPRC configuration.

4.4 Baffles

4.4.1 MC errant beam baffles

The MC suspensions have baffles that serve two purposes. First, they protect the suspension from errant beams. Second, they provided stiffening to the MC support structure. They are made from single pieces of aluminum, which are milled to .050” thick in most locations, but are .500” thick in areas where diagonal bracing is needed. These baffles are placed only on the sides of the suspensions that need protection from errant beams.

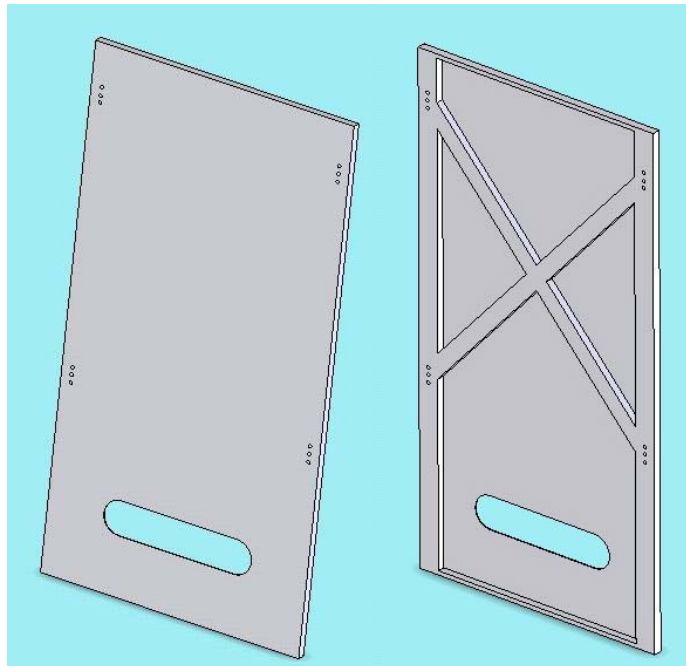


Figure 4.9. MC front baffle

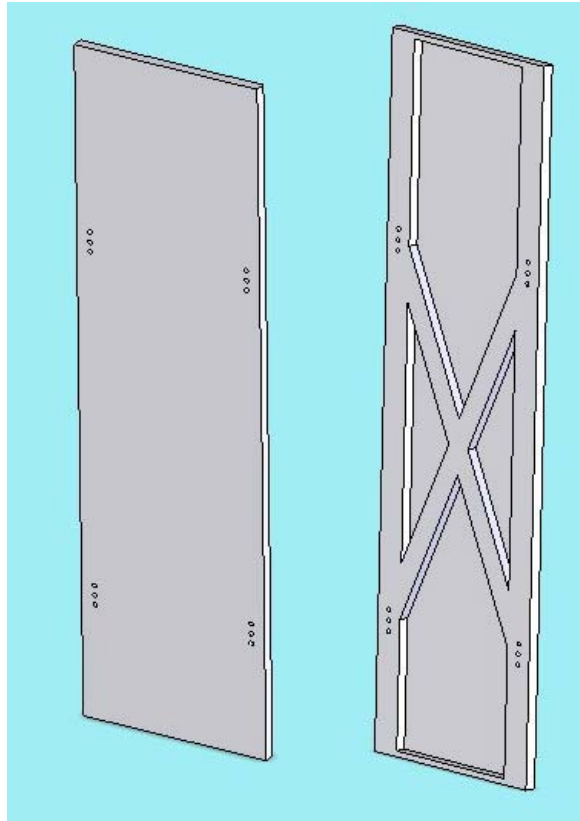


Figure 4.10. MC side baffle.

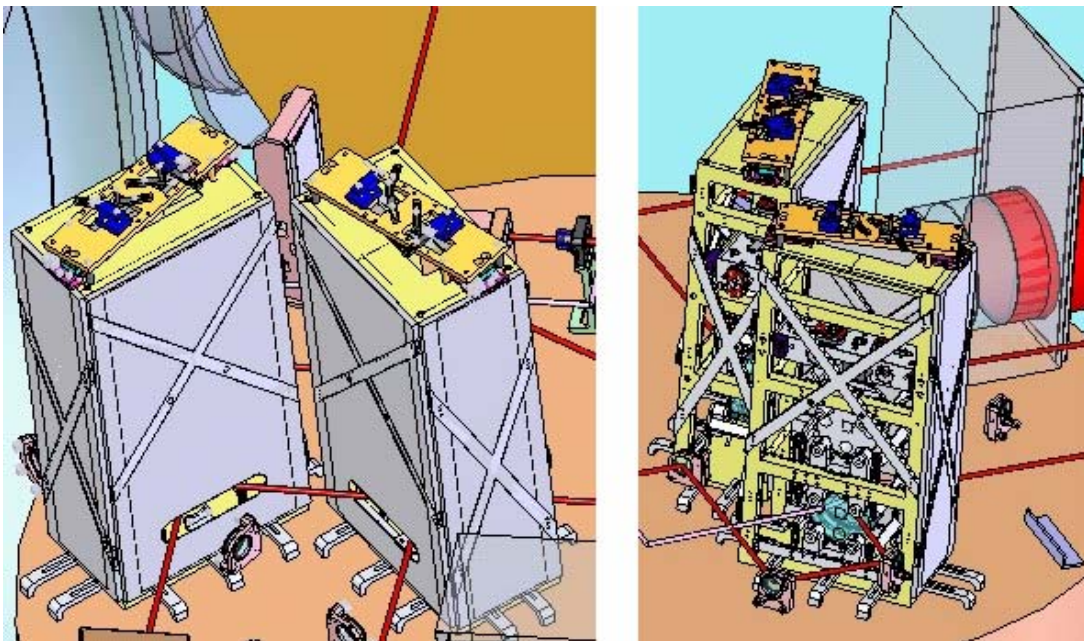


Figure 4.11 MC1 and MC3 with baffles.

4.4.2 SOS baffles

The SOS baffles protect the suspensions from errant beams. They are made from either bent (SM1, SM2, MMT2) or flat (MMT1) sheet metal. The baffle on MMT1 is flat because of the large angle of incidence of the beam. The type of metal is not yet determined, but must have high thermal conductivity to prevent overheating.

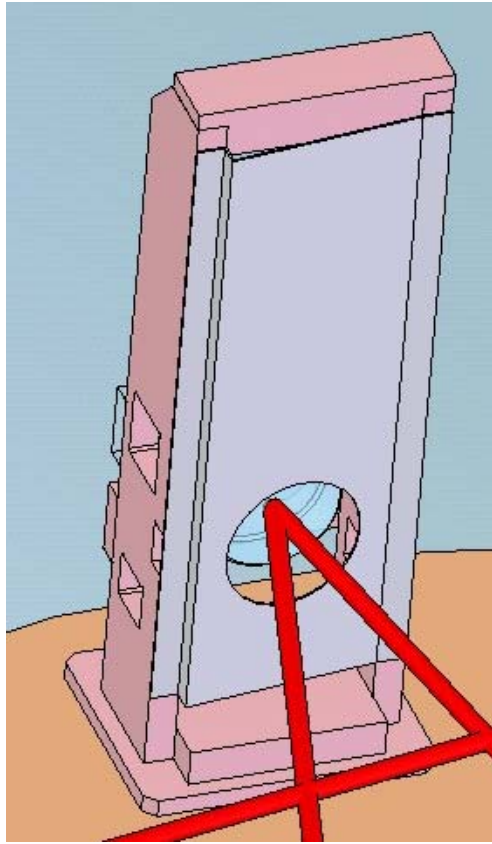


Figure 4.12 SOS baffle for SM1, SM2, and MMT2.

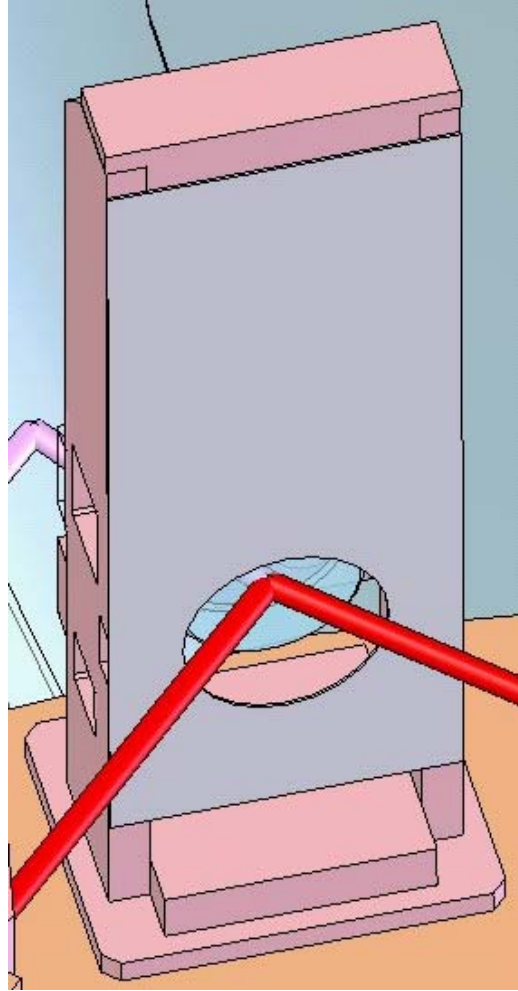


Figure 4.13 SOS baffle for MMT1.

4.4.3 Modified LOS baffle

The modified LOS baffle is used to protect the MMT3 suspension from errant beams. It is similar in design to the bent SOS baffles, just on a larger scale.

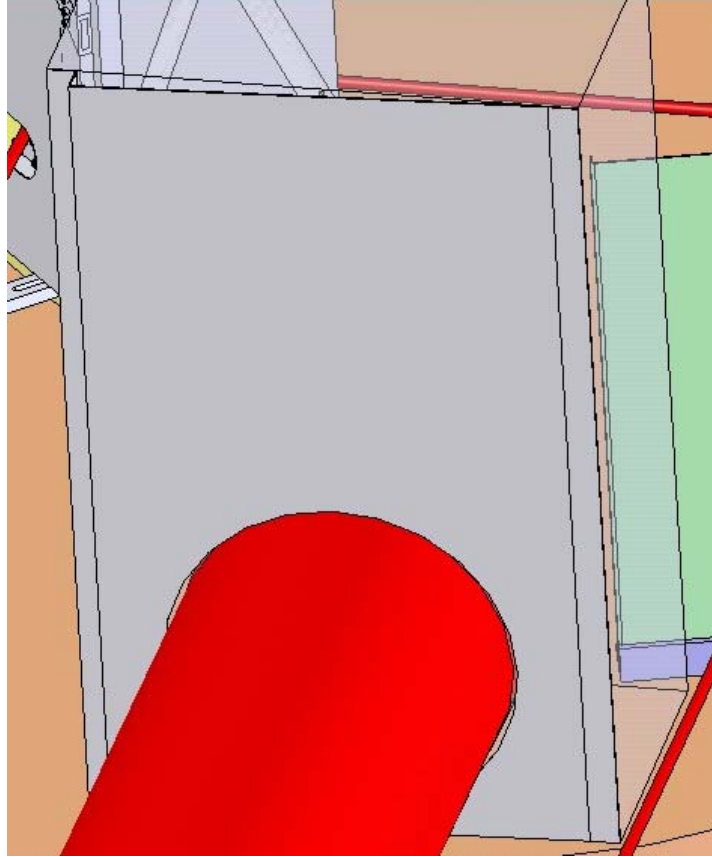


Figure 4.14 Modified LOS baffle.

4.4.4 MC cleaning baffle

The MC cleaning baffle is an aperture used to clean light circulating off path in the MC. The material is TBD.

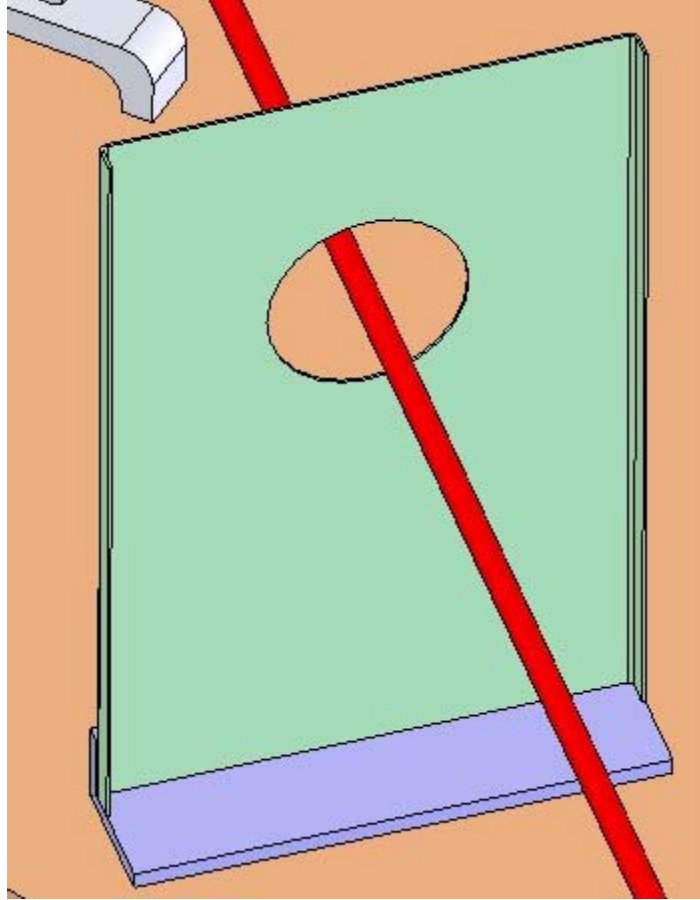


Figure 4.15 MC cleaning baffle.

4.4.5 HAM 2 baffle

The HAM 2 baffle is used to protect the various wires and electronics in HAM 2 from an errant beam returning from HAM 3. Once the locations and sizes of the wires are determined, this baffle may be replaced with smaller individual baffles at those locations. The second hole in the baffle is to allow a heating beam to pass through, in the event that the MMT2 is heated. The material is TBD.

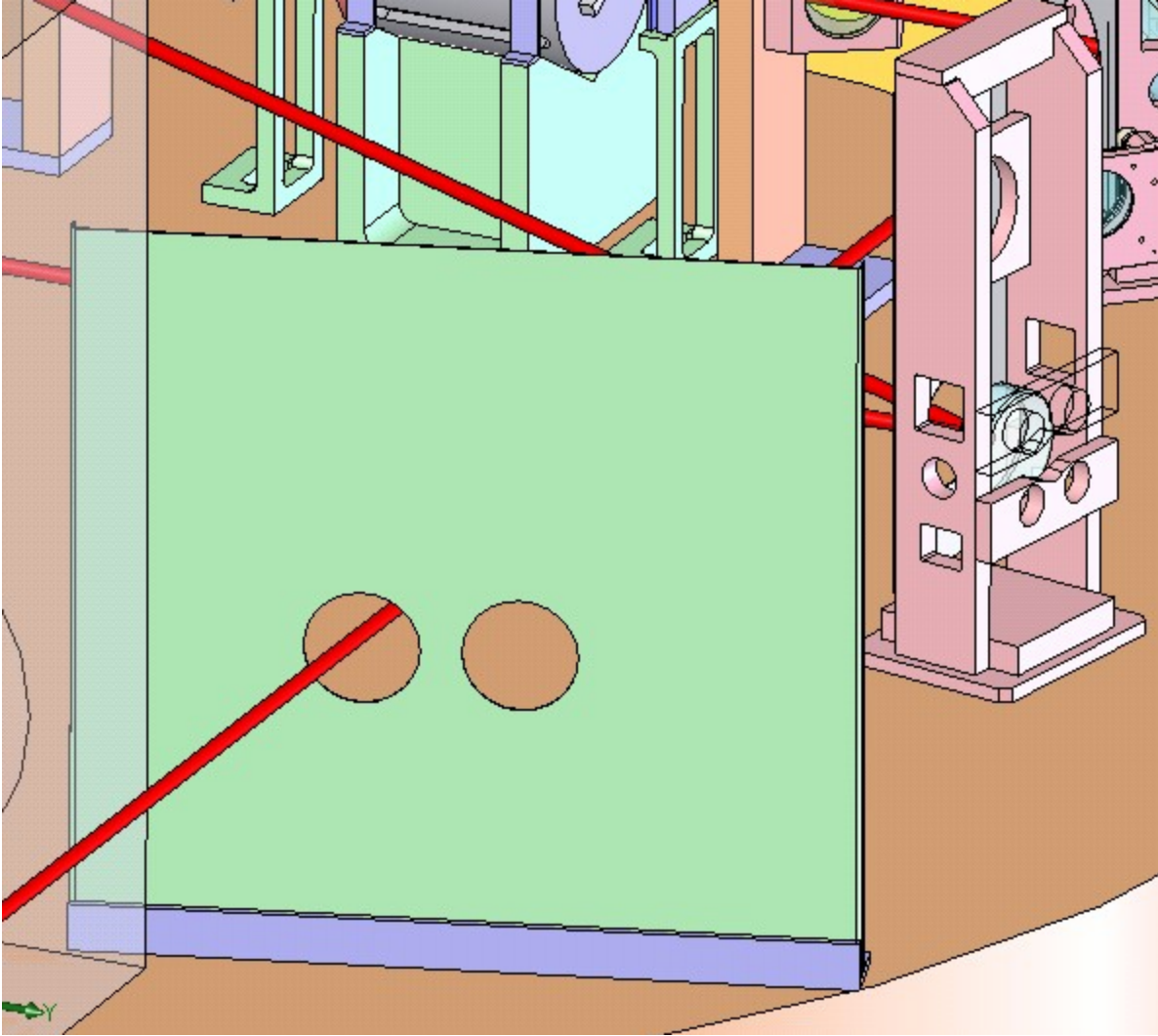


Figure 4.16. HAM 2 baffle.

4.4.6 IO baffle

The IO baffle is used to separate the IO section from the COC section. Figure 4.17 shows the basic shape required of the IO baffle, but it will need to be broken into several pieces in order to allow for changes in the placement of MMT2, and to cover the full beam tube aperture without contacting the ceiling of the HAM chamber.

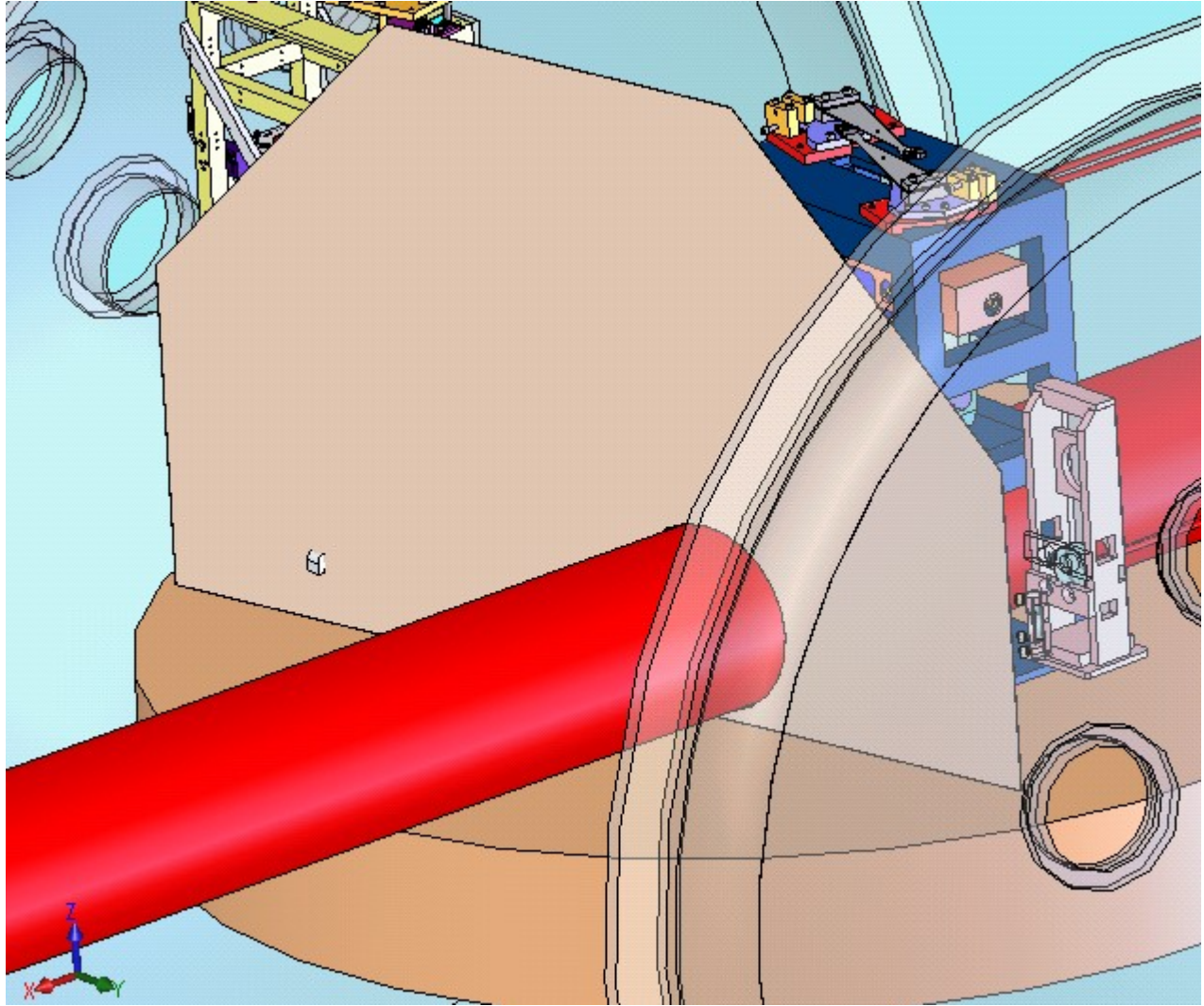


Figure 4.17 IO baffle.

5 Power Control Subsystem

A power control system similar to that employed in the current LIGO interferometers will provide continuously adjustable variable power into the interferometer without disrupting the interferometer operation. The power control system is not designed to function as an intensity stabilization servo loop system.

5.1 Requirements

The power control system should:

- provide essentially continuous power adjustment into the IMC from ~ 0 W to the maximum available power. The minimum incremental power step should be such that the resultant radiation pressure kick does not knock the IMC out of lock.
- provide an interface to CDS.
- be able to dump the excess light according to the stray light requirements of AdLIGO.

The power control system should not:

- introduce fluctuations in the output power
- unlock the interferometer or IMC undergoing adjustment

5.2 Design

We will use a design similar to that used in initial LIGO based on a polarizer and rotating half wave plate as shown in Figure 5.1.

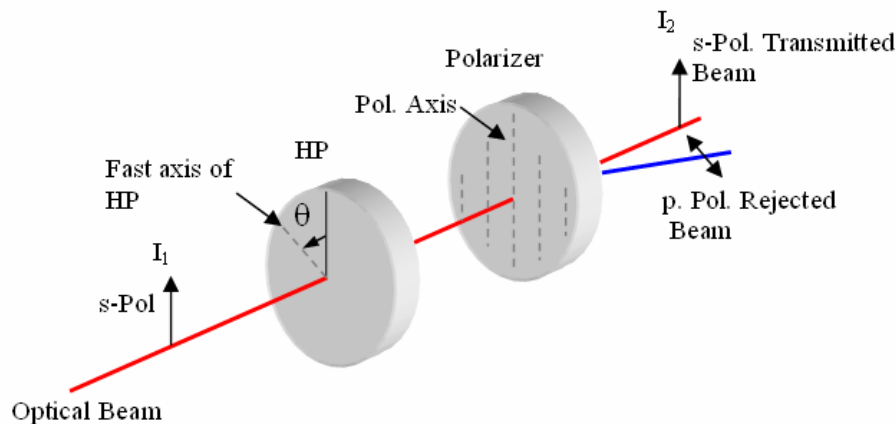


Figure 5.1 Conceptual Design of Power Control System.

The p-polarized IFO optical beam with an intensity of I_1 passes through a HP plate with fast axis at an angle θ with the vertical axis and a TFP with axis along the vertical direction. The s-polarized transmitted light has intensity I_2 while the rejected beam is horizontally ('p') polarized. The relationship is given by Malus's Law:

$$\frac{I_2}{I_1} = \cos^2(2\theta) \quad (5.1)$$

The full range of power is realized as the HP plate rotates through 0-45°. LIGO 1 uses New Focus Picomotors to rotate the 1/2 waveplate in 1 dB steps (determined by CDS software). For Advanced LIGO, a motorized rotational stepper stage (Newport URS-100 CC) can provide quasi-continuous rotation of 0.0005°/step. The corresponding incremental power change as a function of linear step is shown in Figure 5.2

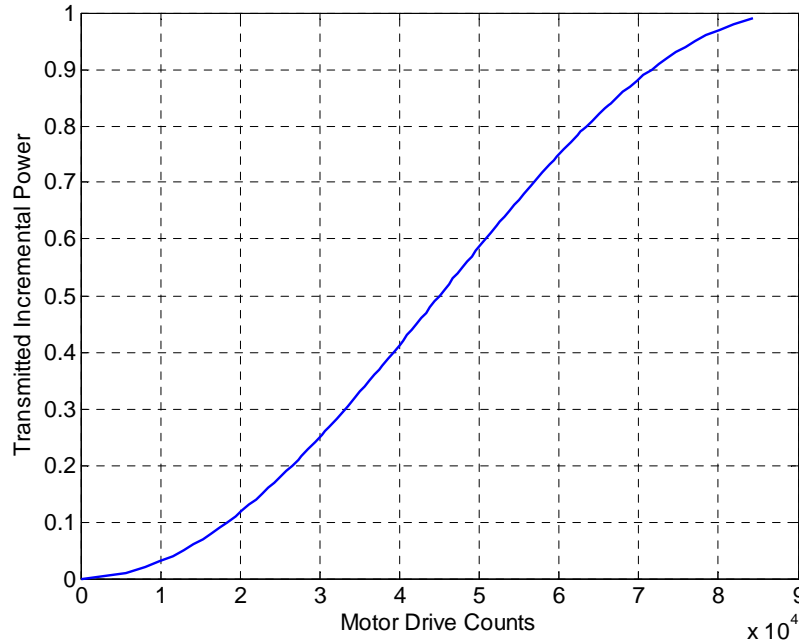


Figure 5.2 Incremental transmitted power as a function of motor drive count to be used to send a control signal to the rotational motorized stage controller. Note that the x-axis is units of 10⁴ counts.

5.2.1 Radiation pressure and IMC displacement

The IMC and IFO mirrors will be subjected to incremental radiation pressure changes as the input power is changed. Since the IMC mirrors are 20 times lighter than the TMs, since the cavity pole of the IFO is much less that of the IMC, and since the IMC stores roughly 1/4 the power of the FP arm cavities, the IMC is most susceptible to radiation pressure kicks.

Power adjustments should occur in such a manner that the incremental ‘kick’ of the mirrors does not produce longitudinal or angular displacements larger than the bandwidth of the servos used to control the length and alignment.

5.2.1.1 Length Displacement ‘Kicks’

The component of force on a mirror from light pressure that induces displacement can be written as:

$$F_{rad} = \frac{2P}{c} \cos \phi \quad (5.2)$$

where P is the power incident on the mirror, c is speed of light, and ϕ is the angle of incidence of the light on the mirror. Assuming that the cavity is on resonance (i.e., neglecting the correction from the optical spring effect) and the excitation is far above the resonance frequency of the pendulum, the induced longitudinal displacement of a mirror with respect to the cavity axis can be written as:

$$\Delta x_{cav} = \frac{F_{rad}}{\omega^2 M} \frac{1}{\cos \phi} \quad (5.3)$$

where M is the mirror mass, ω is the angular frequency, and the $\cos \phi$ term accounts for the difference between the displacement and cavity length. For the case of IMC, the $\cos \phi$ terms in the radiation force and the displacement offset each other, and the displacement kicks can be written as:

$$\Delta x_{IMC1,2,3} = \frac{2P_{in} \mathfrak{F}}{c \omega^2 \pi M} \quad (5.4)$$

where P_{in} is the input power and \mathfrak{F} is the finesse of the IMC cavity.

Table 3 Parameter Values for Triple Pendulum IMC Mirror.

Parameter	Unit	Value
P_{in}	W	0-165
IMC Mirror Mass	kg	2.9
\mathfrak{F}	-	500
Thickness	cm	7.5
Diameter	cm	15
Angular Frequency	rad/s	$2\pi \times 0.65$

To maintain lock, the radiation pressure kick must be compensated by the IMC LSC. This translates in to a requirement on the slew rate of the servo. For the LSC, we consider the worst case of 82.5 W into the IMC and the maximum power increment at the half power point (HWP set to 22.5°); this corresponds to an incremental input power change $\Delta P_{in} = 2.1$ mW/step using Eq. 5-1. The radiation pressure kick will be felt by all three IMC mirrors. Thus the total mirror displacement is additive: $\Delta x_{total} = \Delta x_{IMC1} + \Delta x_{IMC2} + \Delta x_{IMC3}$. From Eqs. 5.4, this produces a radiation pressure cavity length displacement Δx_{total} of 131.4 pm/step.

The power build-up time is limited by either the cavity pole filter, $f_{p,IMC}$, or by the speed of the stepper stage. For our design, the maximum speed of the motorized rotational stage limits dP_{in}/dt .

Multiplying the displacement/step by steps/s (1778 steps/s for Newport URS-100 CC) produces a maximum IMC mirror velocity of 0.233 pm/μs due to radiation pressure as the power is changed by rotating the HP through the motorized rotational stage. This puts a lower limit on the actuator slew rate. These actuators should be able to move the IMC mirror substantially faster than 0.08 pm/μs. Assuming a safety margin of 10, the MC servo should have a slew rate of better than 1 pm/μs.¹

5.2.1.2 Angle Displacement ‘Kicks’

If the beams are not centered on the MC mirrors, the power increase can cause an angular ‘kick’ produced by the radiation pressure torque. The torque introduced by an input Power of P_{in} in the IMC that hits a mirror at a distance, d , away from the center and the restoring torque is given by:

$$T = \frac{2P_{in}\Re d}{c\pi} = \alpha\Theta\omega^2. \quad (5.5)$$

where α is the angle, Θ is the angular moment and ω is the angular frequency in yaw. Simplifying

$$\text{Eqs. } \Delta x_{IMC1,2,3} = \frac{2P_{in}\Im}{c\omega^2\pi M} \quad (5.4) \text{ and } T = \frac{2P_{in}\Re d}{c\pi} = \alpha\Theta\omega^2.$$

(5.5) for α :

$$\alpha = \frac{2P_{in}\Im d}{c\pi\Theta\omega^2}, \quad (5.6)$$

where Θ along the orthogonal directions to the beam propagation various directions is given by $\Theta_{xx} = \Theta_{yy} = \frac{1}{4}MR^2 + \frac{1}{12}Mh^2$. Here M is the mass, R is the radius, and h is the thickness of the mirror as given in Table 3. Assuming the maximum allowed decentering of 1 mm⁸ on the MC mirror, the angular ‘kick’ is equal to 0.077 nrad/step at the half power point. Multiplying the nrad/step by the transfer function of the rotational stage, i.e., 1778 step/s given 0.137 prad/μs. Considering that there are three mirrors and assuming a safety margin of 10, a minimum of 4.2 prad/μs slew rate should be available from the IMC ASC servo loop.

5.2.1.3 CDS Control of the Input Power

Should it be found during commissioning that incremental radiation pressure due the power control system causes unforeseen problems in the interferometer, the slew rate of the power can easily be (and should be) limited in software.

5.3 Beam Dump

The rejected beam in the power control system must be disposed of properly. Although there is no formal requirement, the rejected beam (as much as 180 W) should be dumped with minimal backscatter. For beam dumps, the IO base line design is commercially available water cooled beam

⁸ Advanced LIGO Input Optics Preliminary Design Document, LIGO T-020020-00-D

dumps from Kentek (ABD-2C). The quoted specular reflectance of these beam dumps is less than 0.1%.

To verify this, we have measured the scattering of laser radiation from the commercial beam dump at 100 W input powers. The total scattered power into 2π steradian (half hemisphere) was measured to be 7.6 mW using a calibrated Ophir power meter. The measurements as a function of angle from the normal to the surface of the beam dump at a distance of 18.5 cm away from the surface are shown in Figure 5.3. A 4th degree polynomial is fitted using least squares technique and the result is integrated into 2π steradian (half hemisphere). The total power radiated into half hemisphere is found to be ≈ 10 mW.

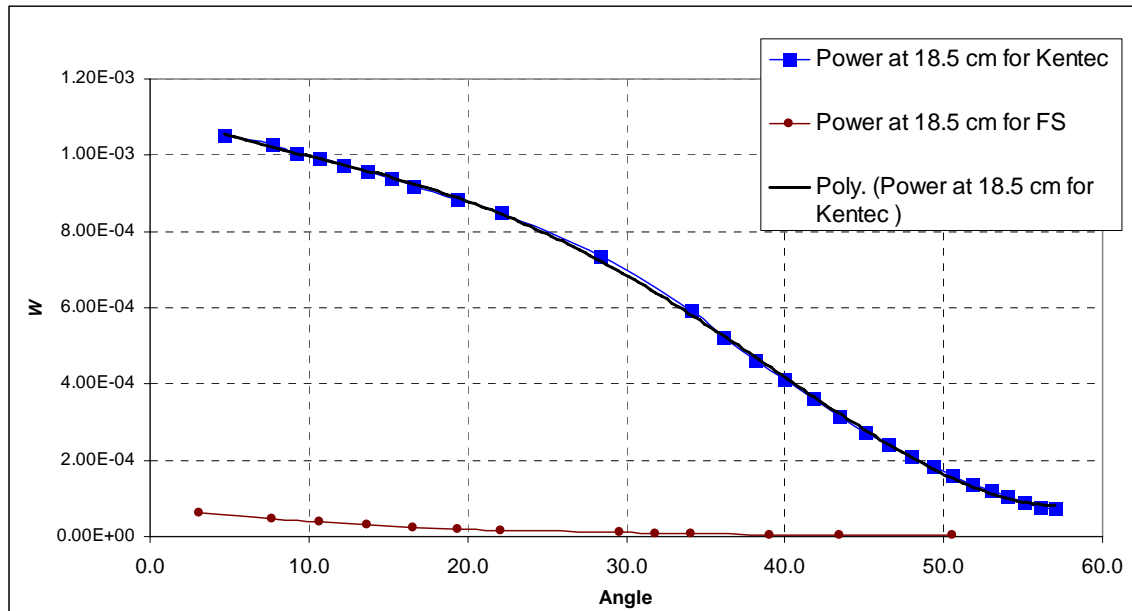


Figure 5.3 Power in W measured at a detector of 1 cm^2 area placed at 18.5 cm from the beam dump as a function of angle from the normal to the beam dump. The blue squares are experimentally measured powers for the Kentek beam dump; the red circles are experimentally measured powers from a home-made beam dump described in the text.

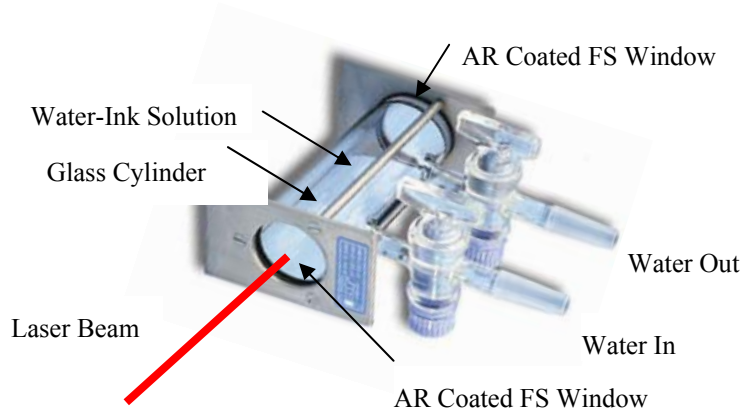


Figure 5.4 UF-made beam dump for ultra-low scattering/reflection high power laser power absorption.

5.3.1 Alternative Low Backscatter Beam Dump

An alternate ultralow backscatter beam dump has been designed and tested (Figure 5.4) using a commercially available infrared spectrometer gas cell where the light is absorbed in the circulating water containing India ink. A glass cylinder is sealed using fused silica windows at the end with AR coatings at the front and back surfaces. There are two inlets to the cylinder, one for water entering the enclosed cylinder and the other for water going out from the cylinder. An experiment was conducted using 42 W laser power and the results are shown in Figure 5.5.

As shown in Figure 5.5, a 0.8 ml/L solution of India-Ink in water in a 10 cm path can successfully dump 100 W of laser power. The non-specular back-reflectance was minimized by AR-coated fused silica windows (Figure 5.4). This option can be used if the commercially available beam dumps do not provide satisfactory requirements in terms of back-reflectance and scattering.

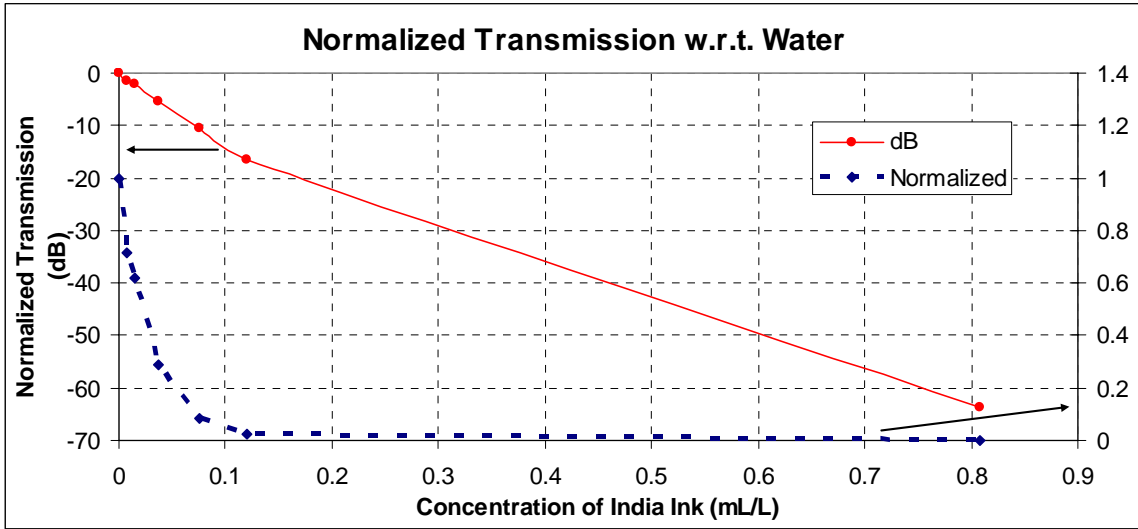


Figure 5.5 Experimental results showing the transmission (1 pass attenuation) of the low scatter beam dump.

6 RF Modulation

6.1 Introduction

RF modulation is needed to sense and control the interferometer length and alignment DOFs. Three modulation frequencies are needed, one to lock the mode cleaner and two other frequencies to extract control signals of the main interferometer (including Michelson, power recycling cavity, signal recycling cavity and arm cavities). The IO must produce and monitor these sidebands using RF signals from the ISC.

Specifically, the IO provides:

- the design, fabrication, and assembly of all RF electro-optic modulators for the production of sidebands for controlling the interferometer and mode cleaner length and alignment sensing systems;
- a ‘clean’ sideband spectrum. The modulation must avoid the sidebands on sidebands problem⁹ for the interferometer’s central part control signals (either by using a Mach-Zehnder setup or a complex modulation scheme);
- ancillary optical and mechanical components.

6.2 Baseline Design

AdvLIGO uses the same vacuum chambers as the current LIGO interferometer, thus constraining cavity lengths. The IMC FSR is set by its length to ~9 MHz. In order to pass through the IMC, the IFO control modulation frequencies must satisfy:

$$f_{mc} = n \frac{c}{2L_{mc}}$$

The modulation frequencies for the core interferometer are TBD but the current modulation schemes [6] favor either 9 MHz/108 MHz allowing still the resonant readout scheme¹⁰ or 27 MHz/45 MHz. When choosing the exact values of the modulation frequencies it is paramount that they all miss the harmonics of the 4 km arm cavity free spectral range of 37.5 kHz.

The modulation frequency to be used to lock the mode cleaner is not transmitted (heavily attenuated by the IMC) and can be considered non-critical as long as overlap with the modulation frequencies for the core interferometer is avoided. We choose a value of **31.457 MHz (TBR IO)**, for the IMC locking, about 100 kHz off the fourth antiresonance ($n = 3.5$).

⁹LIGO-T040119-00-R, “Mach-Zehnder interferometer for Advanced-LIGO optical configurations to eliminate sidebands of sidebands, O. Miyakawa, et al.

¹⁰ The upper modulation frequency is constrained by the space in the vacuum chambers that limits the maximum asymmetry in the Michelson arm length to $\Delta l < 75$ cm.

6.3 Constraints

The constraints on the modulation frequencies are mainly given by the vacuum system. The mode cleaner and recycling cavities span vacuum chambers whose separations determine the various cavity lengths.

6.4 RF modulation requirements

The requirements on optical modulation, including modulation depths, and relative stability of the modulation frequency and amplitude, for Advanced LIGO are described in the IO DRD, LIGO-T020020 and also EO-Modulators for Advanced LIGO, Part I, LIGO-T020025-00-D.

A more recent investigation was done in the LIGO-T060267-00-D document “Upgrading the Input Optics for High Power Operation”. Refer to this document for technical details of the modulator. Changes in the design/performance the AdvLIGO modulators from those ELIGO modulators are discussed in this document.

6.4.1 Modulation frequencies

The final values for the modulation frequencies are **TBD ISC**; nominal values are given Table 4 below. Section 7.2.3 lists possible combinations for the modulation frequencies for the IFO.

Table 4 Performance of the Advanced LIGO FI

	Modulation f1	Modulation f2
HF scheme	9 MHz	108 MHz
LF scheme	27 MHz	45 MHz

6.4.2 Modulation depths

Modulation depths are set by GW shot noise considerations at the asymmetric port. In addition, the IO must provide for a range of modulations about the specified depths to accommodate diagnostic functions and potential degradation.

- The IO must provide for modulation depths in the range $m = 0-0.8$.

6.5 Modulator design

We have made prototype RTP-based phase modulators using 1.5 cm long x 0.4 cm width x 0.4 cm thickness crystals. A preliminary design is given in LIGO-T060267-00-D document “Upgrading the Input Optics for High Power Operation”.

6.5.1 Mechanical design

The modulator is enclosed in an industry-standard housing, providing multiple apertures to guarantee that the high power laser beam comes in contact only with the crystal and not the electrodes (thus preventing catastrophic damage). The housing will be manufactured by UF. The crystal housing does not include the resonant circuit and impedance matching network.

6.5.2 Impedance matching

The impedance matching circuit is placed in a separate housing to easily change resonant frequencies without the need to access the sensitive crystal. Figure 6.1 shows the equivalent circuit of the impedance matching network. The matching circuit is designed to have an input impedance of 50Ω and at resonance to increase the RF voltage at the crystal by Q , the quality factor of the resonator.

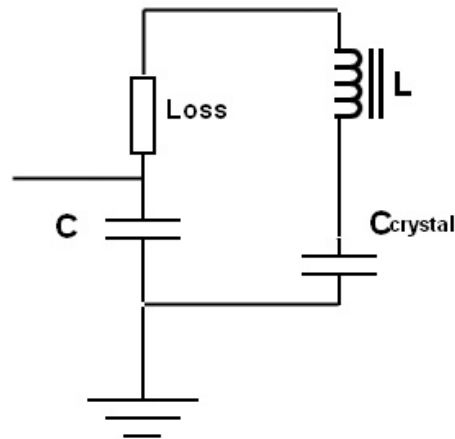


Figure 6.1 Equivalent circuit of the resonant circuit / impedance matching network.

Based on earlier ISC requirements, we have made and tested matching networks for $f = 19.7$ MHz and 180 MHz. The crystal has capacitance $C = 6$ pF and the impedance associated with the electrodes and the electrical wiring is about 2Ω . The shunt capacitance is in the 20 pF range. The 19.7 MHz circuit had $Q = 20$ while the 180 MHz circuit had $Q = 3$.

6.5.3 Temperature stabilization

It is planned to actively stabilize the modulator crystal temperature with a temperature control circuit. The temperature can be measured with standard low voltage temperature sensors like the TMP35/36/37 which has a sensitivity of 10mV/K. The temperature will be stabilized by feeding the error signal to Peltier elements that control the temperature of the modulator housing.

6.5.4 Damage testing and thermal lensing

Results of damage testing and thermal lensing are given in “Upgrading the Input Optics for High Power Operation”, LIGO-T060267-00-D, and “Modulators and Isolators for Advanced LIGO”, LIGO-G060361-00-D.

6.6 Avoiding Sidebands on Sidebands

Currently, three techniques are known to circumvent the sidebands on sidebands problem¹¹ that arises when phase modulators are used in series to impose modulation sidebands. The baseline design is to split the beam using a Mach-Zehnder interferometer and apply the modulations in different arms. We will concentrate on this in the first part of the following section. As an alternate solution to this problem that is also pursued by our group we will briefly discuss the possibility of the use of *complex modulation* to synthesize arbitrary modulation configurations. In addition, it is possible to use two-phase locked lasers to generation a frequency-shifted sub-carrier, however we are not actively exploring this as it falls outside of the IO scope.

6.6.1 Parallel (Mach-Zehnder) modulation

The parallel phase modulation was first tested in an interferometer at Caltech's 40 m prototype.¹² This technique entails splitting the laser light with a beam splitter, modulating the transmitted and reflected beams with two different frequencies, and then recombining the light with a second beamsplitter, as shown in Figure 6.2. This configuration is commonly called a Mach-Zehnder (MZ) interferometer.

Although the MZ method avoids the generation of sidebands on sidebands, it creates some other complications:

- An additional servo loop to control MZ differential arm length
- Overdriving the EOMs to achieve the required modulation index
- Possible introduction of excess intensity, frequency and sideband noises
- Additional intensity modulation (noise) at modulation and mixing (sum/difference) frequencies

As an interferometric method is used to recombine the beams, it is necessary to control the differential length arm to keep the output port constructive for the carrier. It is also necessary to keep both arms equal lengths on a macroscopic scale to achieve a good beam overlap and therefore a good visibility.

¹¹ LIGO-T040119-00-R, "Mach-Zehnder interferometer for Advanced-LIGO optical configurations to eliminate sidebands of sidebands, O. Miyakawa, et al.

¹² LIGO-T040161-00-R, "Effect of Mach Zehnder Residual Displacement Noise on the 40m Detuned RSE Interferometer, S. Kawamura and O. Miyakawa.

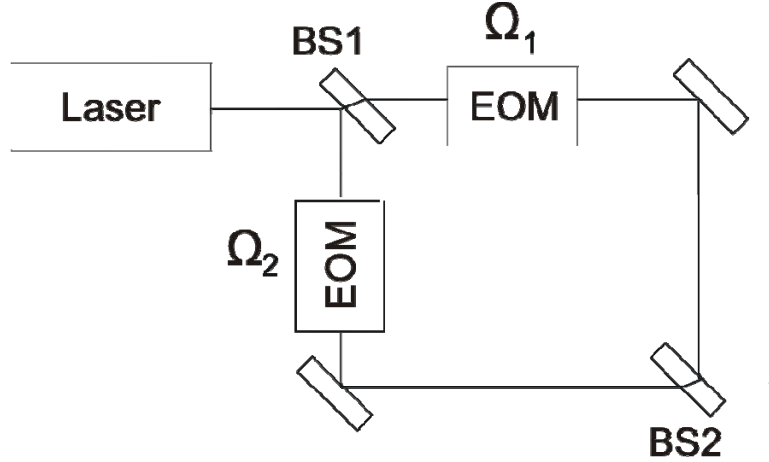


Figure 6.2 Parallel modulation using a Mach-Zehnder interferometer.

Assuming 50/50 beamsplitters for the input and output ports, only half of the light is modulated with each modulation frequency and then half of the modulation is lost at the combining beam splitter, reducing the effective modulation index 4X.¹³ The recombined light is constructed from two physically distinct optical paths, thus environmental noise can lead to additional intensity, phase or pointing (beam position) noise. Finally phase modulation directly couples into intensity modulation at the second harmonic if the interferometer is kept on the bright fringe and might even leak into the fundamental if the length is not perfectly kept on the bright fringe.

6.6.2 Noise coupling / estimates

The recombined light emerging from the MZ interferometer may exhibit noisiness in its amplitude, phase, or pointing. These noise terms will not be common to all frequency components, a situation distinct from noise found in serial modulation. The noise is the result of mirror motions or index of refraction changes that may be either common or differential between the two Mach-Zehnder arms, or even between mirrors within a single arm. The mirror motions, in turn, may be either angular or longitudinal, and non-normal angles of incidence on mirrors or beams not centered on the optics will mix the effects.

The laser field exiting the MZ is given by:

$$\frac{E_0}{2} e^{i\omega t} e^{ik\bar{L}} \left(e^{ik\Delta L} e^{im_1 \sin(\Omega_1 t)} + e^{-ik\Delta L} e^{im_2 \sin(\Omega_2 t)} \right) + c.c. \quad (6.1)$$

Where Ω_1 and Ω_2 are the modulator frequencies, and m_1 and m_2 are the modulation depths of the two EOMs. We also define the common and differential MZ lengths to:

$$\bar{L} = \frac{L_1 + L_2}{2} \quad , \quad \Delta L = \frac{L_1 - L_2}{2} . \quad (6.2)$$

¹³ In the event that one modulation frequency dominates, the BS ratios can be adjusted to allow for increased power in one arm

with the L_i denoting the length of the two MZ arms.

6.6.2.1 Longitudinal common motion

Longitudinal common motion, when \bar{L} causes phase noise (or noise frequency sidebands) common to carrier and radio-frequency sidebands, is the same as noise produced by vibrating serial modulation components. Because this is a familiar variety of noise, we expect to be able to combat it with existing techniques. This is accomplished with laser frequency monitoring and feedback through the mode-cleaner, which in turn is locked to the common mode of the long arm cavities.

6.6.2.2 Longitudinal differential motion

When the lengths of the MZ arms change differentially $\Delta L \rightarrow \Delta L(t)$, two noise effects occur. The amplitude of the recombined carrier varies, and relative phase noise develops between recombined carrier and the sidebands.

6.6.2.2.1 Sideband-carrier relative phase noise

With the current Advanced LIGO design, noise in the relative phase between carrier and sideband light can end up as laser frequency noise. As mentioned, the laser's frequency is locked to the mode cleaner, which in turn is locked to the common-mode of the arm cavities. The arm cavity common-mode error signal S will (most probably) be measured in the beat between carrier and the one of the sidebands. In this scheme, relative phase noise is indistinguishable from laser frequency noise, feeding back a corrective signal that will impose noise on the laser. The limit on laser frequency noise has been established for Advanced LIGO¹⁴, see Figure 6.3.

To translate this into a limit on differential motion of the Mach-Zehnder arms, we compare the transfer functions of sideband-carrier relative phase to the arm cavity common-mode error signal and the frequency noise transfer function. Given a frequency noise limit $\Delta f(f)$, the relative phase noise limit $\Delta\Phi(f)$ is

$$\Delta\Phi(f) = \frac{\partial S / \partial f}{\partial S / \partial \Phi} \Delta f(f).$$

Here S is the arm cavities' common-mode error signal.

We find the relative phase noise transfer function with a FINESSE model of the full Mach-Zehnder-enhanced dual-recycled interferometer. This noise analysis uses the current baseline parameters of the locking scheme and assumes that 9 MHz sideband is used to generate the error signal. The same simulation is used to calculate the transfer function of frequency noise. Combining both transfer functions allows us to estimate the maximum allowed phase and therefore displacement noise in the differential arm length. The result is presented in Figure 6.4.

(Once the locking scheme is finalized this investigation has to be repeated to verify the final requirements for the *Sideband-carrier relative phase noise*.)

¹⁴ P. Fritschel, "Advanced LIGO Systems Design Report No. LIGO-T-010075-00-D", LSC Conference 2001.

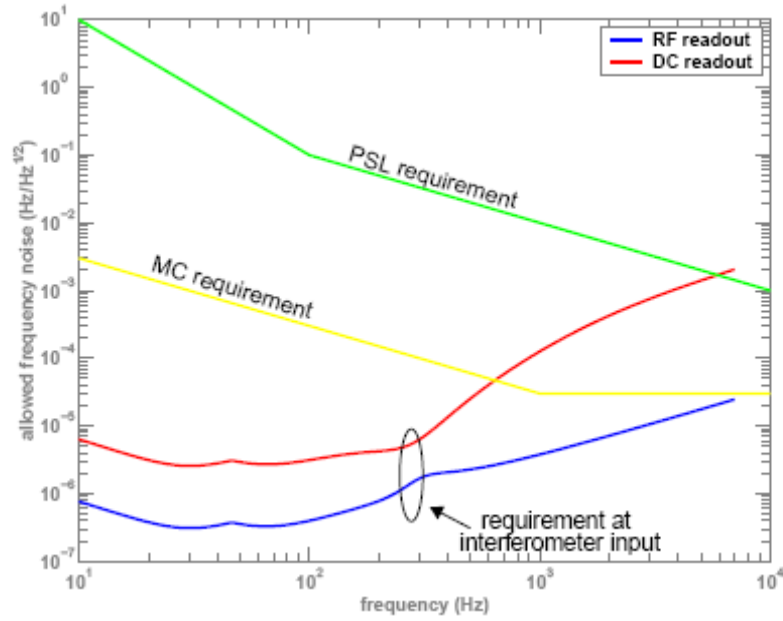


Figure 6.3 AdvLIGO frequency stability requirements

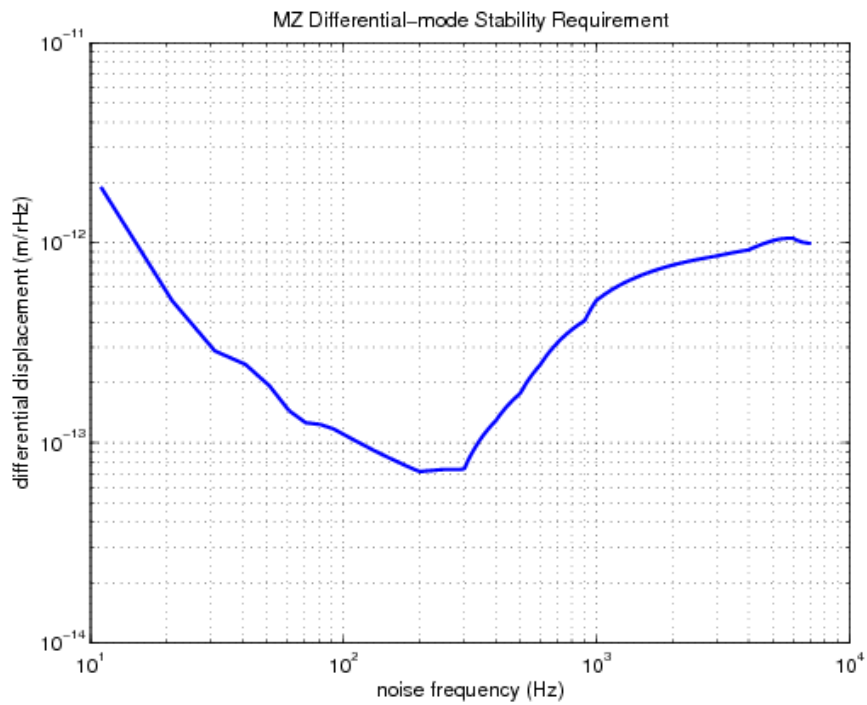


Figure 6.4 Stability requirement for MZ differential mode

6.6.2.2.2 Sideband amplitude noise

The intensity stabilization servo (ISS) after the IMC will make noise in the amplitude of the recombined carrier and the generated sidebands look like noise in the modulation depth.

A limit on Mach-Zehnder differential arm length motion due to sideband amplitude noise is hard to establish but we can quantify the amount of change in the sideband amplitude as a function of the differential length ΔL . The intensity is stabilized to I_0 , meaning the following expression can be assumed to be true for all ΔL .

$$I_0 = \frac{I(\Delta L) \cdot 2}{1 + \cos(2k\Delta L)} . \quad (6.3)$$

Solving this for the intensity before the MZ (assuming small ΔL) gives:

$$I(\Delta L) = \frac{I_0}{2} [1 + \cos(2k\Delta L)] \approx I_0 (1 + (k\Delta L)^2) . \quad (6.4)$$

To first order in $\delta L(f)$ this directly translates into the apparent relative intensity of the carrier and the sidebands to:

$$RIN(f) = k^2 \Delta L_{RMS} \delta L(f) = 4\pi^2 \frac{\Delta L_{RMS}}{\lambda} \frac{\delta L(f)}{\lambda} \quad (6.5)$$

where ΔL_{RMS} is the fringe offset. Assuming a conservative value of $\Delta L_{RMS} = 10$ nm, this leads to a sideband relative intensity noise $RIN_{sb} \approx 3.5 \times 10^{-8}$.

6.6.2.3 Angular mirror motion effects

When mirrors have angular fluctuations, a disparity arises between the optical axes of the Mach-Zehnder IFO and the IMC. Small displacements δ or tilts θ in the recombined beam after the MZ, when expanded in the IMC basis set, will contain small contributions from higher-order Gaussian modes. As the magnitude of the δ or θ mode changes is determined by the differential displacement noise the changes of δ or θ are in the $10^{-13} \frac{\text{m}}{\sqrt{\text{Hz}}}$ or $10^{-13} \frac{\text{rad}}{\sqrt{\text{Hz}}}$ regime (assuming ~ 1 m long arms) and thus fairly small compared to the waist of the beam and thus the *extra intensity noise* after the IMC will be easily suppressed.

6.6.3 Experimental realization

To investigate the noise properties and potential problems of the parallel modulation scheme, a table-top prototype compact and quasi monolithic Mach-Zehnder interferometer was built. All optics were mounted using small mirror mounts near the plate avoiding long lever arms and hereby reducing potential low frequency resonances. Figure 6.5 shows the schematic realization of the experiment. To allow differential arm length control with a high dynamic range, a small 10.0 mm diameter, 2.0 mm thick HR mirror is attached to a PZT actuator which allows tuning the differential arm length with only 2 V per wavelength. The small mirror creates a resonance of about 13 kHz with the PZT. No high voltage amplifiers are needed to compensate for thermal drifts and

the PZT as well as the EOM are driven directly from a low-noise op amp. The servo description can be found at the end of this section.

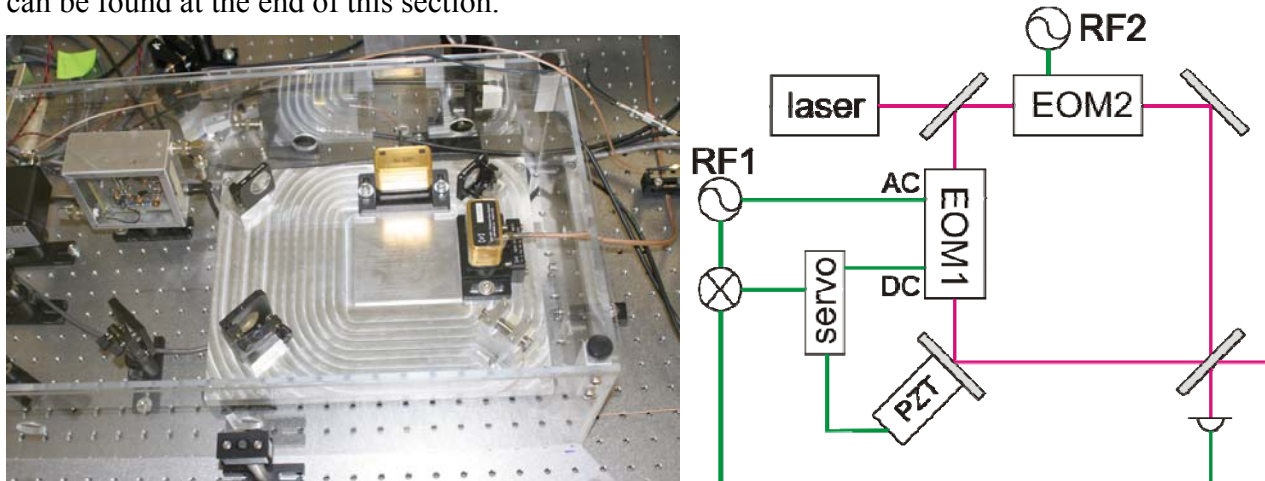


Figure 6.5 Experimental MZ layout. Photo (left) and schematic drawing (right).

The EOM2 shown in Figure 6.5 was an off-shelf resonant phase modulator from New Focus while EOM1 was based on an AdvLIGO design (albeit using a LiNbO₃ crystal) using a modified external resonant / impedance matching circuit that permitted a feedback path for frequency actuation signals. The circuit is shown in Figure 6.6.

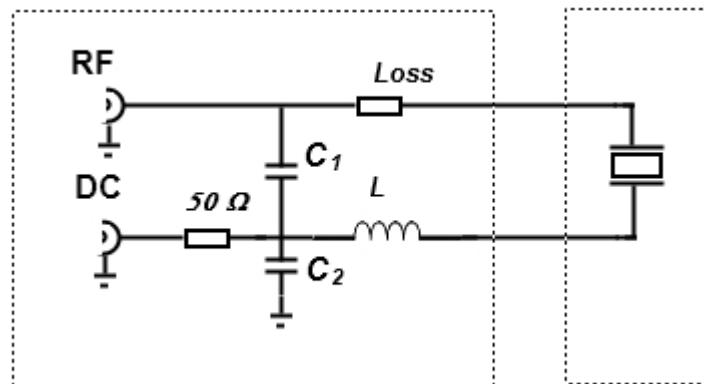


Figure 6.6 Modified impedance matching circuit with DC input and EOM in separate housings.

These modifications allowed us to use the EOM to apply the phase modulation sideband and simultaneously to use it for fast phase (optical path length) correction of the differential arm length. In this prototype, EOM1 was made resonant for 25 MHz and EOM2 was resonant for 31.5 MHz. The 31.5 MHz frequency was used in an internal modulation scheme to generate the error signals for the differential mode.

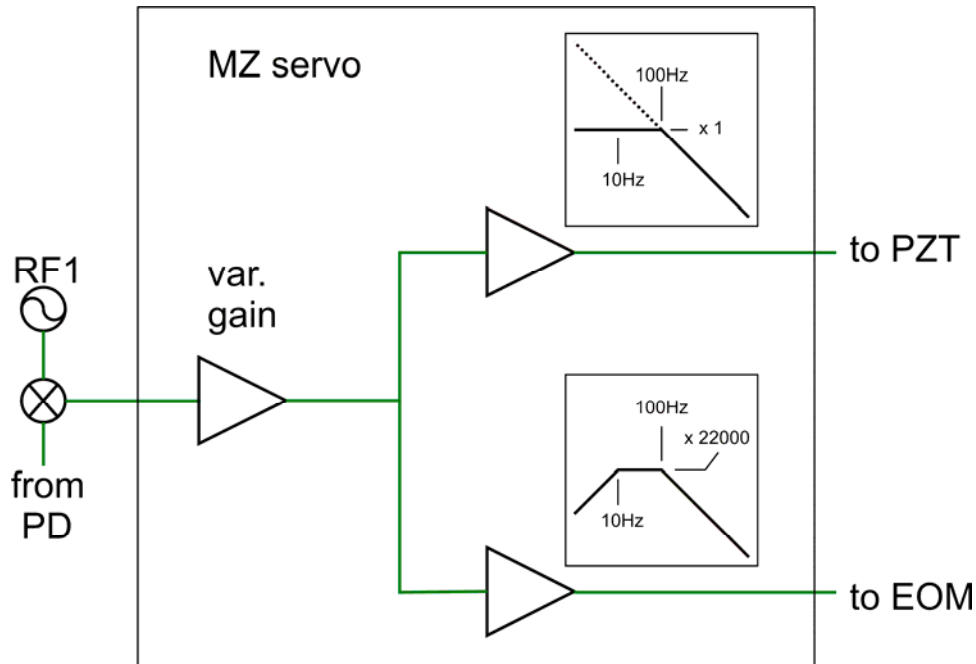


Figure 6.7 Schematic servo design with slow and fast actuator output.

The servo, which is schematically shown in Figure 6.7 above, splits the control signals in “fast” and “slow” components and feeds the slow (but with a high dynamic range for drift control) part back to the PZT and the fast part to the DC input of the EOM. The PZT has a half-wave voltage $V_{\pi} = 1.04$ V, the EOM shows a $V_{\pi} = 210$ V and therefore the electrical gain in the EOM part of the servo has to be significantly higher than in the PZT part. Even though the electronic gain is 22000 times bigger at 100 Hz the noise suppression is only 100 times bigger for the EOM as shown in the following measurement. Figure 6.8 shows the achieved unity gain bandwidth of 40 kHz with about 30 dB noise suppression at 1 kHz when using the combined PZT and EOM servo loop. The remaining servo-bump at 100 kHz will be removed in future versions of the servo design.

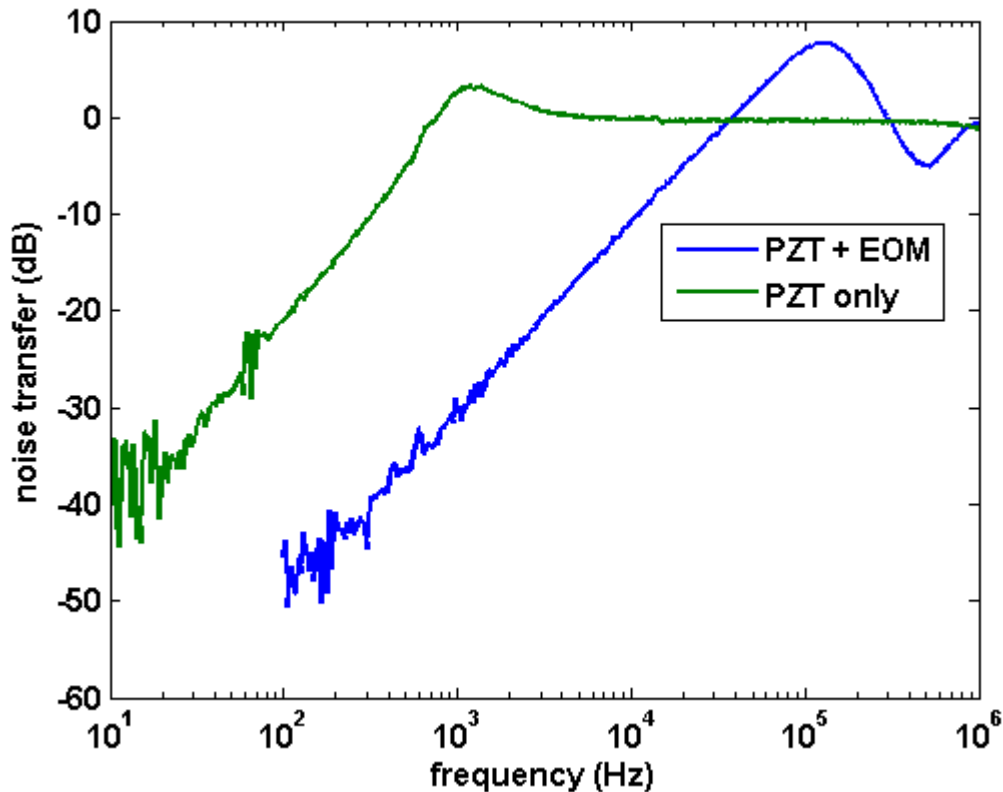


Figure 6.8 Closed-loop noise suppression TF

The complete setup was covered by a Plexiglas enclosure to limit the influence of the environment and the error point noise was used to determine the remaining differential length noise to be less than $10^{-13} \frac{\text{m}}{\sqrt{\text{Hz}}}$, currently limited by the Spectrum Analyzer input noise. Measurements to measure the differential length noise with an independent mixer in an out-of-loop fashion are currently in preparation.

6.6.4 Power scaling

The current set up is not yet ready to handle 180 W of input light but very few changes have to be made to adapt it to this power level. First the EOMs have to be replaced with the final design using RTP crystals instead of MgO:LiNbO₃ crystals and secondly the beamsplitters as the only transmissive optics have to be replaced with superior low absorption fused-silica substrates.

6.6.5 Monolithic design (alternative design #1)

A future option to counter long-term drift which increases the requirements on the dynamic range of the actuators and to increase the stability significantly is to use a monolithic design made from ultra low expansion glass.

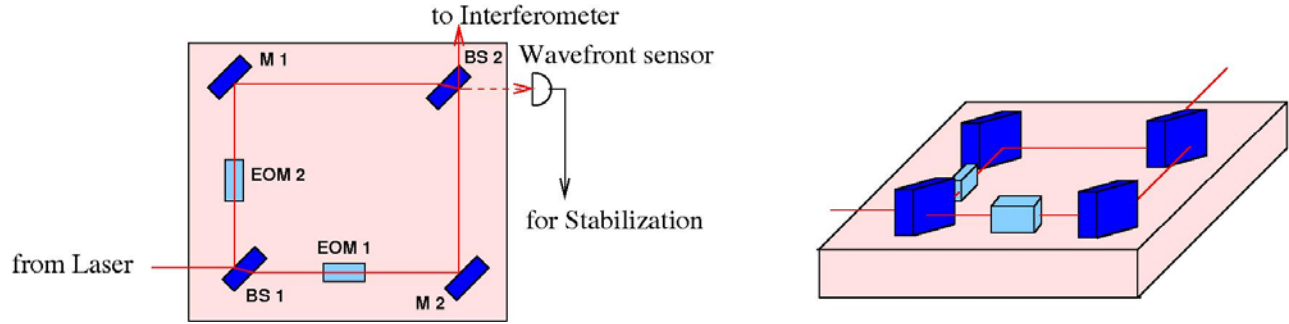


Figure 6.9 Monolithic realization of MZ

We plan to prototype a monolithic Mach-Zehnder interferometer for the final design phase using a Zerodur or ULE baseplate and either optically contact or hydroxide bond the mirrors and beam splitters. Another aspect is to study potential actuators which will later be incorporated into the interferometer to control the longitudinal and angular degrees of freedom such as thermally controlled actuators operating on the optical length and RTP prisms to control angular deviations.

6.6.6 Complex modulation (alternative design #2)

An alternative approach has been developed in which phase and amplitude modulation are simultaneously applied to generate sidebands without mixing terms. Termed complex modulation, we briefly discuss the underlying principle:

An amplitude- and phase modulated light field in general can be described as:

$$E(t) = \frac{E_0}{2} \exp(i\omega t + f(t)) + c.c. \quad (6.6)$$

where the modulation function can be divided in

$$f(t) = \phi(t) + i\alpha(t) \quad (6.7)$$

To create an arbitrarily chosen field E_{new} the following equation has to be solved:

$$E_{new}(t) = E_{old}(t) \cdot \exp(f(t)) + c.c. \quad (6.8)$$

leading to the following coefficient for the amplitude and phase modulations:

$$\alpha(t) = \ln \left| \frac{E_{new}(t)}{E_{old}(t)} \right| \quad \phi(t) = \arg \left(\frac{E_{new}(t)}{E_{old}(t)} \right) \quad (6.9)$$

To follow this approach and to investigate complex modulation it is necessary to impose arbitrary phase and amplitude modulations on the carrier laser light.

6.6.6.1 Experimental realization

A proof-of-principle experiment has been set-up to investigate the usability of this approach. Figure 6.10 shows the schematic setup. The amplitude modulation was generated with an EOM between 45° polarizers. The unwanted extraneous phase modulation was compensated with the second EOM that is mounted in the standard phase modulation orientation.

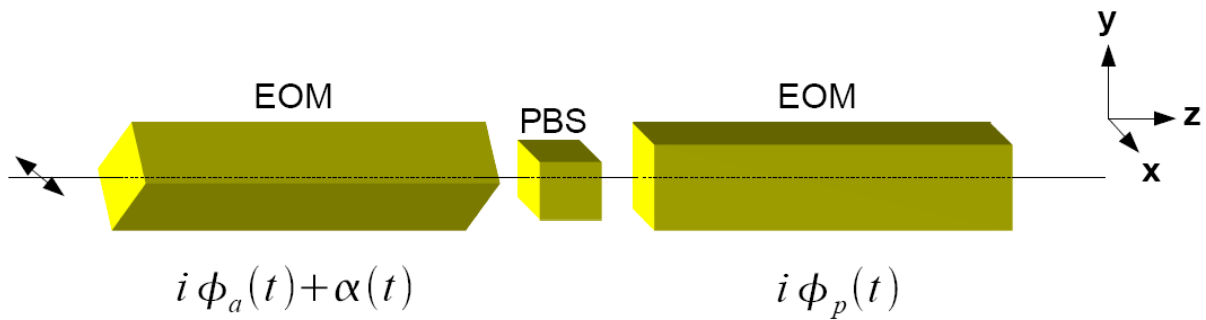


Figure 6.10 Complex modulation

In this configuration, the modulation function can be written as:

$$f(t) = \phi_a(t) + \phi_p(t) + i\alpha(t)$$

Figure 4.3Figure 6.11 shows the schematic layout of the experiment. The modulation function was calculated by a PC running Matlab that was equipped to upload the modulation function into a Tektronix AFG3252 arbitrary function generator.

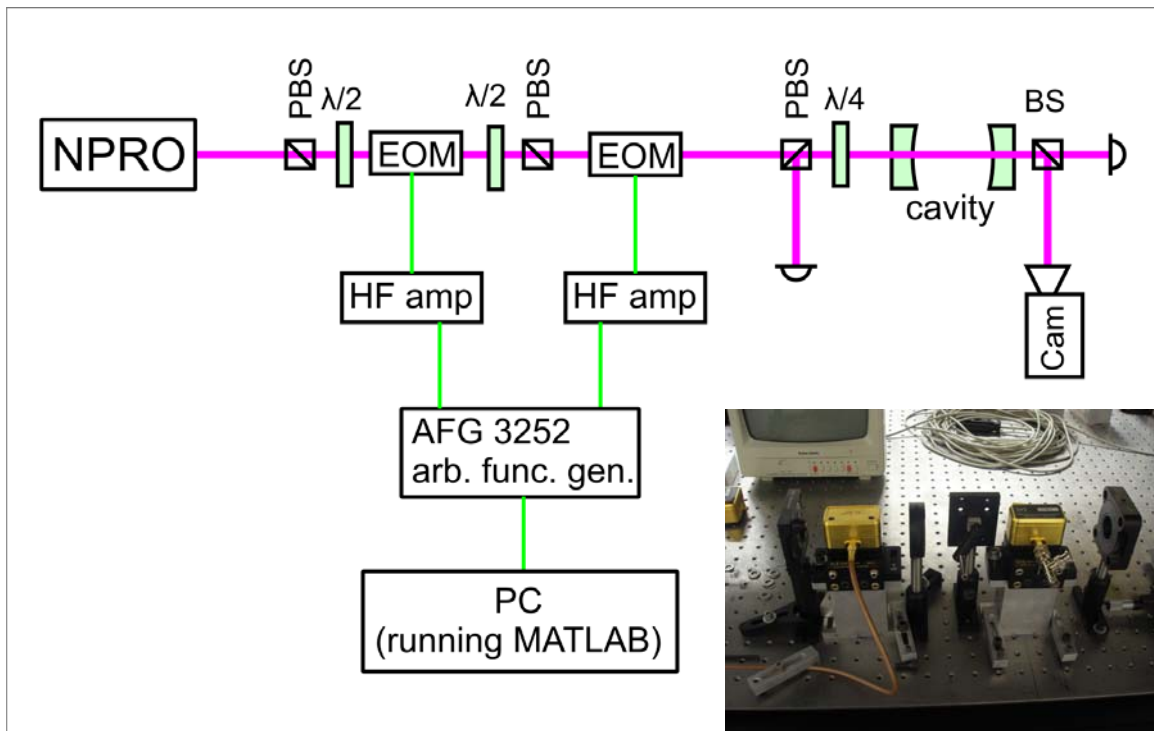


Figure 6.11 Schematic experimental setup. Inset in lower right corner shows the two EOMs.

To achieve a modulation depth of $m = 0.7$ the signals of the function generator were amplified by two RF amplifiers and fed into the modulators. We used an optical cavity to analyze the frequency components and a fast photodiode to measure the amplitude modulation.

To synthesize the desired modulation the transfer function of the modulators has to be flat, or at least to be stable so that it can be compensated by the calculated modulation function. During the measurements, we uncovered the following issues:

- Temperature-dependent AM
- Non flat transfer function probably caused by electrical and/or piezo resonances in the driver and the crystal prohibiting the compensation of mixing terms.
- The (currently used) HF amplifiers become nonlinear for large driving signals.

These problems are likely to be overcome by temperature stabilization of the crystal, the use of electronic and/or mechanical damping and superior amplifiers. Despite these problems the preliminary setup is already able to create and measure a single sideband modulation on the carrier.

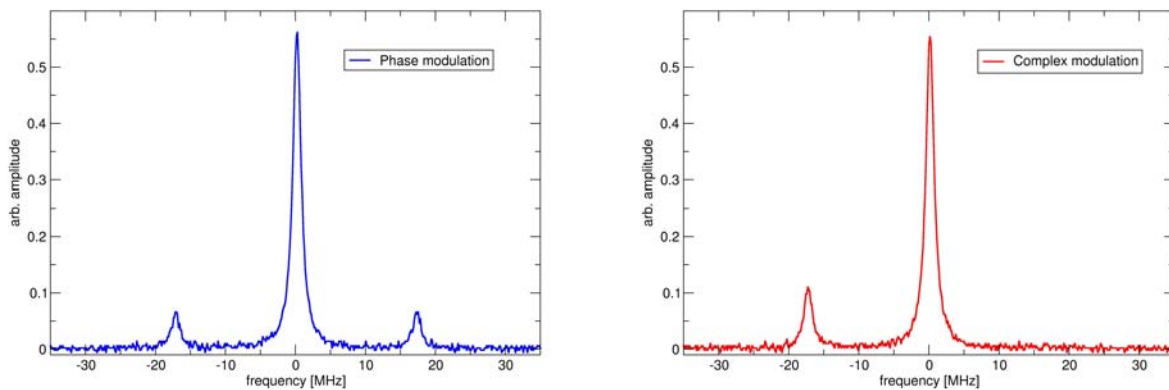


Figure 6.12 Left: Phase Modulation. Right: Single sideband from complex modulation.

7 Input Mode Cleaner

The laser light must be frequency and spatially stabilized before it can be used in the interferometer. The input mode cleaner provides active frequency stabilization through feedback to the PSL, passive frequency noise suppression above its cavity pole frequency, and passive spatial stabilization at all frequencies. The input mode cleaner also reduces higher order modal content of the laser light, suppressing beam jitter.

7.1 Optical Configuration and Definitions

The input mode cleaner is a Fabry-Perot cavity with a moderately high finesse. Its shape is that of a narrow isosceles triangle, as shown in Figure 7.1. The triangle configuration is preferred for several reasons, notably the improved optical isolation it provides. The cavity configuration is flat-flat-curved. The two flat mirrors (MC1 and MC3) define the base and act as the input and output couplers. These are located in HAM2. The curved mirror (MC2) is in HAM3. All three mirrors are suspended.

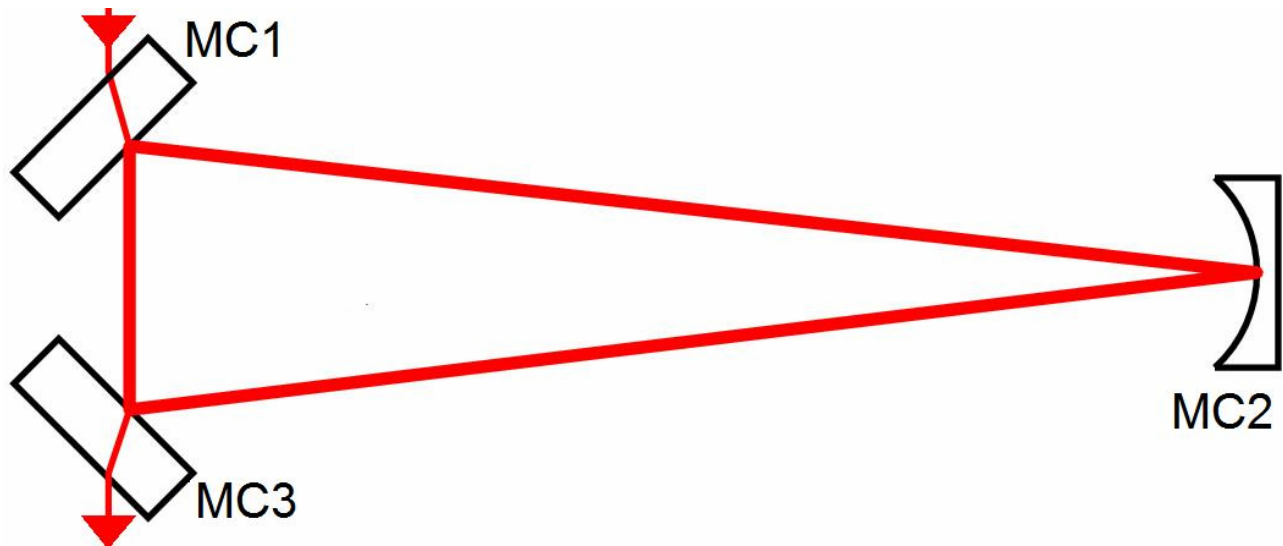


Figure 7.1 Diagram of the input mode cleaner, defining the names of the mirrors.

A Fabry-Perot cavity has transmission

$$t = \frac{t_1 t_2 e^{i\delta}}{1 - r_1 r_2 e^{2i\delta}} \quad (7.1)$$

where t_1 is the amplitude transmissivity and r_1 the amplitude reflectivity of the input mirror; t_2 is the amplitude transmissivity and r_2 the amplitude reflectivity of the output mirror; δ is the optical phase associated with the cavity length L ; for plane waves and plane-parallel mirrors,

$$\delta = \omega L/c \quad (7.2)$$

where ω is the frequency of the light. Here, the optical round-trip path is $2L$. The resonator has transmission maxima whenever $\delta = n\pi$, with n an integer.

The input mode cleaner is located in vacuum. The separation between the chambers determines the range of lengths (and thus of the free spectral range) of the input mode cleaner. The input mode cleaner mirrors are suspended in Mode Cleaner Triple Suspensions.

The specific functions of the input mode cleaner are discussed in the following paragraphs.

7.2 Input Mode Cleaner Optical Parameters

7.2.1 Constraints and Assumptions

The input mode cleaner (MC), power recycling cavity (PRC), signal recycling cavity (SRC), and arm cavity lengths are all interrelated. The arm cavity length determines the PRC/SRC and MC cavity lengths. Moreover, the arm cavities have only +/- 30 mm adjustability. The requirement is that the input mode cleaner and power-recycling cavity resonate the carrier and both locking sidebands but that the arms resonate only the carrier. The sideband is to be 5-6 Hz away from being maximally antiresonant in the arms.

7.2.2 Lengths

The sideband frequencies must satisfy

$$f_{prc} = (k + 1/2)c/2L_{prc} \quad (7.3)$$

where ($k = 0,1,2 \dots$) and L_{prc} is the power recycling cavity length. (Here the length is measured from the PRM to the average of the two ITMs.) The factor of 1/2 occurs because the carrier is resonant in the arm cavities whereas the sidebands are not resonant in the arms, giving an extra 180 degree phase shift in the reflectivity of the arms.

Both sidebands must be equal to one of the input mode cleaner resonances, because the RF modulation is imposed before the input mode cleaner. The resonant frequencies of the input mode cleaner are:

$$f_{imc} = nc / 2L_{imc} \quad (7.4)$$

where n is an integer (1,2,3 ...) and L_{imc} the input mode cleaner length.

The signal recycling cavity length is also tied to these frequencies; its length is¹⁵

$$L_{src} = (p + \delta_\phi/2\pi)c/2f_{src} \quad (7.5)$$

where p is an integer (1,2,3 ...), δ_ϕ is the signal recycling detuning (0.1 rad), and f_{src} is the frequency used to sense the position of the SRM.

¹⁵ "Optical Layout for Advanced LIGO," D. Coyne, LIGO-T010076-010D (7/1/2001)

There is a modest range of adjustments available for L_{prc} and L_{imc} , determined by the dimensions of the LIGO vacuum envelope, the size of the optical tables, and considerations of other articles that must reside on these tables.¹⁶ In turn, this determines a range of frequencies for both f_{prc} and f_{imc} . The union of these frequencies is available for the controls of the interferometer. The lengths are summarized in Table 5 (all dimension in m):

Table 5 Allowed range of lengths for LIGO cavities

Cavity	Configuration	Min	Max
MC	All	15.910	16.461*
PRC	Straight, marginal	8.142	9.162
PRC	Straight, stable	55.480	59.255
SRC	Straight	8.606	9.626
AC	Straight	3994.455	3995.033
PRC	Folded, marginal	13.317	14.338
PRC	Folded, stable	60.602	64.495
SRC	Folded	13.321	14.238
AC	Folded	3994.206	3994.721

* The actual max is 0.6 m longer; this space is reserved for input injection optics. Using it for a longer mode cleaner would not affect any of the length issues (such as no 9 MHz frequency for the folded PRC) discussed below.

7.2.3 Modulation frequencies

The procedure we have used for fixing the modulation frequencies then begins by setting the arm cavity lengths. The length of the arm cavity for the straight (non-folded) interferometer is recommended to be 3994.750 m. The length for the folded interferometer is recommended to be 3994.450 m. Given these lengths, one can find a discrete set of frequencies spaced by 37.5 kHz that satisfy equations (7.3) and (7.4) and the nearly antiresonant condition for the sidebands with respect to the arm cavities. Finally, we can set the length of the SRC from equation (7.5).

The power recycling cavity length is of course quite different depending on whether marginal or stable configurations are chosen, and also differs between the straight (H1/L1) and folded (H2) interferometers.

We highlight one issue at this point: *Given the present location of the HAM chambers, there is no solution lower than 27.3 MHz for the folded interferometer with marginal PRC.* For the stable PRC, the lowest frequency is 17.6 MHz. The minimum frequencies could be reduced to 16.4 MHz (marginal) and 8.4 MHz (stable) by adding 1.8 m to the HAM2/HAM3 separation.

The cases are discussed in the following sections.

¹⁶ “Constraints of Advanced LIGO Cavity Lengths, Version 2” by Luke Williams, LIGO T-###

7.2.4 Straight IFO, Marginal PRC

The length ranges for the MC are 16.284-16.461 m. The length ranges for the PRC are 8.142-8.321 m. (This is the range for each where solutions exist.) A set of lengths (and corresponding frequencies) that meet the requirements is:

Table 6. Straight IFO, Marginal PRC

AC Length	m	3994.750
IMC Length	m	16.338
PRC Length	m	8.169
First frequency	MHz	9.1744
Second frequency	MHz	45.8722
SRC Length	m	9.855*
Alternative second frequency	MHz	64.2211
Alternative SRC length	m	9.373
High second frequency	MHz	183.4890
SRC length for high frequency	m	8.999

*This length is 229 mm *longer* than allowed by physical constraints in the SRC HAM.

One could use MC and PRC lengths of 16.406 m and 8.203 m respectively also; this is the only other possibility if the low modulation frequency is to be near 9 MHz.

7.2.5 Straight IFO, Stable PRC

The length ranges for the MC are 15.910-16.461 m. The length ranges for the PRC are 55.685-57.614 m. A set of lengths (and corresponding frequencies) that meet the requirements are”

Table 7. Straight IFO, Stable PRC

AC Length	m	3994.750
IMC Length	m	15.947
PRC Length	m	55.815
First frequency	MHz	9.3996
Second frequency	MHz	46.9979
SRC Length	m	9.619
Alternative second frequency	MHz	65.7971
Alternative SRC length	m	9.149
High second frequency	MHz	175.5922
SRC length for high frequency	m	9.246

7.2.6 Folded IFO, Marginal PRC

The length ranges for the MC are 15.980-16.461 m. The length ranges for the PRC are 13.317-13.718 m. A set of lengths (and corresponding frequencies) that meet the requirements are:

Table 8. Folded IFO, Marginal PRC

AC Length	m	3994.450
IMC Length	m	16.139
PRC Length	m	13.449
First frequency	MHz	27.8631
Second frequency	MHz	65.0140*
SRC Length	m	13.870
High second frequency	MHz	185.754
SRC length for high frequency	m	13.731

* 46.4386 MHz leads to a SRC length of 12.936 m, 255 mm too short.

The PRC is longer for the folded interferometer, putting its first resonance at 5.2-5.6 MHz and its second resonance near 15.7-16.9 MHz. Neither frequency is consistent with the 9.26 MHz median input mode cleaner FSR; the first hit occurs for $n = 3$ and $k = 2$ in equations (7.3) and (7.4) above.

If the tube that links HAM2 and HAM 3 were increased in length by 1.8 m, then the input mode cleaner FSR is decreased to 8.33 MHz, and a frequency of 16.65 MHz could be used. (Note that this tube is scheduled for replacement in Advanced LIGO.)

7.2.7 Folded IFO, Stable PRC

The length ranges for the MC are 16.160-17.061 m. The length ranges for the PRC are 60.602-63.979 m. A set of lengths (and corresponding frequencies) that meet the requirements are:

Table 9. Folded IFO, Stable PRC

AC Length	m	3994.450
IMC Length	m	16.221
PRC Length	m	60.829
First frequency	MHz	18.4816
Second frequency	MHz	64.6857
SRC Length	m	13.941
High second frequency	MHz	175.575
SRC length for high frequency	m	8.551

If the tube joining HAM2 and HAM3 were increased in length by 1.8 m, a low frequency between 8.31 and 8.46 MHz could be employed.

7.2.8 Calculated Optical Parameters

The following sections list the optical parameters chosen for the input mode cleaner. To save space, the results are presented only for the straight interferometer, marginal PRC case. Gaussian parameters change a few % for the other cases.

Table 10 Optical parameters for the straight interferometer, marginal PRC

IMC Length	m	16.338
IMC free spectral range	Hz	9,174,449
IMC polarization		's'
MC1/3 radius of curvature	m	>10000
MC1/3 transmittance		0.006
MC1/3 reflectance		0.994
MC2 radius of curvature (cold)	m	26.769
MC2 transmittance		<0.00001
MC2 reflectance		0.9999
Mirror absorption/scatter loss (each)	ppm	30
IMC finesse		519
Cavity Pole Frequency	Hz	8,830
Cavity g factor		0.3897
MC waist	mm	2.103
Rayleigh range	m	13.05
Input Power	W	165
Stored IMC Power	kW	23.2
Intensity at Flat mirrors	kW/cm ²	167
IMC mirror mass	kg	2.92
IMC mirror diameter	cm	15
IMC mirror thickness	cm	7.5
MC1,3 HR center-center distance	cm	43.18
MC1,3 intracavity angle of incidence, θ	deg	44.625
Static radiation pressure (MC1/MC3)	Pa	7.9
Static radiation pressure (MC2)	Pa	4.3

Static force from radiation pressure (MC2)	μN	155
--	---------------	-----

7.2.9 Input Mode Cleaner Locking Frequency

The modulation frequency to be used to lock the mode cleaner is not transmitted (heavily attenuated by the MC) and can be considered non-critical as long as overlap with the modulation frequencies for the core interferometer is avoided. We choose a value of **32.011 MHz (TBR IO)**, for the IMC locking, about 100 kHz off the fourth antiresonance ($n = 3.5$).

7.3 Input Mode Cleaner Expected Performance

7.3.1.1 Transmission

Figure 7.2 shows the calculated mode cleaner transmission as a function of frequency for one FSR above the carrier.

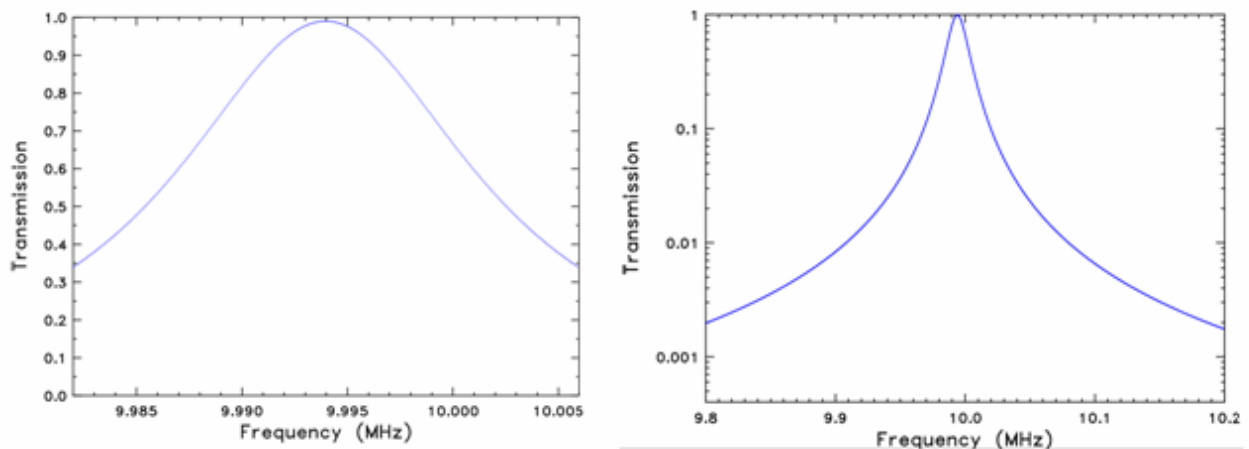


Figure 7.2 Calculated input mode cleaner transmission as a function of frequency, one FSR above the carrier. The left panel shows the spectrum on a broad frequency scale and a logarithmic scale for the transmission; the left panel shows the detail.

7.3.2 Jitter Suppression

For Advanced LIGO, the beam jitter required at the input to the core optics is such that the relative amplitude of the TEM_{10} mode is $4 \times 10^9 / \text{Hz}^{1/2}$ at 230 Hz and above, rising as $1/f^2$ below 230 Hz. The pointing from the PSL is expected to be $1 \times 10^6 / \text{Hz}^{1/2}$. The input mode cleaner therefore must provide a filtering of a factor of 250.

Beam wobble (angular and lateral deviations of the beam) may be viewed as the superposition of higher-order Gaussian modes on the TEM_{00} mode. Because higher-order modes are suppressed by the input mode cleaner, beam wobble is also suppressed. The amplitude of the suppression is

$$S_{lm} = \frac{1}{\left[1 + \left\{\frac{2F}{\pi} \sin[(l+m)\text{acos}(\sqrt{g})]\right\}^2\right]^{\frac{1}{2}}}$$

where F is the finesse of the cavity. Since, as already discussed, the quantity $(l+m)\text{acos}(\sqrt{g})$ is chosen *not* integer times π , the value of the sinusoid is not zero. If we take it to be a typical value, 1 rad, then, since $F \gg 1$,

$$S_{lm} \approx \frac{\pi}{2F \sin(1)}$$

A finesse of 500 will meet the jitter requirements.

7.3.3 Higher Order Mode Rejection

For TEM_{lm} Gaussian modes, the input mode cleaner Fabry-Perot resonances occur at frequencies

$$\nu_{lm} = \frac{c}{2L} \left[n - \frac{1}{2} + \frac{l+m+1}{\pi} \text{acos}(\sqrt{g}) \right]$$

where $g = 1-L/R$ with R the radius of curvature of the curved mirror. The resonator is adjusted for resonance with the TEM₀₀ mode; this sets the value of n (of order 30 million). The cavity length and mirror radius of curvature (and hence g) are chosen so that the resonance condition can be satisfied for some n and $l=m=0$ not satisfied any other $\{n,l,m\}$. This condition is met when

$$\frac{l+m}{\pi} \text{acos} \sqrt{g} \neq \text{integer} + \varepsilon$$

where ε specifies the amount the higher-order mode avoids being resonant. It is assumed that the actual frequency from the laser of the fundamental and all higher-order modes is the same.

Figure 7.3 shows the transmittance of the mode cleaner (in ppm) vs. mirror radius of curvature. The mode cleaner was taken to be illuminated with light in which all the modes with the fundamental and higher modes satisfying $0 < l+m < 65$ existed with amplitude $\sim 1/\text{sqrt}(l+m)$. The transmittance of the fundamental is unity. As the radius of curvature is varied, one or another of the higher order modes is transmitted. There is a large peak of 14% at $r = 26.73$, when the modes with $l+m = 7$ are transmitted, and then a broad decrease at higher radius, followed by many narrow peaks for larger values of $l+m$. Because the radius of curvature changes by 0.13 m (see below) between cold and hot cases, we pick the cold ROC at $r = 26.769$ m anticipating an increase to 26.9 m when hot.

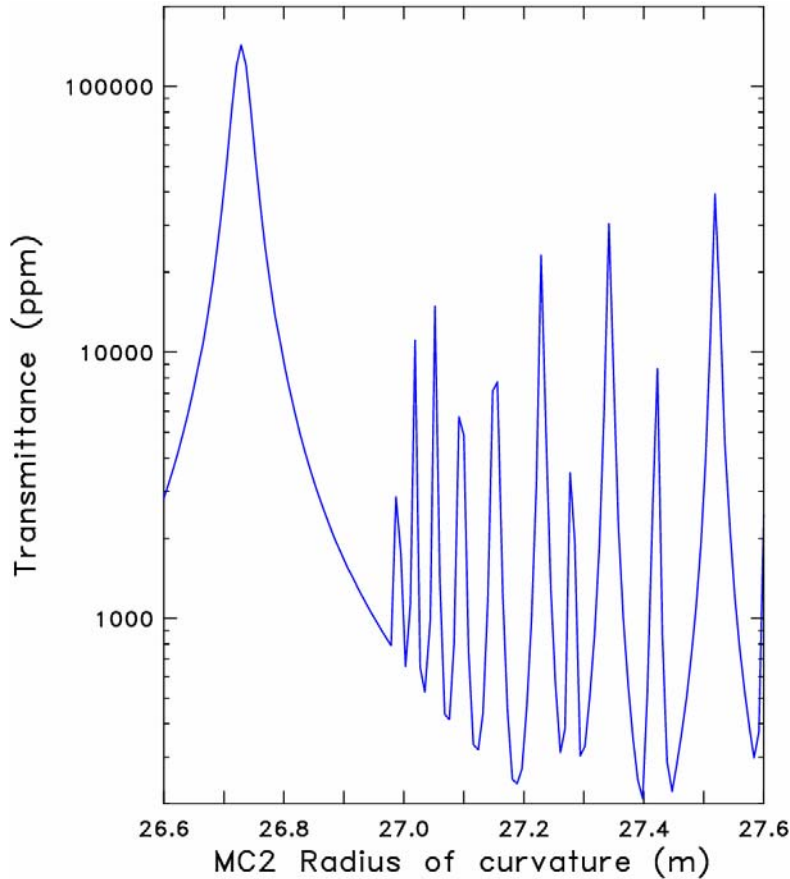


Figure 7.3 Transmission of MC Cavity

7.3.4 Laser wavelength stabilization

The input mode cleaner can serve as a length standard for the laser. The arms are better standards, but the input mode cleaner plays an intermediate role in the length control system.

7.3.5 Laser noise suppression

The input mode cleaner acts as a low-pass filter, with a corner frequency of $f_c = 1/\tau$, where $\tau = 2FL/c$ is the storage time of light in the cavity. Amplitude and frequency noise at frequencies above the corner frequency are suppressed as $1/f$ (20 db/decade).

7.3.6 Polarization

The input mode cleaner transmission is polarized. Because the light in the input mode cleaner has an odd number of reflections during one round-trip circuit, the overall phase of s-polarized light (E normal to plane of the cavity) is reversed on one circuit. This effect shifts the resonance condition from the usual $\nu = cn/2L$ to

$$v = \frac{c}{2L} \left(n - \frac{1}{2} \right)$$

The phase reversal does not happen for p-polarized (E in the plane) light, for which $v = cn/2L$. Thus, the input mode cleaner acts as polarization sensitive filter. As its length is varied, first one and then the other polarization are transmitted.

The input mode cleaner uses s-polarized light.

7.3.7 Input Mode Cleaner Instabilities

7.3.7.1 Optical Spring Effect

The static radiation pressure force in the IMC when on resonance (see above) is 155 μN . If the length of the IMC is changed, this force drops; this change of force with length resembles a spring.¹⁷ The spring is unusual, in that its spring constant is itself linear in the distance from the cavity resonance. The “spring constant” k_{opt} can be calculated: $k_{opt} = dF_{RP}(x)/dx$, where $F_{RP}(x)$ is the radiation pressure force in the cavity, and follows the usual Fabry-Perot resonance form. In the IMC, this resonance (for fixed laser wavelength) occurs over 1.2 nm (FWHM), and the corresponding optical spring would have maximum spring constant (near the $3/4$ maximum points) of $\pm 130,000$ N/m. This is enormously larger than the 170 N/m restoring force of the pendulum suspension. Fortunately, the mode cleaner servo keeps the mirror much closer than 1.2 nm to the resonance; if the deviations are ± 1 pm, the optical spring constant will be below 160 N/m comparable (but not negligible) to the gravitational spring. Thus optical spring effects could change the pendulum resonances by 40%.

7.3.7.2 Angular (Sidles-Sigg) Instabilities

These instabilities¹⁸ work as follows: angular misalignment of the beam in the cavity (decentering) introduces a torque on the suspended mirrors. If fluctuations in this radiation induced torque become larger than the restoring torque of the torsion pendulum, then the resonator becomes

¹⁷ V. B. Braginsky, M. L. Gorodetsky, and F. Ya. Khalili, Phys. Lett. A **232**, 340 (1997);

Benjamin S. Sheard, Malcolm B. Gray, Conor M. Mow-Lowry, David E. McClelland and Stanley E. Whitcomb, “Observation and characterization of an optical spring,” Phys. Rev. A **69**, 051801(R) (2004); A. Di Virgilio, et al. “Experimental evidence for an optical spring.” Phys. Rev. A **74**, 013813 (2006).

¹⁸ John A Sidles and Daniel Sigg, “Optical torques in suspended Fabry Perot interferometers.” Physics Letters A **354**, 167-172 (2006); Daniel Sigg, “Angular Instabilities in High Power Fabry-Perot Cavities,” LIGO-T030120-00; Daniel Sigg, “Angular Stability in a Triangular Fabry-Perot Cavity,” LIGO-T030275-00.

unstable. Following the analysis in LIGO-T030275 we calculate the critical power $P_{crit} = \Theta c \omega^2 / 2k_2 L$ (where Θ is the suspension angular moment, ω is the pitch angular frequency, $k_2 = 0.39$ is a g -dependent eigenvalue of the equations of motion, and L is the cavity length) for the IMC. We obtain $P_{crit} = 2.0$ MW, compared to the 23 KW circulating power in the advanced LIGO IMC design. The mode cleaner will not suffer from this instability.

7.3.7.3 Parametric Instabilities

The IMC is also free of these instabilities, on account of the small spot sizes and large free spectral ranges.

7.3.8 Input Mode Cleaner Thermal effects

Circulating power

The stored power in the input mode cleaner is larger than the incident power by $1/T$, with T the (power) transmittance of the input and output couplers.

Absorption in coatings and the substrates of the input mode cleaner mirrors will lead to changes in the effective radii of curvatures, changing and distorting the spatial eigenmode of the input mode cleaner. The heating in the coating will change the sagitta δs across the beam profile of the input mode cleaner mirrors. This change can be approximated by the Hello-Vinet theory and the details are presented in the supporting document LIGO T070090-00-D.

Based on an absorption coefficient of 0.5 ppm for the coatings and 10 ppm/cm substrate absorption, the fused silica mirror will change their sagitta by $\delta s = 0.523$ nm for the MC₁ and MC₃ mirrors and a beam waist of 2.1028 mm. This would change the radii of curvatures of the flat mirror to -4 km. The radius of curvature of the curved mirror would change from 26.769 to 26.840 m due to a sagitta of 0.62 nm for a 3.4 mm beam size. (See Table 11 Temperature effects in the IMC). However, an effective radius of curvature at MC₂ that incorporates the change of -4 km at MC₁ and MC₃ and the 10 km change at MC₂ can be modeled as if the hot ROC of curved mirror is 26.9116 m. This is the number that can be used to find out hot beam waist and the g -factor of the cavity.

The substrate of MC₁ and MC₃ will act as a thermal lens for the input and output beams. Using the Hello-Vinet theory and the absorption losses mentioned above, a thermal lens of 135 nm is expected. This corresponds to a sagitta of 15.5 nm. This lens is astigmatic in nature because of the 45° angle of incidence at the flat mirrors. The value of 135 nm corresponds to sagittal plane. The thermal lens in the tangential plane is smaller by a factor of 2 because the beam waist in the tangential plane is larger by a factor of $\sqrt{2}$. Therefore a lens of 270 m is expected in the tangential plane. However, for the worst case scenario, if we consider an equal thermal lens of 135 m in both directions, the resultant mode miss-match is less than 0.4% as the interferometer goes from cold to hot state. This thermal lensing if left unchecked will not decrease the power in the TEM₀₀ mode appreciably.

The thermal lensing in the MC mirror will actually be used to improve the mode matching. This will be done by ensuring that the residual thermal lensing in the FI stays negative. Then the positive lens in the MC mirror will cancel the effect of residual thermal lensing in FI to a certain extent. A RH is being planned around DKDP crystal that will further ensure that the beam parameters as seen

by the mode stay same from cold to hot operation. Further details of the scheme will be discussed in Section 8.

With 26 kW stored in the cavity, and 50 ppm losses at each mirror, the changes in cavity parameters from cold to hot cavity are:

Table 11 Temperature effects in the IMC

		cold	Hot
MC1 radius of curvature	m	>10000	-4000
MC2 radius of curvature	m	26.769	26.9116
MC3 radius of curvature	m	>10000	-4000
Cavity g factor		0.3897	0.3929
MC waist	mm	2.1028	2.1098
Rayleigh range	m	13.0558	13.1429

The rejection and dewiggling properties of the input mode cleaner are not affected by heating.

Frequency Noise

Length fluctuations of the input mode cleaner will compromise the frequency stability of the light leaving the input mode cleaner. Figure 7.4 shows the expected total frequency noise performance and individual contributions to the MC frequency noise assuming the characteristics above. The frequency stability is limited by technical radiation pressure noise over the entire frequency range. This stability and the allowed frequency noise of the field going into the main interferometer set the requirements on the frequency stabilization loop gains.

7.3.9 Input Mode Cleaner Noise Budget

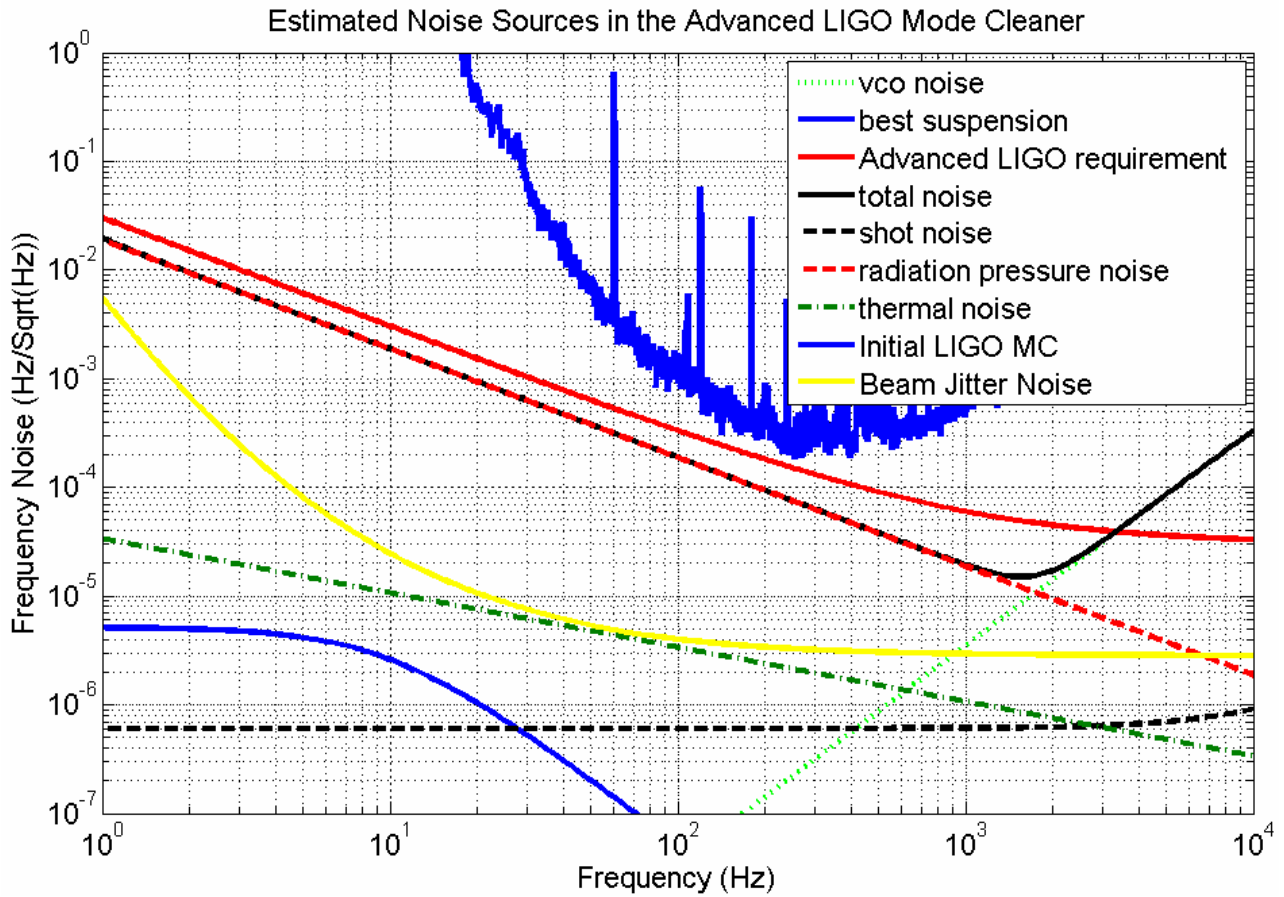


Figure 7.4 Predicted MC Frequency noise properties.

The code for this plot is described in LIGO-T030258-00-R “Single Test Cavity Design and use of the Xarm for LASTI,” David Ottaway 10/30/03, but the calculation is for the mode cleaner of Advanced LIGO.

8 Faraday Isolator

The Faraday Isolator (FI) is responsible for rejecting the back-reflected light from propagating towards the IMC and generating phase noise in the interferometer. At high optical powers, absorption in the FI optical components generates thermally-induced birefringence, thermal lensing and beam steering, requiring alternative designs and compensation methods, as well as a careful selection of the polarizers and crystals.

The Advanced LIGO Faraday Isolator design underwent a Preliminary Design Review on 28 April 2006 in anticipation of Enhanced LIGO.¹⁹ Here, we briefly update the status of the FI design since the PDR. For more details, see RODICA DOC.²⁰

8.1 Faraday Isolator Design

The Faraday Isolator consists of a birefringence-compensated Faraday Rotator (consisting of two TGG crystals and a quartz rotator), polarizers, a $\lambda/2$ waveplate, and a negative dn/dT material for thermal lens compensation.²¹

The FI for Advanced LIGO will most likely use three polarizers instead of two: a pair of calcite wedge polarizers (CWP) possessing high extinction ratios for optimal isolation and a thin film polarizer (TFP) inserted in between to minimize power-dependent beam steering in the REFL port.

8.2 Optical Characterization

Here, we separately investigated the isolation and the beam steering at optical powers as high as 103 W using a mode size of 3.9 mm, nearly identical to that expected in Advanced LIGO. Two different configurations²² were tested:

- A hybrid configuration, consisting of a fused silica thin film polarizer and a 2.5 mm thick calcite wedge, with a 4.3° wedge angle (TFP + CWP).
- A pair of identical calcite wedge polarizers (CWP + CWP) – same as in the (TFP + CWP) setup.

The performances of the FI are summarized in **Error! Reference source not found.** below.

While we have not yet characterized the full 3-polarizer setup, the two tests above provide confidence that it will work. A full test will take place at LLO in a few months.

¹⁹ LIGO-T060267-00-D, "Upgrading the Input Optics for High Power Operation", UF LIGO Group, IAP Group; LIGO-G060361-00-D, Modulators and Isolators for Advanced LIGO, UF IO Group.

²⁰ LIGO-T070021-00-D "Status of High Power Measurements in Faraday Isolators", R. Martin for IO Group, University of Florida.

²¹ E. Khaznov, N. F. Andreev, a. Mal'shakov, O. Palashov, A. K. Poteomkin, A. Sergeev, A. A. Shaykin, V. Zelenogorsky, I. A. Ivanov, R. Amin, G. Mueller, D. B. Tanner, and D. H. Reitze, "Compensation of thermally Induced Modal Distortions in Faraday Isolators" IEEE J. Quantum Electron., 40, 1500-1510 (2004).

²² The high power performances of the FI were previously tested^{Error! Bookmark not defined.} in a third configuration yet, consisting of two thin film polarizers, with very satisfactory results regarding beam drift (1.5 μ rad at 30 W optical power).

Table 12 Performance of the Advanced LIGO FI

Performance		TFP + CWP	CWP + CWP	Comments
Isolation Ratio (at 103 W input):		39 dB	49 dB	For TFP + CWP, 39 dB is limited by the extinction of the TFP.
<i>Variation in isolation across 0-103 W</i>		< 1 dB	< 5 dB	For CWP + CWP, isolation is maximum at maximum input power and decreases at lower powers.
Maximum back-transmitted Power (103 W input):		12.9 mW	1.3 mW	Better suppression for the CWP + CWP setup.
% Transmitted Power:		94 %	95 %	The FI was optimized for max. isolation (min. back reflection).
Total Optical Losses (at 103W input):		6 W	5 W	Of which ~ 3 W are lost in the second polarization of the second CWP.
Thermal Drift (at 103W input): (± 30 μrad)	<i>Transmission:</i>	< 30 μrad (0.3 μrad/W)	< 50 μrad (0.5 μrad/W)	Larger drift for CWP + CWP setup.
	<i>Reflection:</i>	< 50 μrad (0.25 μrad/W)	< 80 μrad (0.4 μrad/W)	Drift in reflection is ~twice as in transmission (FR and first CWP are double passed).

8.2.1 Optical Isolation

The optical isolation was determined as the dB ratio between the incident and the backward transmitted light. In **Error! Reference source not found.** below, the isolation ratio vs. incident optical power is displayed for each of the two configurations. In each case, the setup was optimized for maximum isolation at the highest power (103 W) and not adjusted thereafter.

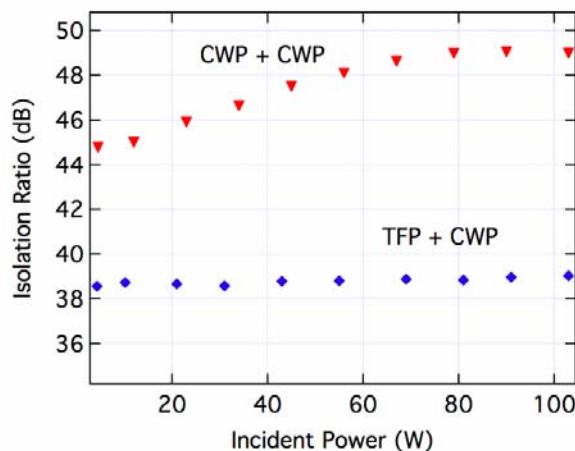


Figure 8.1 Power-dependent optical isolation for FI using one TFP and CWP (blue diamonds) and a pair of CWPs (red triangles)

The TFP + CWP configuration presents a lower isolation ratio (39 dB), limited by the extinction ratios of the TFPs (measured to be 40 dB). An isolation ratio of 49 dB is obtained at 103 W for CWP + CWP, essentially constant for power changes from 80 to 103 W. It decays to 44 dB as the power is reduced.

8.2.2 Thermal Drift

Thermal beam steering in forward transmission and back reflection were measured at 103 W incident power, with a Quadrant Photodetector (QPD) located ~2.5 m from the FR. The beam was first blocked for 45 min and then recorded the beam displacement for 30 minutes after illumination. As some optical elements warm up as they are illuminated (0° mirror that reflects light back into FI as well), it is not possible to separate the thermal drift caused by the FI from the environmental drift (temperature changes). Including the environmental contribution, a maximum value of **80 μ rad** was measured at 103 W in reflection for the double calcite wedge setup (**0.40 μ rad/W**) and **50 μ rad** was measured at 103 W in reflection for the double calcite wedge setup (**0.25 μ rad/W**).

8.2.3 Thermal Lens Compensation

This was investigated in a previous study [Error! Bookmark not defined.](#) in a double calcite polarizer setup, by placing a DKDP crystal after the second polarizer of the isolator. The total thermal lensing observed at 70 W of incident power was 40 m. This will be tested in vacuum at LLO in the next few months.

8.3 Vacuum compatibility

A modified housing design of the Faraday rotator was vacuum-baked (at 60C) and tested at Caltech in December 2006. An analysis by Dennis Coyne of the outgassing rate indicated that it was adequate for Enhanced LIGO and possibly Advanced LIGO, but showed high levels of “broad carbon peaks repeating every 14 AMU (broadly around 41, 55, 69, 83) ... with robust signal”. This unit was then rebaked at 80 C showing improved outgassing and no degradation in magnetic field strength.

For details, see http://www.ligo.caltech.edu/~rtaylor/your%20folder/Luke_Williams.htm

The modified design is currently undergoing a cavity contamination test at Caltech. Three new units for Enhanced LIGO have been ordered and will undergo vacuum baking in June or July 2007, so we will have more data then.

8.3.1 Preliminary UHV tests

The Faraday isolator in the two-calcite polarizer configuration was tested in vacuum at pressure values as low as 40 mTorr. The isolator was optimized at 1 atm and the throughput light was measured as a function of the pressure inside the chamber while the chamber was being pumped, at three different incident powers: 104 W, 50 W and 30 W. Preliminary results show strong degradation of the isolation as the pressure was lowered below 0.1 Torr. **Error! Reference source not found.** below displays the isolation ratio versus pressure for each of the three power levels. The strongest degradation was observed at the highest incident power - 104 W, in which case the

isolation drops to less than 30 dB at 40 mTorr pressure. The data are shown as a function of pressure, but the pump-down time was short compared to the thermal time constant at these low pressures. Consequently, the main effect is a loss of isolation as the rotator's temperature increases. Lower pressures correspond to longer times.

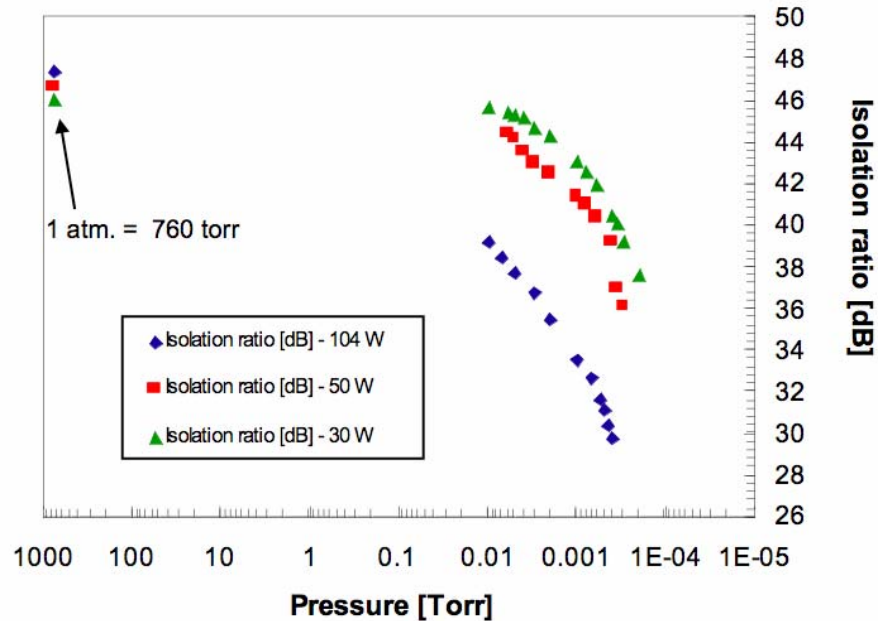


Figure 8.2 Isolation degradation with pressure, at 104 W, 50 W and 30 W.

These observations can be explained by the less efficient convection cooling of the absorbing optical elements of the Faraday isolator at higher vacuum levels.

Recently we have inserted a vacuum-compatible motorized rotation stage in the chamber to control the half-wave plate for a better optimization of the isolation. Fig. 8.3 shows that the isolation can be recovered by small adjustments of the half-wave plate in vacuum. For the data shown, the system had run for an hour and the waveplate adjusted for best isolation. Then, the isolation was measured at 10 minute intervals during the next 90 minutes, showing a decrease from 40 dB to just below 36 dB. The initial isolation was then recovered by a fractional degree adjustment of the waveplate.

The pressure increase is attributed to outgassing of the isolator as the temperature increased.

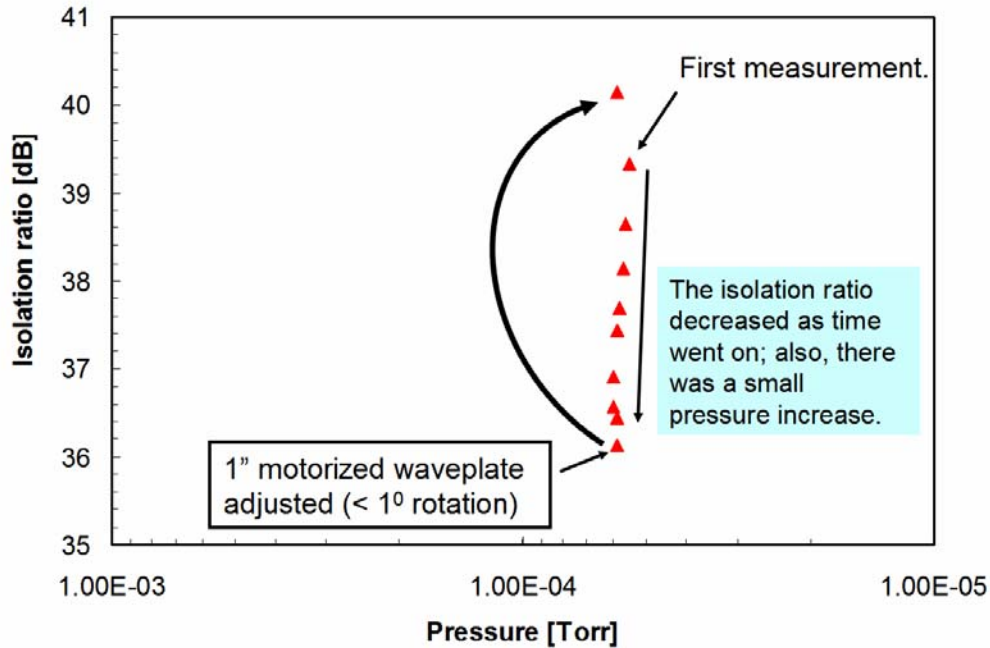


Fig. 8.3. Isolation recovery with waveplate adjustment. The measurement was made at 30 W.

Experiments continue at LLO, to investigate the time dependence of the thermally induced depolarization in the Faraday rotator and, separately, in the calcite polarizers, at constant, minimum achievable pressure. In addition we are working to develop a design that has more effective conduction cooling channels

8.4 Excess Phase Noise

As the parts of the Faraday Isolator are transmissive optics that are not suspended their motion is significantly bigger than that of the suspended optics and this could lead to extra phase/frequency noise in the light after the mode cleaner. The following sections will investigate the influence of moving focusing elements and prisms (wedged optics).

8.4.1 Movement of a focusing element

To estimate the phase changes because of transversal movement of lenses or curved mirrors we consider only perfect lenses. (This also applies to thermally generated lenses). The optimal form (no aberrations) of a focusing element with focal length f can be represented as the following change to the optical path for a given distance r from the axis:

$$\Delta l(r) = \frac{1}{4f} r^2 \quad (8.1)$$

We use this to calculate optical path change that a beam experiences when it moves from the center of the element ($r = 0$) to a position r . This formula corresponds to the following phase change for light of the wavelength λ :

$$\Delta\phi = \frac{2\pi}{4f\lambda} r^2 \quad (8.2)$$

From <http://ilog.ligo-wa.caltech.edu:7285/advligo/HAM_ISI_Expected_Performance> we can use the motion at 10 Hz ($3 \cdot 10^{-11} \frac{\text{m}}{\sqrt{\text{Hz}}}$) to estimate the introduced phase noise. For a focal length of $f = 50 \text{ m}$ this leads to a phase noise of $2.8 \cdot 10^{-17} \frac{\text{rad}}{\sqrt{\text{Hz}}}$. This corresponds to a frequency noise of $1.8 \cdot 10^{-15} \frac{\text{Hz}}{\sqrt{\text{Hz}}}$ and is well below the frequency noise requirement in LIGO-T010075-00-D at 10 Hz, which is around $10^{-5} \frac{\text{Hz}}{\sqrt{\text{Hz}}}$.

8.4.2 Movement of a prism (wedge)

The following picture illustrates the effect of a prism moving “perpendicular” to the beam.

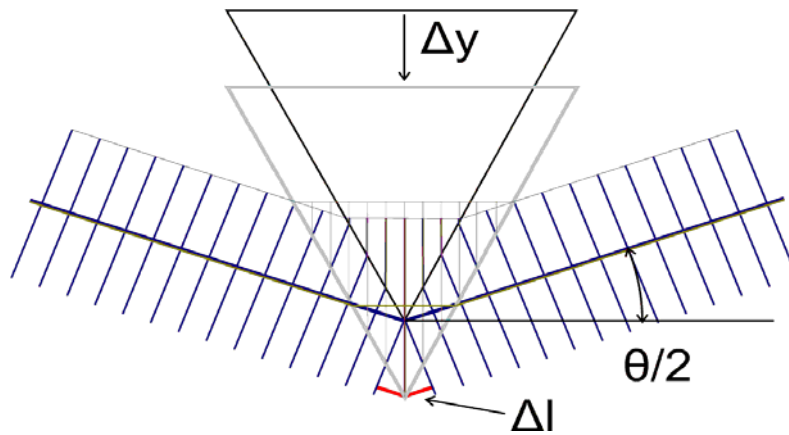


Figure 8.4 Prism moving perpendicular to the beam.

Even though the previous graph assumes plane waves it can be used to approximate the phase change of a moving (shaking) prism. In this configuration the effect is purely a phase change, but no beam shift. The path length change is:

$$\Delta l = 2 \sin\left(\frac{\theta}{2}\right) \Delta y \quad (8.3)$$

The angle θ is the bending angle relative to the incident beam. The corresponding phase change is:

$$\Delta\phi = \frac{4\pi}{\lambda} \sin\left(\frac{\theta}{2}\right) \Delta y \quad (8.4)$$

If we assume that the bending of the beam by the two calcite wedges compensates because of the common ground motion, there will still be a residual angle by which the beam is bent because the deviation at each wedge depends on its alignment. For a (assumed) remaining angle of 0.005

degrees and motion at 10 Hz of $(3 \cdot 10^{-11} \frac{\text{m}}{\sqrt{\text{Hz}}})$ this leads to a phase noise of: $3.3 \cdot 10^{-8} \frac{\text{rad}}{\sqrt{\text{Hz}}}$ or $2.1 \cdot 10^{-6} \frac{\text{Hz}}{\sqrt{\text{Hz}}}$. This is still within the specification but great care has to be used when setting up the two anti-parallel wedges.

For TFP polarizers, we are safe as long as the surfaces of the TFPs are parallel to each other within 0.005 degrees (1/3 minute). This is about a factor of 10 better than commercial flats, so some effort will be needed to produce high quality TFPs

Note that the motion of the prism along the beam introduces a parallel beam shift of

$$\Delta r = \sin\left(\frac{\theta}{2}\right) \Delta x, \quad (8.5)$$

but has **no** effect on the phase.

9 IFO MODE MATCHING TELESCOPE

The IO MMT delivers the light from the mode cleaner to the IFO with the proper mode content. The IO DRD requires that the coupling efficiency of light into the main interferometer shall be 0.95 or greater in TEM₀₀. The IO MMT matches to the average of the two interferometer arm cavities ('common mode').

The MMT is designed to:

- compensate for static variations from design values in IO as well as thermally-induced variations in the IO components.
- provide for diagnostic measurement of the mode-matching in the IFO.
- Meet constraints imposed by the physical dimensions of the HAM stacks and vacuum system.

The MMT does not:

- Correct for differential mode changes between the X and Y arms due to static errors in the COC ROC. This falls in the scope of AOS (TCS).
- Correct for thermally induced variations in the COC components. This also falls in the scope of AOS (TCS).

9.1 Overview of Mode Matching Telescope Design

The configuration of the MMT depends upon the choice of specific recycling cavity design, i.e., Stable Power Recycling Cavity (SPRC) or Marginally Stable Power Recycling Cavity (MSPRC). As of this writing, the MSPRC is the baseline, but SYS is holding for the possibility of a SPRC. For the SPRC, the MMT is integrated in the SPRC; in the MSPRC, the MMT is separate. Thus, preliminary MMT designs for both the MSPRC and the SPRC are presented.

9.1.1 Design Philosophy

The MMT design philosophy is governed by the following criteria:

- Minimizing the number of optics after the mode cleaner.
- Adjustment of the mode parameters in the IFO sufficient to meet the requirements through either (re)positioning of the MMT mirrors or adaptive heating of DKDP.
- Provide for diagnostic measurement of the mode-matching.
- Minimize astigmatism and other aberrations introduced into the main beam.
- Allow for steering of the beam into the mode IFO without significant higher order modal contamination.

9.1.1.1 Marginally Stable Power Recycling Cavity MMT

In Initial LIGO, the criteria above led us to select a three element telescope comprised of spherical reflective optics for MMT_{1,2,3}.²³ For Advanced LIGO, an analysis of i) the constraints imposed by the physical layout of the IO in vacuum, ii) the available tuning of the mode matching available using the motion of MMT₁, and iii) the capability for adaptive *in situ* tuning have led us to propose a design where MMT₁ is a flat mirror. For the Advanced LIGO FP arm cavities, the mode matching is relatively insensitive to changes in the position of MMT₁ over possible range of motions on HAM₂. Most significantly, the HAM₂ layout imposes an angle of incidence of 6.675° for MMT₁. Making MMT₁ flat will ensure that no aberrations are introduced in the system. The angles of incidence for MMT₂ and MMT₃ are much smaller (~0.5°) such that the reduction in TEM₀₀ power coupling into the arm cavity is less than 0.1%.

9.1.1.2 Stable Power Recycling Cavity MMT

In the case of SPRC, MMT_{1,2,3} are located in the SPRC and will have proper ROC matching to the recycling cavity mode. The beam from IMC will be incident at normal incidence on MMT₁ (or Power Recycling Mirror PRM). The suspensions for MMT₂ and MMT₃ now need to be similar to IMC mirrors.

9.1.2 Design Assumptions

In designing the MMT, the following assumptions are used:

- Values for COC ROC and their tolerances as given in LIGO-E060268, “Advanced LIGO Pathfinder Polish”.
- Values for the IMC mirror ROC and their tolerances are as given in Section 9.2.
- TCS will hold the COC ROC to their nominal values, ensuring that IO will mode match to the same arm cavity mode at all power levels.
- Static or fixed errors will be corrected by changing the distance between MMT₂ and MMT₃. Adaptive heating will be used to correct dynamic (power-dependent) errors in the IO.
- Aberration and wavefront modeling done for the initial LIGO MMT (see LIGO-T970143-00-D) showed that achievable surface figure errors in polishing and coating did not contribute to degradation of the wavefronts.²⁴ In addition, for small angles of incidence on the curved MMT mirrors, the introduced astigmatism did not compromise the theoretical amount of TEM₀₀ matched in the FP arms.
 - A 0.1% reduction in TEM₀₀ power coupling is allocated for astigmatism that restricts the angles of incidence to less than 0.6° on curved mirrors. Details are included in Section 9.2.5.2.

²³ LIGO-T970143-00, Design Considerations for LIGO Mode-Matching Telescopes, T. Delker, et al.

²⁴ Ibid

9.2 MSPRC MMT

9.2.1 Optical Layout of MMT

Figure 9.1 shows the conceptual layout and definition of parameters. Table 13 lists the design parameters for MSPRC. The distance values in Table 13 come from the IO optical layout. MMT radii of curvature were determined using an ABCD Gaussian propagation code and an optimization routine.²⁵

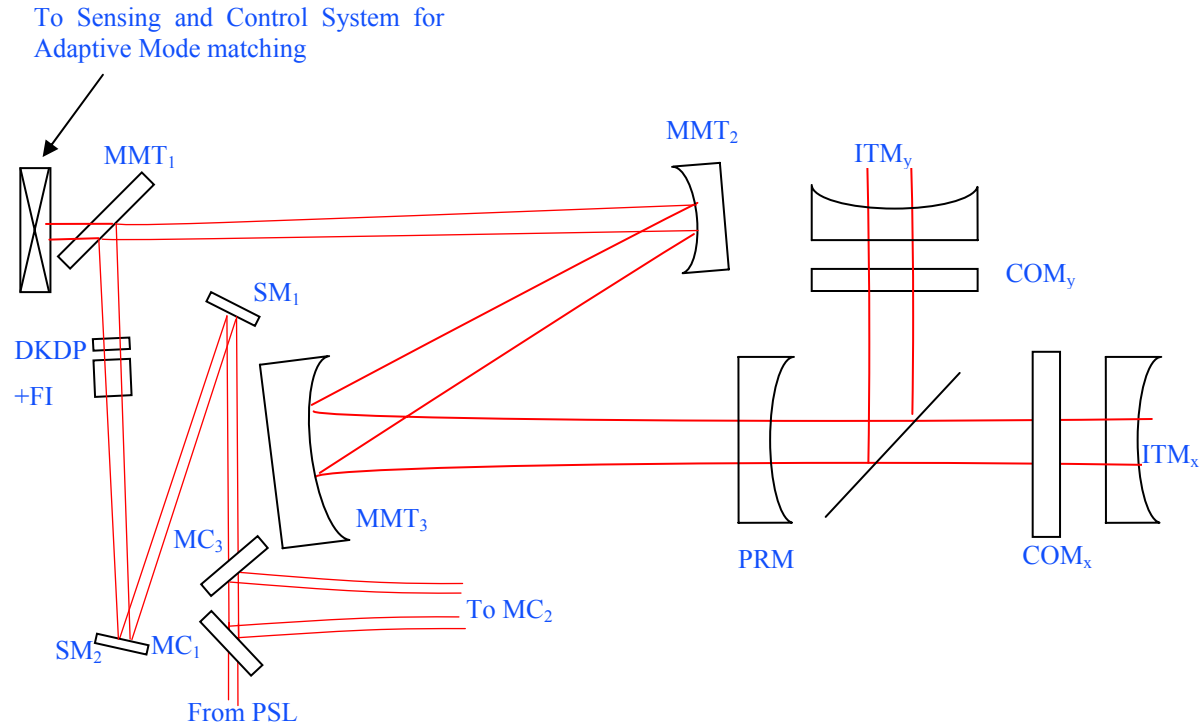


Figure 9.1 Marginally Stable Recycling Cavity Optical Layout. MMT_{1,3} are located on HAM₂; MMT₂ is located on HAM₃. Ring Heater (RH) of DKDP is used for adaptive adjustment.

9.2.2 MMT Design Parameters

Table 13 Parameters for MSPRC

<i>Definition</i>	<i>Unit</i>	<i>Value</i>
W_{mc} = Waist Size in IMC	mm	2.1028
d_{mf} = Distance b/w IMC waist and FI	m	3.1925

²⁵ POINTER TO YOUR MATLAB CODE

d'_{fs} = Distance from FI to MMT ₁	m	0.5539
MMT ₁ radius of curvature	m	>10000
d'_{12} = Distance b/w MMT ₁ and MMT ₂	m	16.8488
R_2 = MMT ₂ ROC	m	1.8135
d'_{23} = Distance b/w MMT ₂ and MMT ₃	m	15.54088
R_3 = MMT ₃ ROC	m	28.7936
d'_{pr} = Distance b/w MMT ₃ and PR	m	15.40822
R_{pr} = PR ROC	m	1436.1
d'_{pb} = Distance b/w PR and BS	m	3.50880
d'_{bs} = BS Effective thickness	mm	68.783
d'_{bt} =Distance b/w BS and ITM	m	4.5
R_{itm} = ITM ROC	m	2076
w_c = Req'd. beam waist size in arm	mm	11.53
w_{itm} = Spot Size at ITM	cm	6.0
d'_c = Beam waist location from ITM	m	2000
θ_1 = Incident angle at MMT ₁	degree	44.88
w_1 = Spot Size at MMT ₁	Mm	2.2
θ_2 = Incident angle at MMT ₂	degree	0.62
w_2 = Spot Size at MMT ₂	mm	3.9
θ_3 = Incident angle at MMT ₃	degree	0.74
w_3 = Spot Size at MMT ₃	cm	6.13
w_{pr} = Spot Size at PR	cm	6.03

9.2.3 Preliminary Mirror Component Specifications

General optical component specifications for the MSPRC are represented in Table 13

Table 14 Component Specifications

Definition	Unit	MMT1	MMT2	MMT3	Notes
Marginally Stable Power Recycling Cavity					
Substrate material		Fused Silica	BK7 ¹	BK7 ¹	¹ See 9.2.3.1
AR Surface ROC	m	>10000	>10000	>10000	
Diameter	mm	75.0, +1, -0	75.0, +1, -0	265.0, +1, -0	
Thickness	mm	25.0, +0, -0.5	50.0, +0, -0.5	100, +0, -0.5	
Wedge Angle/orientation	Arc minutes	30, +10, -0	30, +10, -0	120, +10, -0	
HR Surface Reflectivity (Intensity)		>0.9999	>0.9999	>0.9999	

Clear Aperture	mm	>60	>60	>250	
HR Surface ROC	m	>10000	1.813, $\pm 0.05^2$	28.82, $\pm 0.025^2$	² Similar to LIGO1

Note that the tolerances on ROC are similar to Initial LIGO. These tolerances are determined that any error in ROC can be compensated by repositioning MMT₂ with less than 0.5% drop in TEM₀₀ power coupling into the arm cavity.

9.2.3.1 MMT Substrate Material

To allow for unanticipated problems in TCS during commissioning and the maximum possible flexibility in IFO thermal compensation methods, we adopt BK7 as material for MMT mirrors. This is done in order to take advantage of the factor of 10 larger thermal expansion coefficient of BK7 relative to FS in the event that TCS adaptive control is needed on those mirrors.

The IO layout allows for the injection of CO₂ heating beams on MMT_{2,3} should they be needed. Similarly provision will be made for an anticipated RH at MMT₃ to help in TCS operation.

9.2.3.2 Thermal Effects in MMT Mirrors

Thermal effects in MMT mirrors can be completely neglected. The power incident on MMT_{2,3} is 125 W and at 1 ppm coating absorption, the amount of heat absorbed is 100 μ W. Therefore no correction is required for thermal effects in MMT mirrors.

9.2.4 Adaptive Mode Matching

Adaptive mode matching will be required to compensate thermal effects in FI. There is a passive thermal compensation through DKDP crystal for FI. However, there might be some residual thermal lensing left. Also, MC mirror thermal lensing may contribute to mode miss-match in the interferometer. Therefore, an adaptive system is proposed where the DKDP will be installed with a RH around its barrel for adaptive mode matching.

9.2.5 MSPRC Mode Matching Operation and Performance

- Static errors in IOO ROC will be corrected by changing the distance between MMT₂ and MMT₃. The ROC tolerances to MMT mirrors is assigned in such a way that mode matching can be improved to 99.9% for the worst case scenario in ROC errors through distance position change of MMT₂ in MSPRC.
- The proposed dynamic system of adaptive heating on DKDP is capable of handling both the thermal effects in MC as well as any residual thermal lensing in FI. Using the proposed RH, 99.5% mode matching can be restored at full power.
- Assuming simultaneous occurrence of various errors, the proposed MMT is designed to recover > 99% mode matching in the following manner:
 - Static errors due to MMT₂, MMT₃, IMC mirrors, and tolerances at their worst case values are corrected by changing the distance between MMT₂ and MMT₃.

- The passive DKDP compensation and adaptive DKDP compensation via RH on DKDP can correct the residual thermal lensing in FI such that the mode matching loss is less than 0.5%.

9.2.5.1 COC Variations

The beam waist location and beam waist size inside the arm cavity are not independent quantities. Any change in the arm cavity mirror ROC due to figure errors affects both beam waist size and location. LIGO-E060268 provides:

- Absolute ROC = 2076 – 2137 m
- Arm cavity ITM-ETM ROC mismatch tolerance = ± 3 m

Using the range of absolute ROC values, the possible beam waist location and size is shown in Figure 9.2. Using a fixed MMT design will introduce static mode-mismatch in the arm cavity with a worst case coupling efficiency drop of 3.0% assuming worst case tolerances in the ROC of the COC and the IO and appropriate re-positioning of the MMT mirrors. This mismatch is still tolerable under the IOO requirements of maintaining more than 95% coupling efficiency. However, adaptive mode-matching system consisting of CO₂ heating at MMT₂ and a RH at MMT₃ can be installed in future if needed be.

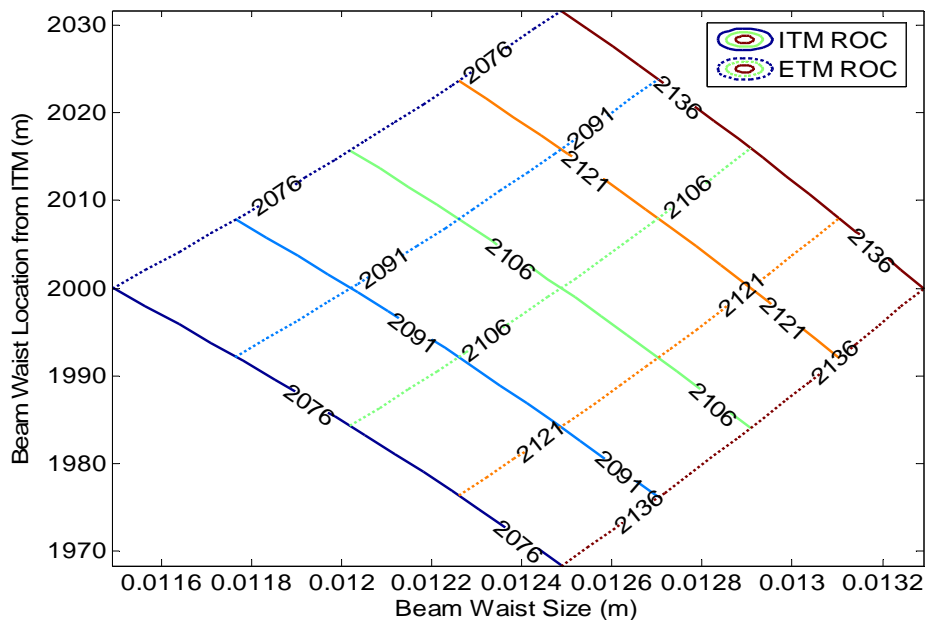


Figure 9.2 Modal Space showing the beam waist location and beam waist size inside the arm cavity as ITM and ETM ROC are varied from 2076 m to 2137 m exploring every possible combination of the two cavity mirrors. The solid lines are the contour of constant ITM ROC.

9.2.5.2 Assignment of ROC Tolerances for MMT₂, MMT₃

The ROC tolerances on MMT₂ and MMT₃ are assigned in such a way that the mode mismatch due to these tolerances can be mitigated independently by repositioning of the MMT optics to recover

99.9% mode-matching. The tolerances (similar to initial LIGO MMT specs) are presented in Table 14.

The designed value of MMT₂ ROC is 1.8130 m and the tolerance is ± 0.05 m while designed value of MMT₃ ROC is 28.7936 and the tolerance is ± 0.025 m. In terms of normalized value, this is equivalent to a ± 3.0 % (0.03 Normalized) of the designed MMT₂ ROC. Similarly for MMT₃ the respective tolerance corresponds to a ROC of 17 km ($\pm 12.0 \times 10^{-5}$ Diopter). In terms of normalized value, this is equivalent to a ± 0.15 % (0.0015 Normalized) of the designed MMT₃ ROC.

9.2.5.3 Mode Matching Adjustments for the MSPRC

9.2.5.3.1 Static Error Sources

Static errors in IOO may consist of MC curved mirror ROC tolerance resulting in MC waist mismatch from the IFO mode, incorrect positioning of the optics from MC flat mirrors to the MMT₁, incorrect positioning of MMT_{2,3}, and ROC tolerance of MMT₂ and MMT₃ assuming that TCS holds the ETM/ITM curvatures to their nominal value of 2076 m. The contribution of these errors to the mode matching drop is presented in *Table 15*.

Table 15 Static Errors Sources and Mode Miss-Match

Static Error Source	Nominal Value	Tolerance		Mode Mismatch %
		Values	%	
MC Waist	2.1028 mm	± 4 mm	± 1.0	0.01
Distance from MC-MMT ₁	3.7464 m	± 24 cm	± 6.5	0.01
MMT ₂ ROC	1.8130 m	± 0.05 m	± 3.0	36
Moving MMT ₂ ^A		± 15 mm		14
Moving MMT ₂		± 1.5 mm		0.16
MMT ₃ ROC	28.7936 m	± 0.025 m	± 0.15	12
Moving MMT ₃ ^A		± 15 mm		14
Moving MMT ₃		± 1.5 mm		0.16
Moving PR Mirror		± 15 cm		0.0002
Moving ITM		± 4.5 cm		0.0001

Note A: This is for controlling purposes. Otherwise, the expected tolerance on positioning is ± 1.0 mm.

Here, the Table 15 shows that a budget of 0.5% mode mismatch is adequate except for the ROC tolerance of MMT_{2,3}. However, as is evident from Note A above, repositioning MMT₂ and MMT₃ can alter the mode mismatch quite significantly. Therefore we can use this distance to correct errors

in ROC tolerances of MMT mirrors. Moving either $MMT_{2,3}$ changes the distance between these mirrors but since moving MMT_2 is easier because it is a smaller mirror, therefore for static error correction for ROC tolerances of MMT mirrors will be mitigated by repositioning MMT_2 .

In fact, the tolerances on MMT_2 and MMT_3 are assigned such that more than 99.5% mode matching can be recovered by repositioning of MMT_2 .

When the MMT ROCs are at their worst case values, mode matching drops to 40% with no repositioning. Mode matching into the arm cavity is far more sensitive to MMT_3 ROC. Therefore it is suggested that MMT_3 is fabricated first and ROC measured and then accordingly MMT_2 ROC is assigned.

9.2.5.3.2 Static Error Correction

To correct these static ROC errors, the position of MMT_2 is optimized. Changing position of MMT_2 by 1 cm means that the distance between MMT_1 - MMT_2 and MMT_2 - MMT_3 is changed by 1 cm. Using a search algorithm, the distance change that gives the maximum of mode matching is selected. Analysis in the MMT design document shows that mode matching can be recovered to 99.9% for all possible combinations of ROC tolerances. Figure 9.3 shows improved mode matching after reposition MMT_2 to an optimal value.

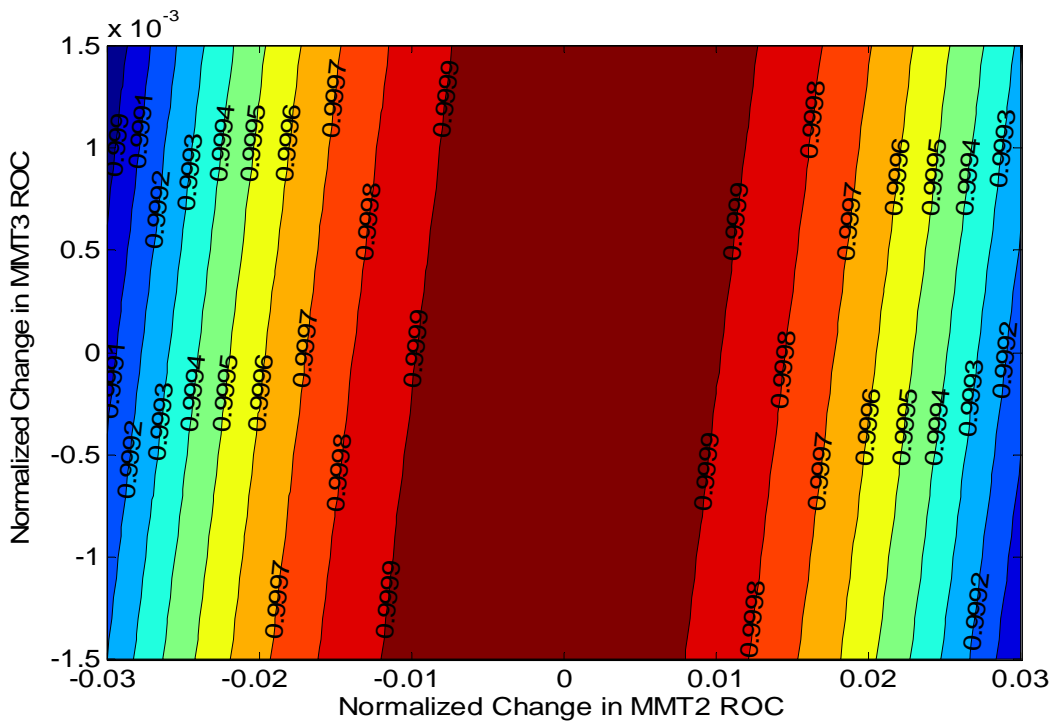


Figure 9.3 Improved mode matching as a result of repositioning MMT2 mirror to correct static errors in MMT2 and MMT3 ROC. The lines are contour of constant mode matching. The worst case mode matching is 99.6%.

9.2.5.3.3 Static Error Corrections using Adaptive Heating

Adaptive heating of MMT_2 and MMT_3 can be used to correct static errors also. However, this is not currently being planned but keeping the option of heating these mirrors, can be used further to improve mode matching if needed be.

9.2.5.3.4 Dynamic Error Correction using Adaptive Heating

Adaptive heating will be built into the IO MMT to compensate for power-dependent thermal lensing in the IO optical components (Faraday Isolator, IMC optics) via RH installed on DKDP.

9.2.6 Preliminary Adaptive Mode Matching Specifications

The DKDP serves two purposes. It passively compensates for the FI lensing. For optimal compensation, the length has to be selected very precisely and the absorptions should be known very precisely. In actual practice, there will be some residual thermal lensing left. It is proposed that the length be such selected that the residual thermal lensing is always negative. This will ensure that the positive thermal lensing in the MC flat mirror will compensate the residual FI lensing. Furthermore, the RH on DKDP will adaptively provide compensation for thermal lensing in FI. RH will provide an *in-situ* adaptive positive lensing element.

Another responsibility of DKDP adaptive compensation is to mitigate the effect of astigmatic thermal lensing in MC flat mirror. However, if we even neglect the astigmatic lens unchecked, the mode miss-match is of the order of less than 0.5%. In principle, the DKDP will be designed in such a way that we can produce an astigmatic lens in the DKDP using RH.

9.2.6.1 Optical Dynamic Range

The thermal lensing in MIO will actually help in relaxing the amount of compensation required at DKDP using RH. However, as a worst case we can assume that there is no thermal lensing in MC mirrors. Then the optimal correction is equal to the negative of residual thermal lensing in FI as shown by blue straight line in Figure 9.4 for every value of residual thermal lensing in FI. Any thermal lensing in MC will help in reducing the amount of correction needed at RH.

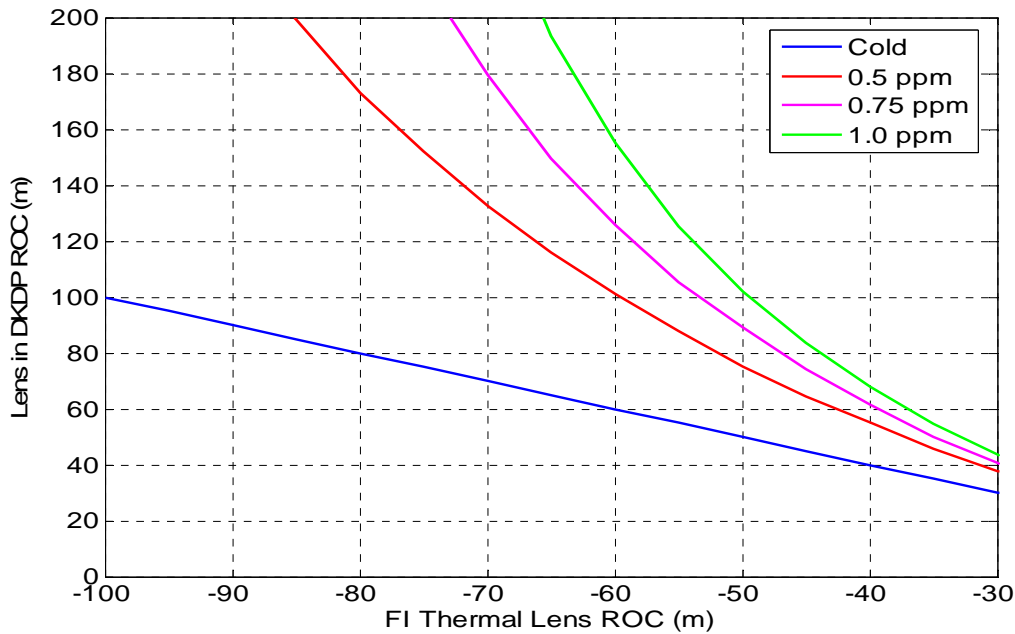


Figure 9.4 Optimal ROC required at DKDP via RH for improving the mode matching. The resultant mode mismatch becomes less than 0.25% if we apply the required correction at the DKDP for a given value of residual thermal lensing in FI.

A worst case thermal residual lensing in FI could be -60m ROC. Using this estimate, the dynamic range for the RH at DKDP should be from -60m to infinity.

9.2.6.2 Ring Heater Specifications

The RH for DKDP will consist of four segments of Nichrome Wire placed as shown in Figure 9.5. Here $RH_{1,2}$ will be used to provide compensation for the horizontal direction while $RH_{2,4}$ will be used for compensating for vertical direction. The exact details of required compensation depend upon FI performance. A servo loop will control the amount of power into the RH based upon the beam width measurements described in 1.2.6.3.

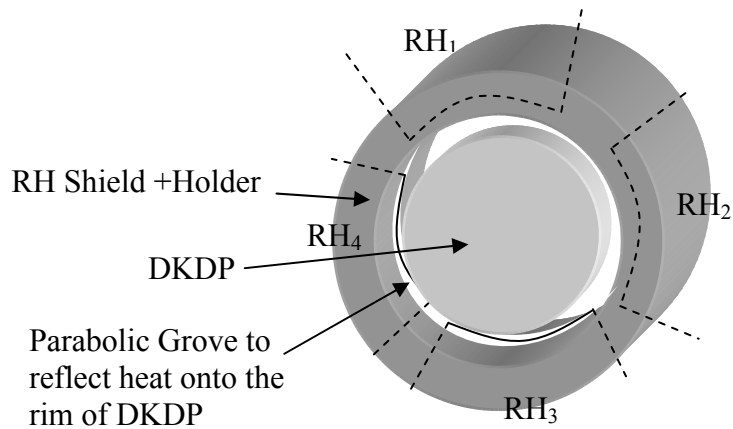


Figure 9.5 Conceptual layout of DKDP RH design. The parabolic groove will ensure that a constant flux from the heating Nichrome wire element incident on the rim of DKDP.

9.2.6.3 Sensing and Control Adaptive Heating

Sensing and control of adaptive mode matching is realized by measuring the beam width of the laser beam transmitted through MMT_1 . The optical layout is shown in Figure 9.6. Here the transmitted (or leaked) beam through MMT_1 coming from FI is used to monitor the combined residual thermal lensing in FI, DKDP, and MC mirrors. A Quad photodetector is used to monitor the position of the beam and can be used for steering the beam in the right direction. The sensing of the residual thermal lensing is realized through the beam width measurements by the CCD Camera. The effect of thermal lensing on the beam width is shown in Figure 9.7.

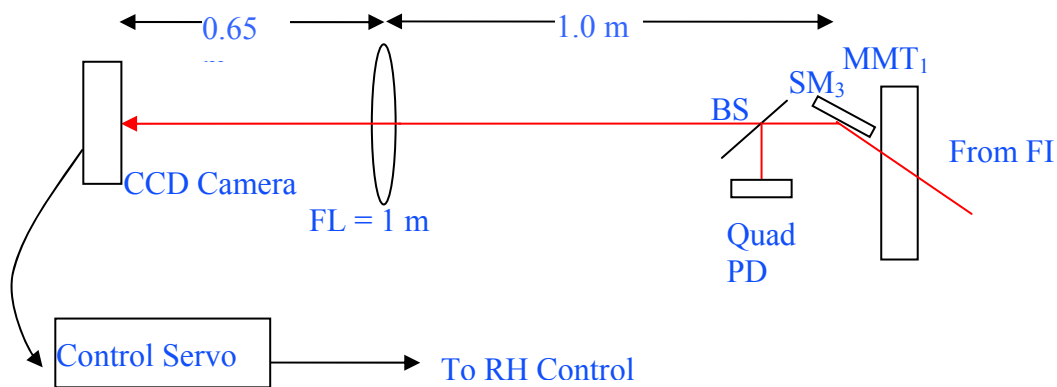


Figure 9.6 Sensing and control of adaptive mode matching in the IOO. Steering mirror SM_3 , BS, and Quad photodetector are located in vacuum while the lens and the CCD camera are

located outside the vacuum chamber. A control servo converts the beam width data to four control signals to the four DKDP RHs.

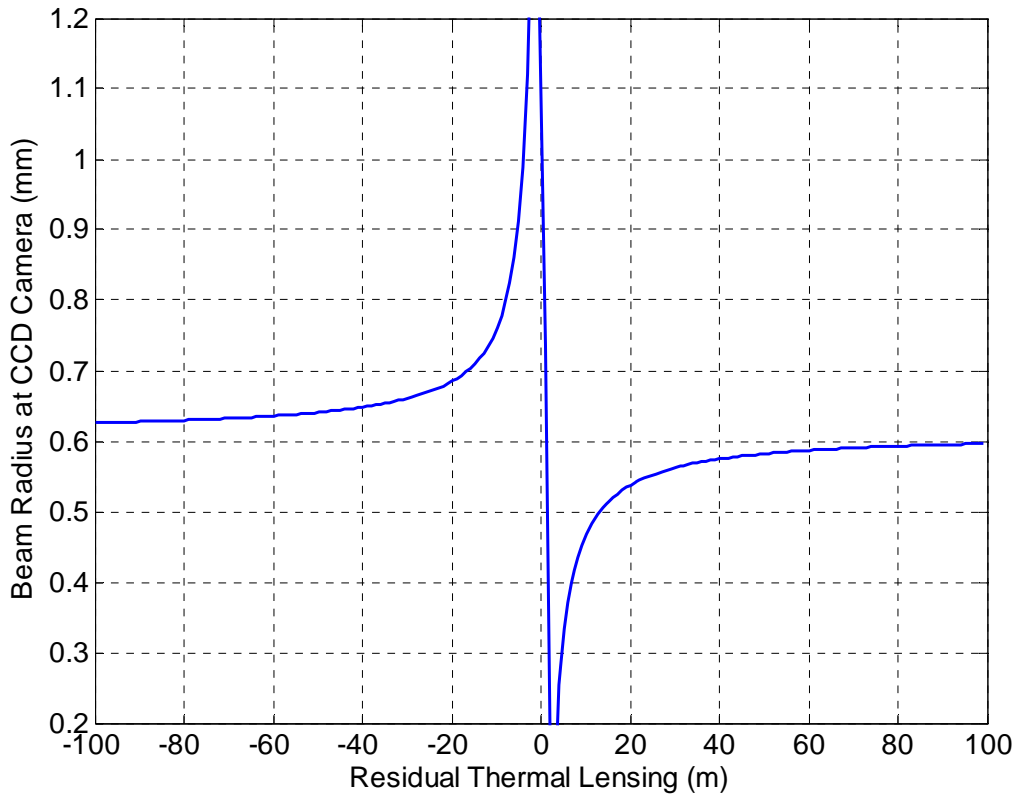


Figure 9.7 Beam radius at CCD in Figure 9.6 as a function of residual thermal lensing in FI, DKDP, and MC mirrors.

As mentioned earlier that the residual thermal lensing is expected to be negative but the system is capable of differentiating between positive and negative thermal lensing. Figure 9.7 shows that if the beam width is more than a certain threshold value (0.61 mm in this case for the specific geometry used) the residual thermal lensing is negative and the beam width increases as the residual thermal lensing gets stronger. This beam width data can then be used to control the current in DKDP RH. Here, beam width in two orthogonal directions should be measured so that any astigmatism present due to astigmatic nature of MC thermal lensing or birefringence of optical components can be corrected. The exact details of the control servo will be finalized later based upon RH design.

9.2.6.3.1 CCD Camera

Based upon available data, Spiricon L230 CCD camera is selected to be used in beam width measurements. This CCD camera comes with a software package and USB2 connection and hence

can be readily integrated into the electronic control system. Any extra frame-grabber is not required with this CCD camera.

9.3 SPRC Mode Matching Telescope

An alternate design for the recycling cavity is the Stable Power Recycling cavity. Here the MMT is incorporated in the recycling cavity and the cavity G-factor becomes 0.4. Depending upon the parametric instabilities, alignment control, and layout considerations, either of the two designs may be selected for the final design. Therefore, both designs are being considered for the IOO design document.

9.3.1 Optical Layout of Mode Matching Telescope

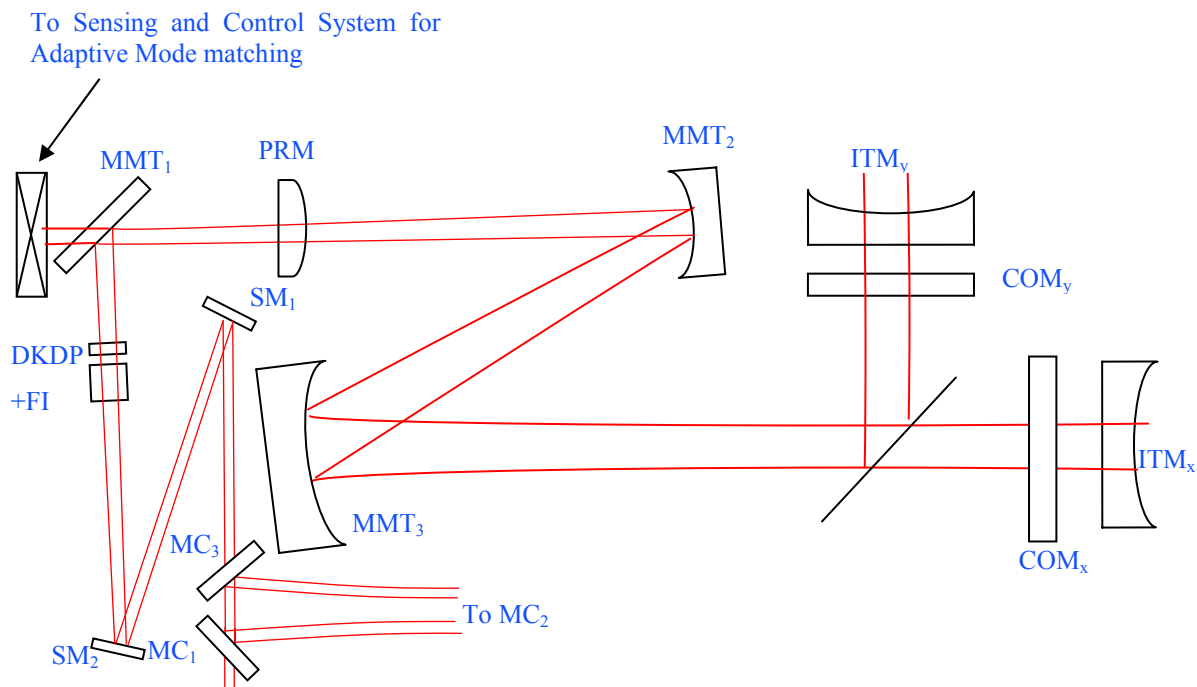


Figure 9.8 Optical layout of Stable Power Recycling Cavity. PRM and MMT3 are located on HAM2; MMT2 is located on HAM3. The main difference between SPRC and MSPRC is the position of the PRM. In SPRC, PRM replaces MMT₁.

Same procedure was used as outlined in Section 9.2.1 for determining the ROC of MMT mirrors. The distance values in Table 16 come from the IO optical layout.

9.3.2 MMT Design Parameters

Table 16 Parameters for SPRC

<i>Definition</i>	<i>Unit</i>	<i>Value</i>
w_{mc} = Waist Size in MC	mm	2.1028
d_{mf} = Distance b/w MC waist and FI	m	3.1925
d_{fp} = Distance from FI to PR	m	0.5539
PR radius of curvature	m	-70.3
d_{12} = Distance b/w PR and MMT ₂	m	16.585
R_2 = MMT ₂ ROC	m	1.8560
d_{23} = Distance b/w MMT ₂ and MMT ₃	m	16.655
R_3 = MMT ₃ ROC	m	31.059
d_{mb} = Distance b/w MMT ₃ and BS	m	20.655
d_{bs} = BS Effective thickness	mm	68.783
d_{bt} = Distance b/w BS and ITM	m	4.5
R_{itm} = ITM ROC	m	2076
w_c = Req'd. beam waist size in arm	mm	11.53
w_{itm} = Spot Size at ITM	cm	6.0
d_c = Beam waist location from ITM	m	2000
θ_1 = Incident angle at PR	degree	0.0
w_1 = Spot Size at PR	mm	2.2
θ_2 = Incident angle at MMT ₂	degree	0.745
w_2 = Spot Size at MMT ₂	mm	3.7
θ_3 = Incident angle at MMT ₃	degree	1.265
w_3 = Spot Size at MMT ₃	cm	6.11

9.3.3 Preliminary Mirror Component Specifications

Table 17 Component Specifications

Stable Power Recycling Cavity					
Substrate material		Fused Silica	BK7 ¹	BK7 ¹	¹ See 9.3.3.1
AR Surface ROC	m	>10000	>10000	>10000	
Diameter	mm	75.0, +1, -0	75.0, +1, -0	265.0, +1, -0	
Thickness	mm	25.0, +0, -0.5	25.0, +0, -0.5	100, +0, -0.5	

Wedge Angle/orientation	Arc minutes	30, +10, -0	30, +10, -0	120, +10, -0	
HR Surface Reflectivity (Intensity)		0.9985	0.9999	0.9999	MMT ₁ transmission specified by required PRC gain
Clear Aperture	mm	250	250	250	
HR Surface ROC	m	-70.3, ±2	1.856 ±0.05	31.059, ±0.25	

9.3.3.1 MMT Substrate Material

Same as Section 9.2.3.1.

9.3.3.2 Thermal Effects in MMT Mirrors

The power incident on MMT_{2,3} is 2.1 kW and at 1 ppm coating absorption, the amount of heat absorbed is 2.1mW. This results in a 2 km (3 nm sagitta change) thermal lens at MMT₂ and 6000 km (0.3 nm sagitta change) at MMT₃. Hence the thermal distortion due to coating absorption can be neglected.

9.3.4 Adaptive Mode Matching

The adaptive mode matching using DKDP is independent of the geometry of the recycling cavity and therefore it will remain same for the SPRC.

9.3.5 MSPRC Mode Matching Operation and Performance

This section is same as Section 9.2.5. The only difference is that the PRM will also has to be moved by twice the distance by which MMT₂-MMT₃ distance is changed to keep the recycling cavity length constant.

9.3.5.1 Assignment of ROC Tolerances for MMT₂, MMT₃

The ROC tolerances on MMT₂ and MMT₃ are assigned in such a way that the mode mismatch due to these tolerances can be mitigated independently by repositioning of the MMT optics to recover 99.5% mode-matching and by adaptive heating. The tolerances (similar to initial LIGO MMT specs) are presented in Table 17.

The designed value of MMT₂ ROC is 1.8560 m and the tolerance is ± 0.05 m while designed value of MMT₃ ROC is 31.059 and the tolerance is ± 0.025 m. This tolerance on MMT₂ corresponds to a lens with ROC of - 33 m (- 0.06 Diopter). In terms of normalized value, this is equivalent to a ±3.0 % (0.03 Normalized) of the designed MMT₂ ROC. Similarly for MMT₃ the respective tolerance corresponds to a ROC of 17 km (± 12.0 ×10⁻⁵ Diopter). In terms of normalized value, this is equivalent to a ±1.5% (0.0015 Normalized) of the designed MMT₃ ROC.

9.3.5.2 Mode Matching Adjustments for the SPRC

9.3.5.2.1 Static Error Sources

The details are similar to the MSPRC design. An added constraint is to move PRM by twice the distance by which MMT_2 is repositioned.

9.3.5.2.2 Static Error Corrections using Adaptive Heating

Adaptive heating of MMT_2 and MMT_3 can be used to correct static errors also. However, this is not currently being planned but keeping the option of heating these mirrors, can be used further to improve mode matching if needed be.

9.3.5.2.3 Dynamic Error Correction using Adaptive Heating

Same as Section 9.2.5.3.

9.3.6 Preliminary Adaptive Mode Matching Specifications

Same as Section 9.2.6.

9.4 Angular Noise

Document T060075-00-D by P. Fritschel verifies that the new AdvLIGO OSEMs used small optics suspensions meet the angular noise requirements. For the modematching/steering mirrors the following can be estimated.

For the new OSEMs a position sensitivity of $1 \cdot 10^{-10} \frac{\text{m}}{\sqrt{\text{Hz}}}$ at 1 Hz is targeted, see T050111-01-K “OSEM Preliminary Design Document & Test Report”. The current LIGO OSEMs reach a sensitivity of $1 \cdot 10^{-10} \frac{\text{m}}{\sqrt{\text{Hz}}}$ at 100 Hz, see figure 22 in LIGO-T960103-00-D “ASC: Environmental Input to Alignment noise”.

The requirement for the angular stability $\Delta\phi$ of the beam after the mode cleaner for a beam waist of $w(z)$ on the mirror at a given frequency is $\Delta\phi \leq \frac{\lambda}{\pi w(z)} \cdot 7 \cdot 10^{-9} \left(\frac{230 \text{ Hz}}{f} \right)^2 \frac{\text{rad}}{\sqrt{\text{Hz}}}$ assuming a misalignment of 10^{-9} rad for the ITM (from: Beam jitter coupling in advanced LIGO, G. Mueller). At 7 Hz for 2 mm beam radius this leads to $\Delta\phi \leq 1.3 \cdot 10^{-9} \frac{\text{rad}}{\sqrt{\text{Hz}}}$. This is nearly exactly the angular noise of small optics suspensions with the (new) OSEMs spaced ca. 5 cm apart and a unity gain frequency slightly lower than that.

10 Overall IO Performance

10.1 Optical throughput

The overall throughput based on the IO layout is given in Table 18. A basis of estimation is given for each subsystem or component. We assume that the PSL will meet it spec of 165 W TEM₀₀ at the PSL IO handoff.

Table 18 Optical throughput

<i>IO Subsystem or Component</i>		<i>Transmission</i>	<i>Cumulative Transmission</i>	<i>Basis of Estimation</i>
From PSL		1.0	1.0	Input beam from PSL
PSL Table Optics				
	CCD pickoff wedge	0.995	0.9950	Fused silica substrate; 300 ppm AR coatings, scatter due to dust from ambient environment
	Lens 1	0.995	0.9900	Fused silica substrate; 300 ppm AR coatings, scatter due to dust from ambient environment
	M1	0.998	0.9880	HR, scatter due to dust from ambient environment
	M2	0.998	0.9861	HR, scatter due to dust from ambient environment
	Lens 2	0.998	0.9841	Fused silica substrate; 300 ppm AR coatings, scatter due to dust from ambient environment
	1/2 wave plate	0.99	0.9743	Quartz components, commercial AR coating
	Thin film polarizer	0.98	0.9548	Measured transmission in P-pol
	MZ EOM	0.9	0.8593	Assumes 50/50 BS, ~100% visibility, m=0.6 in each arm
	M3	0.998	0.8576	HR, scatter due to dust from ambient environment
	EMMT1	0.998	0.8559	HR, scatter due to dust from ambient environment
	EMMT2	0.998	0.8541	HR, scatter due to dust from ambient environment
	EMMT3	0.998	0.8524	HR, scatter due to dust from

				ambient environment
	Pick off wedge	0.995	0.8482	Fused silica substrate; 300 ppm AR coatings, scatter due to dust from ambient environment
	1/2 wave plate	0.98	0.8312	Quartz components, commercial AR coating
	Thin film polarizer	0.99	0.8229	Measured transmission in P-pol
	Lower periscope mirror	0.995	0.8188	HR, scatter due to dust from ambient environment; vertically oriented surface
	Upper periscope mirror	0.998	0.8171	HR, scatter due to dust from ambient environment
Vacuum				0.8171
	HAM1 Vacuum Feedthrough	0.995	0.8131	Fused silica, 300 ppm AR coatings, some scatter
	HAM2 Vacuum Feedthrough	0.999	0.8130	Fused silica, 300 ppm AR coatings, clean environment
	DLC-M1	0.9999	0.8129	HR, clean environment
	DLC-M2	0.9999	0.8128	HR, clean environment
	IMC	0.9	0.7315	Historical data with some optimism thrown in...
	SM1	0.9999	0.7315	HR, clean environment
	SM2	0.9999	0.7314	HR, clean environment
	Faraday Isolator	0.95	0.6948	Measured transmission
	MMT1	0.995	0.6913	5000 ppm transmission, clean environment
	MMT2	0.9999	0.6913	HR, clean environment
	MMT3	0.9999	0.6912	HR, includes worst case beam clip losses, clean environment
Cumulative transmission			69.1%	

Based on this estimation, the IO will deliver approximately 69.1% of the light from the IO to the PRM, or roughly 114 W. This is less than the requirement, but assumes somewhat conservative values for the scatter loss on the PSL table optics.

The ‘bad actors’ are the MZ modulation, the IMC, and the Faraday isolator. Of these, there is not much we can do with the MZ and the FI, but if the IMC transmission can be improved to 96%, we can get to ~74%.

11 Diagnostics

11.1.1 PSL Table

11.1.1.1 RF Modulation

The IOO will have an optical spectrum analyzer (Tropel) on the PSL/IOO table for analyzing RF sidebands on the PSL table.

11.1.1.2 RFAM monitor

A fast photodiode (2 GHz, Thorlabs) will monitor the amplitude sidebands of the light after the Mach-Zehnder interferometer. This measurement also needs a RF spectrum analyzer capable of seeing at least three times the highest modulation frequency used.

11.1.1.3 DC photodiode monitor

A photodiode capable of measuring intensity fluctuations at the 10^{-8} RIN noise level will be present to monitor the intensity noise in the DC to 10 MHz range.

11.1.2 Mode Cleaner

11.1.2.1 RF frequency / MC length

Since we are not actively controlling the sideband frequency relative to the mode cleaner length, an RF photodiode will be used to monitor the amount of sideband power that gets rejected. RF frequency and/or MC length adjustments can be made manually when necessary.

The IOO will have the capability to monitor MC cavity ring down times using a fast photodiode on located on the ISC table.

11.1.2.2 MC mirror alignment

Cameras behind the MC mirrors can be used to monitor the MC alignment and also to guide the initial alignment or restore the alignment back to a known value.

11.1.3 Faraday Isolator

11.1.3.1 Polarization losses

The intensity of the second (unwanted) polarization at the second polarizer will be monitored to identify an increase or decrease in the polarization losses.

11.1.3.2 Depolarization and thermal lensing

The other polarization from the second polarizer can also be used to estimate the thermal lensing, including the possible effects of a ring heater around the DKDP, in the FI by measuring the beam diameter with a CCD camera. This image can also be used to gain information about the depolarization by looking at the mode picture.

11.1.4 IFO Mode-Matching Telescope

11.1.4.1 Measurement of Mode-Matched Power

Measurement of mode matched power will utilize two Bull's Eye position sensors to measure the mismatch of cavity waist size and position in the back-reflected light from the IFO.

11.1.4.2 Sensing and Control of Adaptive Heating

The adaptive mode matching needs a quadrant camera and a CCD camera (Spiricon L230) to monitor the effects of the adaptive heating, see Section 9.2.6.3 for more details.

12 Preparation for Delivery

12.1 Preparation

- Vacuum preparation procedures as outlined in LIGO Vacuum Compatibility, Cleaning Methods and Procedures (LIGO-E960022-B-D) shall be followed for all components intended for use in vacuum. After wrapping vacuum parts as specified in this document, an additional, protective outer wrapping and provisions for lifting shall be provided.
- Electronic components shall be wrapped according to standard procedures for such parts.

12.2 Packaging

12.2.1 Small Optics

Vendor provided transport packaging will be used for small optical components (diameter < 7.5cm) as in initial LIGO. At the sites we will use clean trays (D9890509-00) to hold the clean optics.

12.2.2 Mode Cleaner Mirrors and Large MMT mirror

The MC and Large MMT mirrors will be packed in specially designed containers. The COC group is developing a design to contain their large optics, although a final design has not been determined. Key elements of the design include o-ring seals to isolate the entire optic from the atmosphere, as well as Teflon or silicon o-rings used to further seal the optic surface and provide cushioning. The IO group intends to adapt the final design to the scale of the MC and Large MMT mirrors.

12.3 Marking

Appropriate identification of the product, both on packages and shipping containers; all markings necessary for delivery and for storage, if applicable; all markings required by regulations, statutes, and common carriers; and all markings necessary for safety and safe delivery shall be provided.

12.3.1 Vendor-supplied catalog items

For catalog products, vendor-provided model numbers will suffice for identification purposes. For items such as optical components (lenses, mirrors), no marks will be placed on the optics, but items will be identified their packaging.

12.3.2 Vendor-supplied custom items

For non-catalog products, vendors will be requested to provide markings. In the event that is not possible, we will identify parts by labeled packaging until installation.

12.3.3 UF manufactured mechanical and opto-mechanical components

Parts manufactured at UF will have DCC and serial numbers machined into the surface via CNC. Parts which are too small will not have numbers machined into the surface but will be identified by labeled packaging.

12.3.4 Suspended mirrors

Identification of the material shall be maintained through all manufacturing processes. Each component shall be uniquely identified. The identification shall enable the complete history of each component to be maintained (in association with Documentation “travelers”). A record for each component shall indicate all weld repairs and fabrication abnormalities. Serial numbers will be added to the suspended mirrors as noted in the individual manufacturing specifications.

13 Assembly and Installation

13.1 Installation Tooling and Fixtures

The IO alignment will use fixtures for assembly and installation of the optical components followed by an optical alignment using a low-power beam from the PSL (or another low-power laser co-aligned with the PSL beam). The following tooling and fixtures will be required.

13.1.1 PSL Table

13.1.1.1 Mach-Zehnder Modulation

- Low-power laser
- Single and Quad photodiodes
- Other standard optical lab facilities

13.1.1.2 PSL-HAM injection optics

- TBD awaiting choice of injection location.

13.1.2 In-HAM optics

13.1.2.1 Mode Cleaner Triple Suspensions

The mode cleaner triple suspensions will be provided by SUS. Vacuum preparation, cleaning, assembly, mirror insertion, and mirror balancing will follow SUS procedures, TBD.

After assembly/balancing the following will be needed: (Definition of who is responsible is TBD.)

- Clean storage
- Mechanism to transport towers from assembly area to LVEA
- Apparatus to lift towers over beam tube to access the folded interferometer
- Apparatus to lift, position, and place towers on HAM table
- IO will provide fixtures to define position on HAM table (see below)

LASTI experience could be very helpful here.

13.1.2.2 Small Optics Suspensions

These suspensions will be manufactured by the IO group, and IO will be responsible for providing hardware (silver-plated stainless screws, ordinary stainless screws, dowel pins, etc). ISC provides the OSEMS. For assembly IO will require the following items. (Definition of who is responsible is TBD.)

- Vacuum bake ovens for cleaning parts
- Small arbor press for inserting pins

- Air-bake oven for curing epoxy
- Low power laser and quad photodiode for balancing optic
- SOS EPICS controller for testing OSEMS, balance (from ISC?)
- Clean storage
- IO will manufacture the glue fixtures for attaching magnets (including fixtures for attaching magnets to standoffs)

IO will design and provide fixtures to define the SOS locations.

13.1.2.3 MMT 3 Large Optic Suspension

These suspensions will be manufactured by SUS, including assembly and hardware. ISC provides the OSEMS. After arrival at the site, IO will require:

- Vacuum bake ovens for cleaning parts
- Glue fixtures for attaching magnets (including fixtures for attaching magnets to standoffs)
- Air-bake oven for curing epoxy
- Low power laser and quad photodiode for balancing optic
- SOS EPICS controller for testing OSEMS, balance (from ISC?)
- Clean storage
- IO will provide fixtures to define position on HAM table (see below)

13.1.2.4 Faraday Isolator

IO is responsible for the Faraday isolator. The Faraday rotator parts (case, magnets, TGG and quartz crystals, polarizers, waveplate, mounts, breadboard, other small parts) will be cleaned and baked individually at a location TBD. IO will provide apparatus for assembly into a completed rotator at the site. At the site, IO will require

- Air bake oven for cleaning class B assembly apparatus
- Low power laser and quad photodiode for aligning Faraday
- SOS EPICS controller for testing OSEMS, balance (from ISC?)
- Clean storage
- IO will provide fixtures to define positions of parts on the breadboard and of the breadboard on HAM table (see below).

13.1.2.5 Auxiliary Optical Components

IO will provide any fixtures necessary to define position of auxiliary beam steering mirrors.

13.2 Installation and Alignment Procedures

Major subassemblies (Faraday isolator, Mach-Zehnder modulator, suspended optics) will be prepared in the optics lab or vacuum prep lab, aligned there, and placed into the detector as a unit. Other units (steering mirrors, mode matching optics for the IMC and for the core optics) will be placed in position individually.

13.2.1 Mechanical alignment

The fixtures will index the part to the holes on the table, which are believed to be good to $\pm 50 \mu\text{m}$ (0.002 inch), assuming good shop practices. A complete Solidworks model of the IO exists, and this will be used to determine the position of the part on its table. Chamber separation is known to $\pm 1 \text{ mm}$, based on the properties of the initial LIGO mode cleaner.

The fixtures will be in essence L-shaped brackets, touching the part at two points along one edge and at one point along a perpendicular edge. These three touches will set the translational and angular position of the part. In initial LIGO, the IO group made a universal fixture, with micrometers that could be adjusted to pre-calculated settings. This procedure worked adequately. However, it was tedious to use and risked systematic errors if the installation of the micrometers was not good. Therefore, for advanced LIGO, we will design and make fixtures for each part. These will be simple and can be manufactured in-house at Florida, so costs will not be large.

Fixtures for use in the vacuum chambers will be cleaned and bake to class B standards.

13.2.2 Optical alignment

Optical alignment will employ a low power PSL beam.

On the PSL/IO table, fixed apertures will be used to set the beam height and (with a fixture) lateral position. The components will be aligned to the beam rather than the beam aligned to the component. The alignment process will minimize the pointing and displacement of the beam relative to the fiduciary points. The polarization of the beam will be set perpendicular to the table surface (s-polarization).

In the vacuum chamber, we will use targets attached to the suspension frames for alignment of the beam. The input polarization of the light will be rotated to horizontal using a half wave plate positioned at the base of the telescope. This is done to increase the transmittance through IMC1 and IMC3.

Beam height targets will be used to set the beam horizontal, and at the correct height above the table in the HAM. The adjustments will be done either on the periscope mirrors or using mirrors on the PSL/IO table.

Table height and level will need to be monitored and adjusted during this process.

With the mirrors hanging free, the beam will be aligned through the IMC using targets, then by ensuring that the beam closes on itself, using suspension controls. (Small rotations of the towers can be used if the initial pointing is too far off.) We will not try to resonate the IMC in air.

The IMC reflected beams and transmitted beams (the latter taken through SM1) will be aligned into HAM1 and onto the detectors.

The beam will be aligned through the Faraday isolator and the mode-matching telescope in a similar fashion. With the “wrong” polarization being sent through the IMC, the Faraday half-wave plate will need to be adjusted to maximize the transmission through the Faraday for horizontally polarized light. This will have to be repositioned just before vacuum closeup.